JNC TY7400 2002-002

Moisture Migration, Growth of Biofilm and Solute Transport in Unsaturated Fractured Rock Masses

JNC Cooperative Research Scheme on the Nuclear Fuel Cycle Final Report

March 2002

Biosphere Sciences, Hiroshima University

Japan Nuclear Cycle Development Institute, Tono Geoscience Center

〒319-1194 茨城県那珂郡東海村村松 4 番地 49
核燃料サイクル開発機構
技術展開部 技術協力課

Technical Cooperation Section,
Technology Management Division,
Japan Nuclear Cycle Development Institute
4-49 Muramatsu, Naka-gun, Ibaragi 319-1194,
Japan

JNC TY7400 2002-002
2002年3月

亀裂性岩盤の不飽和領域における水の流動とそれに伴う微生物バイオフィルムの形成及び物質の移行に関する研究
（核燃料サイクル公募型研究　最終詳細報告書）

長沼　毅*　　Harihar Rajaram**
榊　利博**　　松井　裕哉***

要　旨

本研究では、亀裂～マトリックス系の湿潤・乾燥過程について、非線形拡散方程式の誘導、岩石試料の水理および誘電特性の測定、マトリックス吸水実験、単一亀裂吸水および排水実験、亀裂ネットワーク吸水実験、そして模擬亀裂表面におけるバイオフィルム形成実験を実施した。

マトリックス吸水実験では、水平および鉛直方向の含水量分布はほぼ同じで重力の影響が小さいことを確認した。単一亀裂吸水実験では、マトリックスの吸水は給水量に影響がないことがわかった。単一亀裂排水実験では、給気量の減少とともに蒸発量が低下した。亀裂ネットワーク吸水実験では、累積吸水量はある時点までは Philip の式に従うことがわかった。

吸水実験のほとんどは吸水現象がマトリックス支配型である場合は Philip の式に従った。排水過程では、亀裂性岩盤のマトリックス寸法が“半無限長の仮定”が満たさないため、蒸発量は Philip の式には完全には従わなかった。簡易モデルを用いた数値解析を実施した結果、非線形拡散方程式アプローチによって水分移動が比較的正しく推定できた。

バイオフィルム形成実験では、来待砂岩の模擬亀裂面に露出した鉱物表面に高度親水性微生物の細胞が付着して増殖し、鉱物表面上にマイクロコロニーを形成することが観察された。また、マイクロコロニーが発達して細胞同士がゆるやかに連結したネットワーク構造が観察された。さらに、岩石中の粒状物（グレイン）間を埋めるように微生物が付着・増殖することも観察された。今後の課題として、鉱物表面で生育する微生物の種類と増殖条件を網羅的に検討する必要性が示唆された。

本報告書は、核燃料サイクル公募型研究推進制度に基づき、広島大学と核燃料サイクル開発機構の共同研究により実施した研究の成果である。

*　広島大学生物生産学部
**　米国コロラド大学工学部土木工学科
***　核燃料サイクル開発機構　東濃地科学センター

JNC TY7400 2002-002
March 2002

Moisture Migration, Growth of Biofilm and Solute Transport in Unsaturated Fractured Rock Masses

Takeshi Naganuma*, Harihar Rajaram**, Toshihiro Sakaki**, and Hiroya Matsui***

Abstract

Flow and transport processes in the matrix and in individual fractures are reasonably well understood. Although the role of fracture-matrix interaction is expected to be an important factor for evaluating macroscopic behavior of fractured rock masses under two-phase flow conditions, it is not yet understood well. In this research, the moisture migration processes in fractured rock mass including the fracture-matrix interaction, and the biofilm formation on simulated fracture surfaces were investigated.

We carried out quantitative theoretical and experimental studies of wetting and drying of fracture-matrix systems. These included a consistent derivation of the non-linear diffusion equation, measurement of hydraulic and dielectric properties of the rock sample, a matrix wetting experiment, single-fracture wetting and drying experiments, and a fracture-network wetting experiment.

The diffusivity of the rock showed a distinct contribution of vapor diffusion at low water contents. In the matrix wetting experiment, the water content distribution in the vertical and horizontal directions were the same, showing that the effect of gravity was negligible. The single-fracture wetting experiment was independent of the inflow rate. The single-fracture drying experiment with a smaller air flow rate yielded a lower evaporation rate. The fracture-network wetting experiment showed that the cumulative infiltration followed the Philip's equation with a smaller sorptivity up to a certain point.

Most of the wetting experiments suggested that the Philip's equation holds when the infiltration is matrix-controlled. For drying cases, the Philip's equation did not perfectly predict the evaporation behavior because the "semi-infinite" matrix length assumption breaks down for fractured rock masses. Selected simple experiments were numerically simulated. The non-linear diffusion equation approach yielded reasonable results.

Biofilm of a highly halophilic bacterium was experimentally formed on simulated fracture surfaces using sandstone fragments. Biofilm formation was started by attachment of bacterial cells, followed by *in situ* proliferation to form microcolonies. The cells and colonies were loosely interconnected to form network-like structures on the grain surfaces, which would further develop to form film-like structures. Bacterial cell attachment and growth in the pits among grains were also observed. These observations call further needs for extensive investigation of biofilm-forming species and conditions.

This work was performed by Hiroshima University under contract with Japan Nuclear Cycle Development Institute.

* Biosphere Sciences, Hiroshima University
** Civil Engineering, University of Colorado at Boulder, USA
*** Japan Nuclear Cycle Development Institute, Tono Geoscience Center

Table of Contents

1. Introduction

For a safety assessment of an underground structure, the surrounding hydraulic environment must be well understood. Because fractures in these rocks are of primary concern as pathways for flow and transport. In this and other contexts, flow in fractured rock has been the topic of active research for the last three decades [e.g., *Evans and Nicholson,* 1987, *Faybishenko et al.,* 2000, etc.]. Fractured rock masses are extremely heterogeneous due to the contrast in porous matrix and fracture permeabilities. Depending on the fracture orientations, the fractured rock mass can be anisotropic. In the unsaturated rock masses, the redox environment may further complicate the moisture and solute transport properties due to complex microbial processes that may possibly cause fracture clogging and may change hydraulic features by biofilm formation. Flow and transport processes in the matrix (essentially a porous medium) and in individual fractures/fracture networks are reasonably well understood. Although the role of fracture-matrix interaction is expected to be an important factor for evaluating macroscopic behavior of fractured rock masses under two-phase flow conditions, it is not yet understood well in this context [*Commission on Geosciences, Environment and Resources,* 2001]. As illustrated in Figure 1-1, elementary types of fracture-matrix interaction can either be; (a) water flow through fracture a part of which is absorbed by the adjacent matrix, or (b) dry air flow through facture that removes water from matrix.

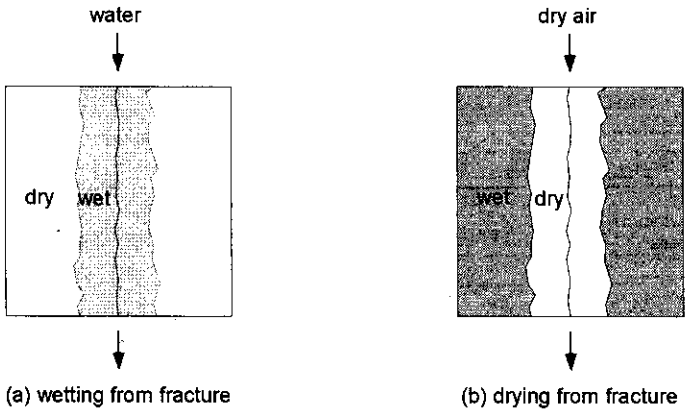

Figure 1-1. Elementary type of fracture-matrix interaction

In the case of infiltration, permeable well-connected fractures may cause very rapid flow of water over large distances. However, under large infiltration rates, large capillary gradients normal to fracture drive matrix imbibition. Imbibition may impede or even preclude intermittent fracture flow, potentially increasing travel times by several orders of magnitude [*Nitao and Buscheck*, 1991]. On the other hand, aperture variability within fractures, and gravity driven fingering [*Glass et al.*, 1996a, b] may overcome the retarding influence of matrix imbibition. The fundamental governing equation for water flow in the unsaturated rock matrix is the *Richards' equation* [*Richards*, 1931], which itself is a simplified equation where the air phase pressure is assumed to be constant. *Philip* [1967] solved the equation for an imbibition of precipitated water at the ground surface under certain boundary and initial conditions. He obtained a simple solution known as the "*Philip's equation*". It states that in the absence of gravity, the volume of infiltrated water is proportional to the square root of time, and the constant of proportionality is referred to as "sorptivity". *Tidwell et al.* [1995] showed that "local" matrix imbibition from a flowing fracture followed a linear $t^{1/2}$ relationship with a heterogeneous matrix. This may suggest that the neglect of the gravity term in the porous matrix is valid and a *non-linear diffusion equation* can be used to model matrix

imbibition during infiltration.

In partially saturated fractured rock masses, water tends to be retained in the matrix rather than in the fracture due to the larger suction in the matrix. In such a case, fractures behave like capillary barriers. In the presence of pressure or thermal gradient(s), air flow is likely to occur in such a system, and may remove water from matrix due to evaporation. This process may potentially cause a transport of toxic chemicals disposed in a geological system. *Weeks* [1987] reported that when the fractures have drained under dry conditions, substantial volumes of air can flow through the fractures due to topographic or barometric effects. Drying by this type of air flow can reduce the matrix water content and increase its imbibition capacity before the next infiltration event. In the vicinity of a ventilated waste repository drift, air flow can also occur due to ambient pressure gradients induced by ventilation. Such an air flow may be a potential source for drying the porous matrix and modifying its hydraulic properties substantially. Thus, drying of porous rock masses by advective flow of air or other gases through a connected system of fractures is a problem of considerable practical significance. However, a survey of the literature reveals very little previous research on this problem.

Drying of porous materials has been studied extensively in other contexts, such as soil physics, and a variety of industrial processes [e.g., *Gardner*, 1959]. The process of drying causes considerable losses of soil moisture, that can be 50% or more of total precipitation in arid regions. When the water table is near the surface, the suction at the soil surface is low and the soil can transmit enough moisture, thus the evaporation rate is determined by external conditions. On the other hand, as the water table becomes deeper and as the suction at the soil surface increases, the evaporation rate approaches a limiting value despite the atmospheric water capacity. *Moore* [1937] studied the

steady-state upward flow of water from a water table through the soil profile to an evaporation zone at the soil surface, and the solutions of the flow equation were given by *Philip* [1957], *Gardner* [1958], *Anat et al.*, [1965], and *Hillel* [1977]. When the water table is not near enough to the surface, it does not affect the evaporation process appreciably. For evaporation of a porous medium such as soil or rock, the gravity effect may be often neglected because the suction gradient is usually sufficiently large enough to dominate the water movement [e.g., *Hillel*, 1998]. In such a case, the non-linear diffusion equation is suitable for modeling the drying phenomenon.

At the soil surface, the evaporation occurs due to radiation and wind for most cases. The upward moisture movement is mainly due to diffusive process both in liquid and vapor. The boundary condition at the soil surface is relatively simple and can usually be explicitly specified either as a constant flux or constant water content boundary. Thus the problem can be significantly simplified. On the other hand, however, in fractured rock masses, the fractures through which air flows, exist within the porous matrix. Evaporation may occur anywhere along the fracture-matrix interfaces and the evaporation rates will vary spatially along the interfaces, depending on the local air flow rate and air humidity. Thus, the evaporation of moisture and drying of fractured rock masses induced by advective air flow in fractures, is quite different from the typical behavior of drying/evaporation in soils.

In this research, the moisture migration processes in fractured rock mass were investigated. We carried out quantitative theoretical and experimental studies of wetting and drying of fracture-matrix systems. These include a consistent derivation of the non-linear diffusion equation, measurement of hydraulic and dielectric properties of the rock sample, a matrix wetting experiment, single-fracture wetting and drying experiments, and a fracture-network wetting experiment. For some cases, the Philip's

equation was used for data analyses. Selected simple experiments were numerically simulated to validate the non-linear diffusion equation approach and to obtain insight for more detailed modeling in the future. Most of the experiments were based on the measurement of water content by a dielectric method.

In Chapter2, basic theory for infiltration and evaporation of water from rock is presented, including some definitions and a derivation of non-linear diffusion equation that accounts for water diffusion in both liquid and vapor phases. In Chapter 3, a detailed explanation of the dielectric method for local water content measurement is given. Chapter 4 presents the definitions of the material properties and the measurement results. In chapter 5, the matrix wetting experiment is presented. The single-fracture wetting and drying experiments are presented in Chapters 6 and 7, respectively. Chapter 8 gives the results of the fracture-network wetting experiment. The results for the selected numerical simulations are presented in Chapter 9. In chapter 10, the processes of biofilm formation in rock fracture are discussed. Some conclusions and recommendations for future research are given in Chapter 11.

2. Theory

The basic concepts for infiltration and evaporation of water into and from rock matrix are analogous to those for soils. In this chapter, these concepts are introduced first and the fundamental governing equation (non-linear diffusion equation) is derived.

2.1 Basics of Infiltration and Evaporation

2.1.1 Infiltration into Rock Matrix

When water is supplied at a surface of rock, it typically penetrates the surface and is absorbed into the rock matrix. A portion of water fails to penetrate and will tend to flow along the surface and eventually becomes fracture flow. *"Infiltration"* is the term applied to the process of water entry into rock [*Hillel*, 1998]. The rate of this infiltration process, relative to the rate of external water supply, determines how much water will enter the rock matrix and how much, if any, will flow through the fractures.

For a case where the external water supply rate (fracture flow rate) exceeds the water absorption capacity of the rock matrix, infiltration proceeds at a maximal rate. This maximal rate is called *"infiltrability"*. As illustrated in Figure 2-1(a), the infiltrability decreases as more water is absorbed. Once, the supply rate exceeds the rock's infiltrability, the latter determines the actual infiltration rate, and thus the process becomes "*matrix-controlled*". In this case, the excess flow in fracture remains and migrates to larger depths. On the other hand, if the rate of water supply to the rock surface is smaller than the rock's infiltrability, water penetrates as fast as it arrives and the supply rate determines the infiltration rate; that is, the process is "*supply-controlled*" *(fracture-controlled)*. For an intermittent water supply such as a precipitation event, the fracture flow will diminish to some extent because all the water will finally be absorbed by the matrix.

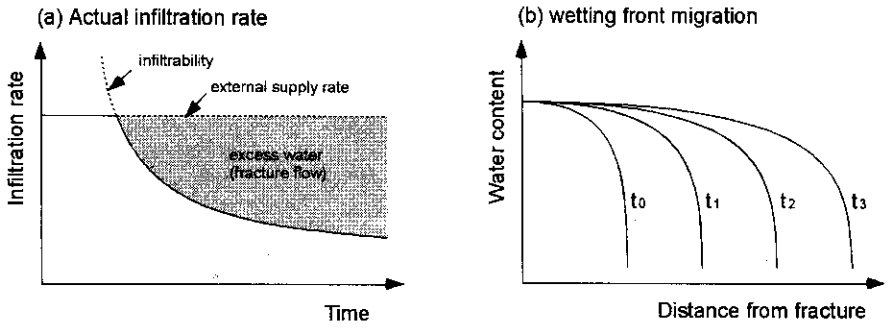

Figure 2-1. Conceptual infiltration phenomenon into rock matrix

Figure 2-1(b) illustrates the typical migration behavior of a wetting front when water is supplied at a fracture (x=0). The wetting front is normally sharp and, for soils, the water content is near saturation. The high water content at the wetting boundary makes the hydraulic conductivity of the matrix large. As a result, the wetting boundary allows water to penetrate into the matrix at a high infiltration rate. Therefore, water content is relatively high and uniform behind the wetting front, that makes the wetting front sharp.

2.1.2 Evaporation from Rock Matrix

For evaporation of water from the rock matrix to occur, three conditions are necessary. First of all, there must be a continuous supply of heat to meet the latent heat requirement (approximately 2.5×10^6J/kg or 590cal/g of water at 15 °C). Second, the vapor pressure in the air flowing through the fracture must remain lower than the vapor pressure at the surface of the matrix (i.e., there must be a vapor-pressure gradient between the matrix and fracture). These two conditions, namely, supply of energy and removal of vapor, are generally external to the evaporating body (matrix) and are influenced by meteorological factors such as air temperature, humidity, velocity, and

radiation. These together determine the maximal flux at which the atmosphere can vaporize water from a free water surface, which is referred to as the atmospheric "*evaporativity*".

The third condition is that there be a continuous supply of water from or through the interior of the matrix to the site of evaporation (fracture surface). It depends on the water content and potential in matrix as well as on its conductive properties, which determine the maximal rate at which the matrix can transmit water to the evaporation site. This maximal rate is called "*evaporability*".

Accordingly, the actual evaporation rate is determined either by the evaporativity of the air flowing through the fracture or evaporability of matrix, whichever is smaller. Figure 2-2(a) shows the typical change of evaporation rate with time, which can be divided into three stages.

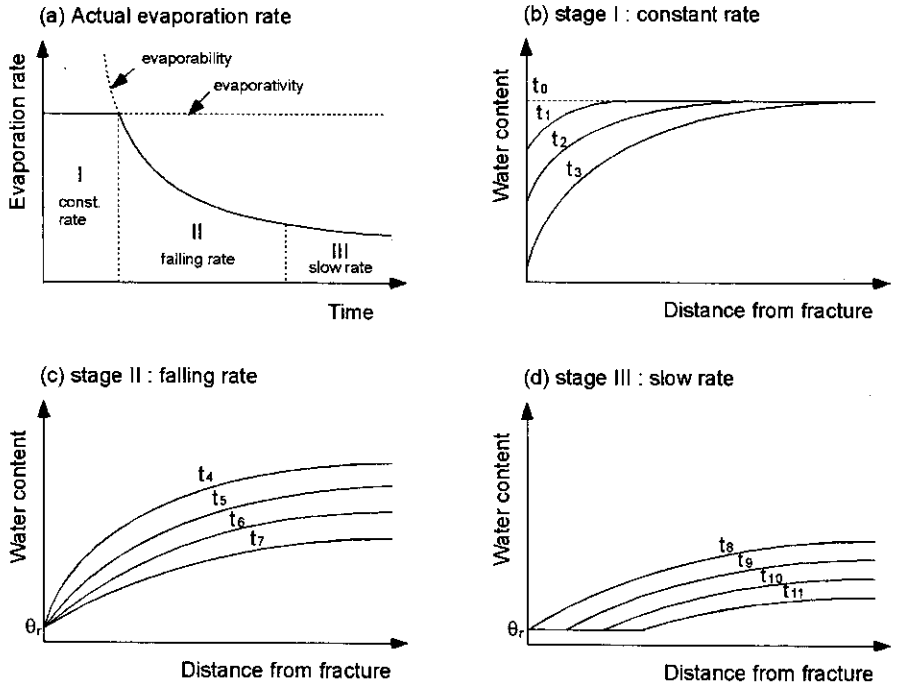

Figure 2-2. Conceptual evaporation phenomenon from semi-infinite rock matrix

(1) Stage I (*constant-rate stage*):

Initially, the matrix is wet and conductive enough to supply water to the fracture surface. This is when evaporability>evaporativity, thus the actual evaporation rate is controlled by the evaporativity. Since it is the maximal amount of water that the air can extract from the matrix, it remains constant as long as the air flow conditions remains the same. During this stage, as shown in Figure 2-2(b), water content gradients toward the fracture surface become steeper, as the surface becomes progressively drier until water content reaches its "air-dry" value (normally referred to as the residual water content; minimal water content under natural conditions). This stage may also be referred to as the "*fracture-controlled*" stage. If the rock matrix is not sufficiently wide, water content decreases more uniformly over the column length.

(2) Stage II (*falling-rate stage*):

Following the constant-rate stage is the falling-rate stage during which the evaporation rate falls progressively below the evaporativity. At this stage, the evaporation rate is limited by the rate at which the drying matrix can deliver moisture toward the fracture surface (evaporability). This stage may persist for a much longer period than stage I. Unlike stage I, water content gradients toward the fracture become less steep during stage II after the fracture surface has dried to its "air-dry" value (Figure 2-2(c)). This stage may also be referred to as the "*matrix-controlled*" stage. The transition from stage I to II is generally distinctive.

(3) Stage III (*slow-rate stage*):

The fracture surface zone eventually becomes so dry that further liquid water

conduction through matrix ceases. Water transport through the desiccated layer thereafter occurs primarily by the slow process of vapor diffusion. The lowest water content transmits into the matrix (Figure 2-2(d)). Stage II usually blends into III very gradually and these two may not be separated.

2.2 Governing Equations

In this section, the governing equation for water flow in the matrix is presented. Starting with the two-phase flow equations, simplifying them based on appropriate assumptions, the resulting equation has the form of a non-linear diffusion equation, which accounts for water transport both in liquid and vapor phases. Under proper boundary conditions e.g., infiltration/evaporation rate or water content specified at the fracture-matrix interface, the non-linear diffusion equation should predict the water migration in the matrix reasonably.

2.2.1 Two-Phase Matrix Flow and Richards' Equations

Assuming no thermal gradient, the generalized 3D *Darcy equations* for liquid water and air in matrix are;

$$v_{wx} = -\tilde{K}k_{rw}\frac{\partial h_w}{\partial x}, \qquad v_{wy} = -\tilde{K}k_{rw}\frac{\partial h_w}{\partial y}, \qquad v_{wz} = -\tilde{K}k_{rw}\frac{\partial h_w}{\partial z} + \tilde{K}k_{rw}\omega \tag{2.1}$$

$$v_{ax} = -\tilde{K}\left(\frac{\mu_w}{\mu_a}\right)k_{ra}\frac{\partial h_a}{\partial x}, \qquad v_{ay} = -\tilde{K}\left(\frac{\mu_w}{\mu_a}\right)k_{ra}\frac{\partial h_a}{\partial y}, \qquad v_{az} = -\tilde{K}\left(\frac{\mu_w}{\mu_a}\right)k_{ra}\frac{\partial h_a}{\partial z} \tag{2.2}$$

where,

v_a : air velocity in Darcy sense (same as specific discharge) [m/s]

v_w : water velocity in Darcy sense (same as specific discharge) [m/s]

$\tilde{K}$: saturated hydraulic conductivity [m/s]

k_{rw} : relative permeability of water [-]

k_{ra} : relative permeability of air [-]

ω : sine of the angle of the flow direction, ω=-1 for vertical downward flow, ω=0 for horizontal flow [-]

μ_w : water viscosity [Pa s], [N s/m^2]

μ_a : air viscosity [Pa s], [N s/m^2]

h_a : air head in terms of "water" heights [m]

h_w : water head in terms of water heights [m]

The total flux (both water and air) in each direction is simply the sum of the above equations. However, when air is unconfined the air pressure equilibrates instantly due to its small viscosity. In such a case, it is appropriate to assume $h_a = atm. = 0(gauge)$ everywhere, resulting in no air flow. Thus, $v_{ax} = v_{ay} = v_{az} = 0$. The total flux is then simply the liquid water flux;

$$v_x = -\tilde{K}k_{rw}\frac{\partial h_w}{\partial x}, \qquad v_y = -\tilde{K}k_{rw}\frac{\partial h_w}{\partial y}, \qquad v_z = -\tilde{K}k_{rw}\frac{\partial h_w}{\partial z} + \tilde{K}k_{rw}\omega \tag{2.3}$$

The 3D mass conservation equation for liquid water is;

$$\frac{\partial(\rho_w\theta)}{\partial t} = -\nabla(\rho_w v_x) \pm cond./evap. \tag{2.4}$$

Substituting eqs. (2.3) into (2.4) yields the *Richards' equation.*

$$\frac{\partial\theta}{\partial t} = -\nabla(K(\theta)\nabla h_w) + \frac{\partial K(\theta)}{\partial z} \pm cond./evap. \tag{2.5}$$

where, θ=water content, $K(\theta)$=unsaturated hydraulic conductivity $(=\tilde{K}k_{rw})$. For a fracture-matrix system, permeability of the matrix is usually low and it may be assumed that gravity gradient is negligible compared to suction gradient [e.g., *Zimmerman*, 1990] and thus flow is expected to occur primarily in the direction perpendicular to the fracture. In such a case, the second term on the RHS of eq. (2.5) diminishes.

2.2.2 Non-Linear Diffusion Equation

Eq. (2.5) without the gravity term can be rewritten in a slightly different form;

$$\frac{\partial\theta}{\partial t} = \nabla\left(D(\theta)\nabla\theta\right) \pm cond./evap. \tag{2.6}$$

where, $D(\theta)= K(\theta)\frac{\partial h_w}{\partial\theta}$ = hydraulic diffusivity of LIQUID water. The condensation/evaporation term in eq. (2.6) is obtained from the vapor transport equation, where transport is assumed to be controlled by diffusion, and advective transport is neglected (consistent with the assumption of negligible air flow).

$$\underbrace{\left.\frac{\partial\theta}{\partial t}\right|_{ev}}_{\cdot} = -\nabla\left\{\underbrace{\frac{D_v}{\rho_w}\left[(n-\theta)\frac{\partial\rho_v}{\partial\theta} - \rho_v\right]}_{\cdot\cdot}\nabla\theta\right\} \tag{2.7}$$

where, $\left.\frac{\partial\theta}{\partial t}\right|_{ev}$ = change in water content due to phase change, which should be balanced by the divergence of vapor flux, D_v= vapor diffusivity in air, n = porosity, ρ_v= vapor density.

*: rate of change of liquid water in unit volume of porous medium due to evaporation only.

**: diffusivity that accounts for water diffusion in vapor phase.

Substituting eqn. (2.7) into (2.6);

$$\frac{\partial \theta}{\partial t} = \nabla \underbrace{\left\{ \underbrace{D(\theta)}_{liquid^*} + \underbrace{\frac{D_v}{\rho_w}\left[(n-\theta)\frac{\partial \rho_v}{\partial \theta} - \rho_v \right]}_{vapor^{**}} \right\}}_{D_{\theta h}(\theta)} \nabla \theta \tag{2.8}$$

where,

*: dominant for large θ, i.e., liquid water flow dominates water migration process under wet conditions.

**: dominant for small θ, i.e., vapor transport (diffusion) dominates water migration process under dry conditions.

or,

$$\frac{\partial \theta}{\partial t} = \nabla \left(D_{\theta h}(\theta) \nabla \theta \right) \tag{2.9}$$

Equation (2.9) is a *3D non-linear diffusion equation*, and $D_{\theta h}(\theta)$ is the combined hydraulic diffusivity that accounts for water diffusion in both "liquid and vapor" phases. This equation implies that, in some cases where liquid water content is low and vapor diffusion is dominant over liquid water diffusion, the net transfer of water may be predominantly due to vapor movement, while the liquid water content actually controls the flow. Figure 2-3 shows an example $D_{\theta h}(\theta)$ curve obtained for Yolo light clay [*Hillel*, 1998]. As can be seen, the $D_{\theta h}(\theta)$ function shows an upward increase in low water content region (<0.1). This is because in this range of water content, water is no longer

transmitted in liquid phase but can still migrate in vapor phase. As the water content further decreases (<0.04), water is not mobile either in liquid or vapor phase.

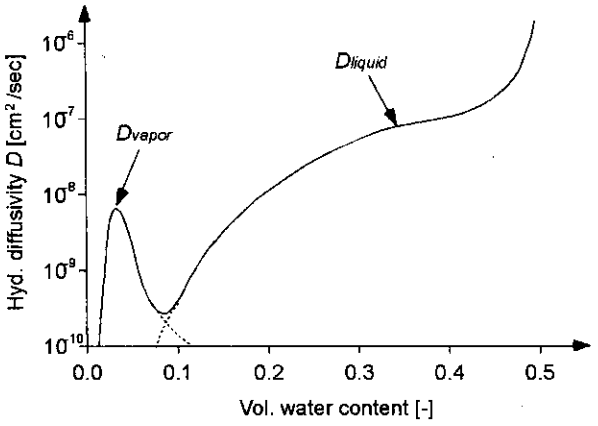

Figure 2-3. Hydraulic diffusivity function for Yolo light clay [*Hillel*, 1998]

When solving eq. (2.9), $D_{\theta_w}(\theta)$ is the most important parameter that controls the water migration through matrix. For rocks where permeability is low and suction gradient is dominant, the gravity term can almost always be neglected, this is why the non-linear diffusion equation approach is meaningful.

An important advantage of using eq. (2.9) over eq. (2.5) is that the range of variation of $D_{\theta_w}(\theta)$ is generally much smaller than that of hydraulic conductivity. For soils, the maximum value of D found in practice is of the order of 10^4 cm^2/day, and D is generally about 1-10 cm^2/day at the lower limit of wetness normally encountered in the root zone. It thus varies about a thousandfold rather than about a millionfold, as does the hydraulic conductivity in the same wetness range. Hence, small changes in θ are likely to affect the value of $D_{\theta_w}(\theta)$ to a much smaller degree than $K(\theta)$. Conversely, the use of an approximate or "average" value of D is less likely to entail large errors in calculation of flux than the use of an inaccurate value of K [*Hillel*, 1998]. A few methods for measuring

$D_m(\theta)$ for soils were established since 1950's [e.g., *Bruce and Klute*, 1956, *Whisler et al.*, 1968, etc.]. However, to the author's best knowledge, they have not been used for rocks due to the difficulty in detailed monitoring of spatially varying water content profiles in rock.

2.2.3 Philip's Equation

Philip [1967] solved the 1D *Richards' equation* for imbibition of precipitated water into a semi-infinite soil column with a boundary condition of $\theta = \theta_0$ at $z = 0$, $t>0$ and initial condition of $\theta = \theta_i$ at $t = 0$, $z>0$. He obtained a simple solution (eq. (2.10)) that includes only one parameter when gravity is neglected.

$$I(t) = S\sqrt{t} \tag{2.10}$$

where, $I(t)$ = cumulative absorbed water per unit area, the parameter S = *sorptivity*. Eq. (2.10) shows that the cumulative infiltration $I(t)$ is proportional to the square root of time. The sorptivity is a parameter that quantifies the transitional flow process induced by the instantaneous water content change at the boundary. It includes effects of the matrix suction and hydraulic conductivity, both of which depend on initial water content θ_i and boundary water content θ_0. The sorptivity S and hydraulic diffusivity $D_m(\theta)$ are inter-related (mathematical definitions are presented in eqs. (4.3) and (4.4)), however, the relationship between the two cannot be explicitly expressed. The use of eq. (2.10) greatly simplifies the formulation of fracture-matrix interaction processes under 1D wetting conditions. S is an important parameter that governs how much water is being absorbed from the fracture to matrix and how much water is passing through the current system and entering the next adjacent system.

The concept of sorptivity is extended to problems including evaporation and the parameter is re-defined as "desorptivity" [e.g., *Charbeneau*, 2000].

$$E(t) = S_E \sqrt{t} \tag{2.11}$$

where, $E(t)$=cumulative evaporation, S_E=desorptivity. Eq. (2.11) is true if the evaporation occurs under conditions on which eq.(2.10) was based.

Philip [1967] assumed that water content at ground surface at z=0 increases from θ_i to θ_o instantaneously and the soil column is semi-infinite. In case of the wetting cycle, the wetting front is usually sharp (dry rock is not water-permeable initially) and water content beyond the front remains unaffected. Thus, even for a rock block with a finite length, the semi-finite column assumption, thus eq. (2.10) is appropriate until the boundary effect becomes significant. On the other hand, for the drying cycle, water permeability is large at the beginning due to high saturation and water content will be affected in a very large region unless the rock block is semi-infinitely long. Therefore, the evaporation rate will be usually affected by the boundary from the very beginning of the drying process. For the drying cycle, eq. (2.11) may not predict the behavior perfectly.

3. Measurement Technique for Local Water Content in Rock

Most of the experiments conducted in this research were based on measuring water content in the rock matrix. A dielectric method known as time domain reflectometry (TDR), originally developed for soil water content measurement, was modified and applied to rock.

3.1 Time Domain Reflectometry (TDR)

Time Domain Reflectometry (TDR) is the most widely used method in soil water content measurement since the early 1980's. It does not require the use of a radioactive source and thus took over the place of the neutron and gamma ray methods. The method is based on measuring the transmission velocity of an electromagnetic pulse through the material of interest. The system used in this research emits a step pulse with a frequency spectrum up to 1.75GHz. For the frequency range of 100MHz-3GHz, the apparent dielectric constant K_a of soil/rock is not frequency-dependent and can be obtained by a simple relationship $v = c/\sqrt{K_a}$, where c is the speed of light (=3x10^8 cm/sec).

Rock is considered to be a 3-phase composite material consisting of rock minerals, air, and water. The apparent dielectric response of such a material depends upon the volume fraction and relative dielectric constant of each individual component. The typical dielectric constants of major rock minerals (K_{soild}) are approximately 3.8-7.5 [*Shen et al.*, 1985] and 7.5-9.2 for limestone [*Wharton et al.*, 1980]. Air and water have dielectric constants of K_{air} = 1 and K_{water} = 81 [15 °C , 300MHz, *von Hippel*, 1995], respectively. Since K_{water} is substantially larger than the others, the apparent dielectric constant of rock K_a is strongly dependent on volumetric water content θ. *Sakaki et al.* [1998a] showed that the α-mixing model describes the K_a-θ relationship well. Although

TDR is a well-known and reliable method for soil water content, applying TDR for measuring water content in rocks is still challenging, due to the difficulties in probe installation.

3.2 Application of TDR in rocks

The method requires a sensor (or probe) to be embedded in rock. The probe usually consists of two or more metal rods connected to a coaxial cable (Figure 3-1(a)). *Hokett* [1992] stated that the rods must be in good contact with the material of interest, in our case rock. However, unlike in soils, guide holes must be drilled prior to the probe installation in rock. Such guide holes rarely yield perfect contact between the probe and rock. In other words, there always remains some void space (gap) surrounding the probe. *Annan* [1977] analytically showed that if such gaps are filled with air, the apparent dielectric constant (thus water content as well) is significantly underestimated. *Knight et al.* [1992] and *Ferre et al.* [1996] numerically confirmed such effects.

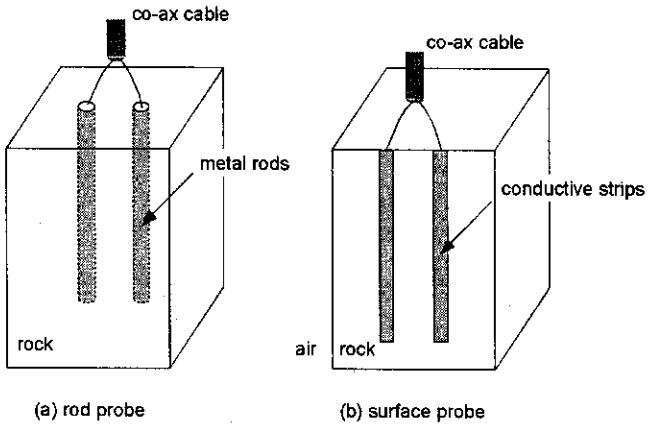

Figure 3-1. Typical TDR probe configurations

Sakaki et al. [1998a] obtained K_a-θ relationships for nine different rock samples. Their data strongly suggested the presence of gaps. *Sakaki and Rajaram* [2002a, *in*

preparation] set up gaps with controlled thickness and known material property and experimentally investigated gap effects. They used 10mm-diameter rods and varied gap thickness from 0.1-1mm. Their data showed that the gap effect can be accurately quantified if the gap width and property of the filling material is known, which is not the case in reality. *Sakaki et al.* [1998b] used porous materials such as plaster, mortar, and bentonite to fill the gaps but all these approaches led to overestimation of water content and they suggested the use of electrically conductive material instead. *Lin et al.* [1999] used an electrically conductive silicone to minimize gaps and compared with cases without such silicone. Their data showed a large improvement by reducing the gap effect.

3.3 Rod and surface probes

The TDR probes are usually inserted into the material of interest so that the probe rods are completely surrounded by the material. This is the most widely used configuration and the apparent K_a value to be obtained is the true dielectric constant of the material when installed perfectly. However, for rocks, drilling guide holes, inserting the probes, and minimizing the gaps sometimes takes a lot of effort.

An alternative approach would be to place the probes onto the rock surface (Figure 3-1(b)). *Maheshwarla et al.* [1995] and *Knight* [1997] analytically studied the characteristics of such a surface probe. They showed that the dielectric constant K'_a obtained with the surface probe is the simple arithmetic mean of the actual apparent dielectric constant of rock K_a and that of air (K_{air}=1). Therefore, K_a can be calculated from K'_a by the following simple relationship.

$$K_a = 2\,K'_a - 1 \tag{3.1}$$

Sakaki et al. [1998b] glued thin stainless strips on the smooth surface of the rock block and confirmed the validity of the above relationship. In their experiment, thickness of the glue was kept as thin as possible so that the effect of the glue on the measurement accuracy is minimized. Although the effect of the glue layer was not detectable in their experiment, it is still a potential source for errors because the glue may be absorbed by the rock and form a layer inside the rock. Using a metal tape with an adhesive layer such as aluminium foil tape would be more problematic because the adhesive layer acts as a gap.

3.4 Electrically conductive silicone surface probe

In this research, a new type of surface probe that had been developed by the authors [*Sakaki and Rajaram*, 2002b, *in preparation*] was used. An electrically conductive room-temperature-vulcanized adhesive sealant (hereafter, referred to as conductive silicone) is directly applied onto the smooth surface of a rock block to form a number of strips. It completely eliminates the presence of the adhesive layer and the associated gap effect. The dielectric constants obtained by such a silicone probe are converted into the apparent dielectric constants of rock using the eq. (3.1). The silicone to be used here is SSP-779-Silver [*Specialty Silicone Products Inc.*, volumetric resistivity = 0.01Ωcm].

3.5 Alternative-strip probe

The typical TDR probe installation for measuring water content distribution in soil is as shown in Figure 3-2(a). In a similar manner, on a rock surface, the surface probes may be installed as in Figure 3-2(b). In this research, an alternative-strip probe

configuration [*Sakaki and Rajaram*, 2002b, *in preparation*] was used (Figure 3-2(c)). With this configuration, all the strips are equally spaced and adjacent pairs of strips serve as a single probe. The advantage of this method is that the measurement interval is halved while maintaining the same number of strips.

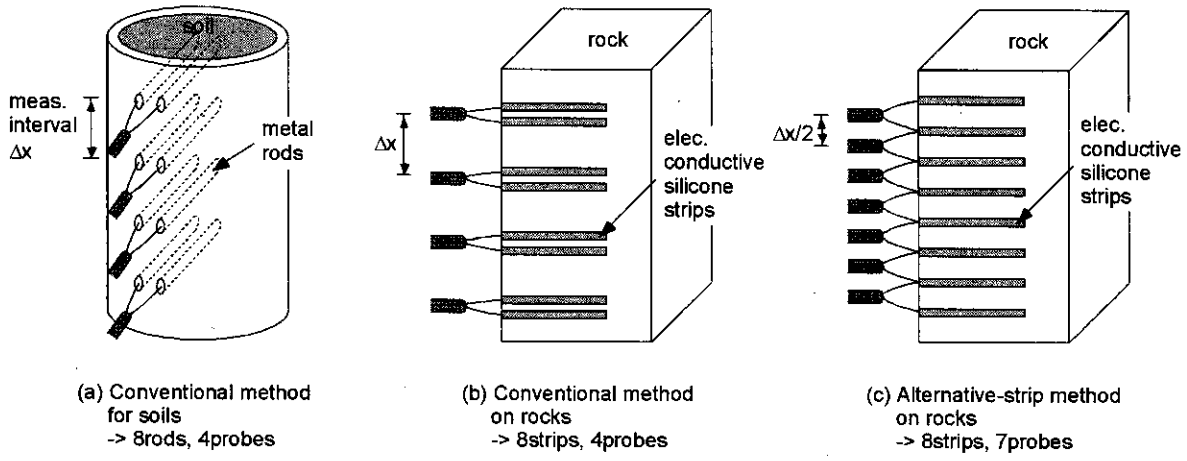

Figure 3-2. Conventional and alternative-strip probe configurations

4. Rock Properties

4.1 Porosity and Hydraulic Conductivity

The rock material used for the laboratory experiments throughout this research is "Indiana limestone (Standard Buff Limestone)", whose effective porosity is n=13-18%. Using three cylindrical specimens (diameter=5cm, length=10cm), the mean saturated hydraulic conductivity measured by the transient pulse method is K_s = 1.5x10^{-6}cm/sec and K_s = 4.6x10^{-6}cm/sec when measured using the constant head method (Table 4-1). This rock has been chosen since it is reasonably uniform and isotropic, relatively easy to drill and cut, and has an appropriate porosity and hydraulic conductivity.

Table 4-1. Hydraulic conductivity measurement

specimen#	volume (cm^3)	effective porosity (%)	transient pulse				constant head	
			confining pressure (MPa)	pore press.#1 (MPa)	pore press.#2 (MPa)	Ks (cm/sec)	head diff. (cmH2O)	Ks (cm/sec)
1	197.2	13.79	1.2	0.2	0.1	1.57e-6	1000	4.84e-6
2	197.0	13.25	1.2	0.2	0.1	1.52e-6	1000	4.71e-6
3	196.6	13.07	1.2	0.2	0.1	1.52e-6	1000	4.26e-6
mean	-	13.37	-	-	-	1.54e-6	-	4.60e-6

4.2 Dielectric Properties

4.2.1 Definition of Dielectric Properties of Rock

As mentioned in the previous section, the apparent dielectric constant K_a of partially saturated rock strongly depends on volumetric water content θ due to the large difference in individual dielectric constants of the rock mineral, air and water. Most of the experiments in the latter sections were based on measuring K_a and converting them into θ according to the dielectric property, to be more specific, the K_a-θ relationship (also referred to as the *calibration function*). The calibration function is unique to each rock material and was obtained for Indiana limestone.

4.2.2 Measurement Methods

In this research, three different types of probe were used. The description of each probe is as follows;

Type A) Rod probe in which two brass rods were inserted into guide holes and the gaps were filled with electrically conductive silicone [*Lin et al.*, 1999]. Diameter=5mm, length=80mm, spacing=20mm. It was assumed that this probe yields the true dielectric property of rock. The major disadvantage of using this probe is that this type of probe is hard to install onto rock blocks.

Type B) Surface probe made of aluminium foil tape with strip width=4mm, length=80mm, spacing=8mm. An aluminium foil tape was cut into two pieces of 4x80mm strips and attached in parallel 8mm apart onto the smooth surface of the block. This is the easiest to install but a thin adhesive layer exists between the aluminium strip and rock which acts as a gap. In such a case, the resulting K_a values depend on the probe configuration such as spacing and width of the strip.

Type C) Surface probe made of electrically conductive silicone with strip width=3mm, length=100mm, spacing=10mm. The electrically conductive silicone probe is in perfect contact with the rock surface and eliminates gap effects. Thus, the K_a values are independent of probe configuration. The silicone used here was SSP-779-Silver [*Specialty Silicone Products Inc.*, volumetric resistivity = 0.01Ωcm].

For probe types A and B, two small blocks with dimensions of 6x6x10cm and a porosity of n=17.6% were used to obtain the K_a-θ relationship (Figure 4-1(a)). The dimensions of the aluminium foil tape probe (type B) is identical to the ones used for single fracture experiments. A block with 7.8x14x2cm and n=15.3% was used for probe type C (Figure 4-1(b)). This block was cut from the same block as the one for the diffusivity measurement. The measurement procedures are as follows;

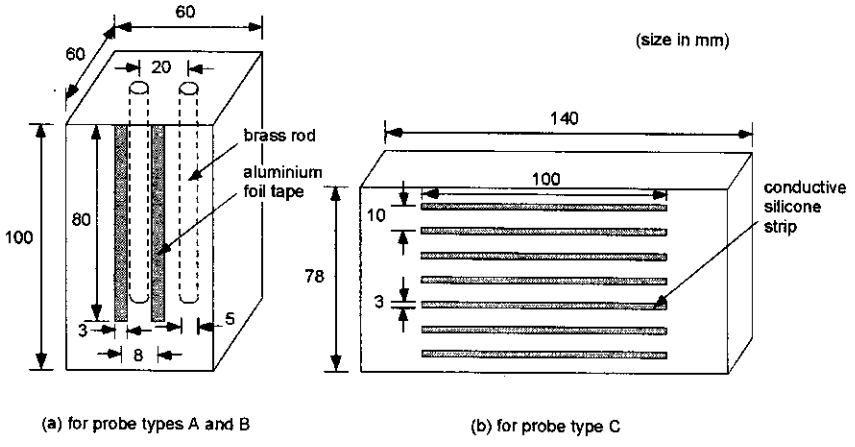

Figure 4-1. Blocks and probes for dielectric property measurement (calibration)

Measurement procedures;

Step 1: Place the blocks in water in a vacuum desiccator for more than a week. It is assumed that the blocks are saturated when no mass change is observed.

Step 2: Take the first TDR measurements, i.e., measure the apparent dielectric constant of the fully saturated blocks.

Step 3: Dry the blocks in the air until their masses attain prescribed values, determined to correspond to progressive 10% changes in saturation.

Step 4: Wrap the blocks and leave at least 24 hours to allow water inside to redistribute.

Step 5: Take another set of TDR measurements.

Step 6: Repeat steps 3~5 until the blocks are completely dry (for the last step, the block are oven-dried at 101 °C).

4.2.3 Experimental Results and Discussion

Figure 4-2 shows the calibration results for Indiana Limestone using the three types of probes mentioned above. The dielectric constants obtained with the aluminium foil tape and silicone probes were converted into the apparent dielectric constants of rock using eq. (3.1).

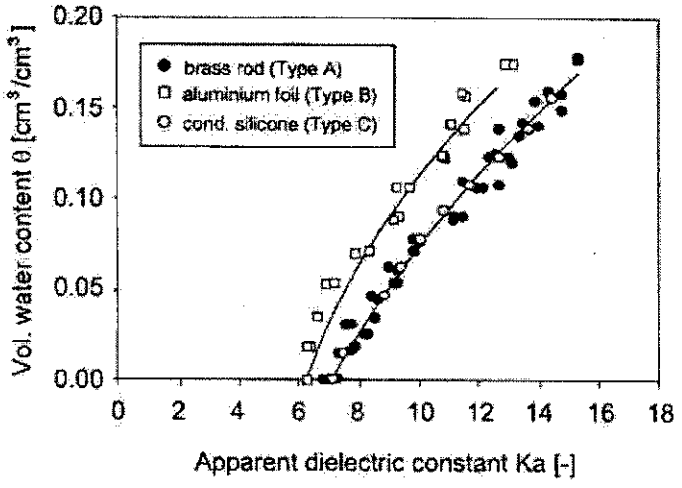

Figure 4-2. K_a-θ relationships for different probe types (Indiana limestone)

For the conventional rod probe (type A), there was a monotonically-increasing relationship between the apparent dielectric constant of rock K_a and volumetric water content θ. The aluminium foil tape probe (type B) showed lower dielectric constants. This is due to the adhesive layer that acts as a gap between the aluminium foil tape strips and rock. In this case, the adhesive layer has a lower dielectric constant than the rock material, thus the K_a values were underestimated. In addition, this gap effect depends not only on the adhesive layer thickness but also the width and spacing of the aluminium foil tape strips. Thus the calibration curve obtained using such a probe can only be used for identical probe configurations. The conductive silicone probe (type C) yielded a $K_a - \theta$ relationship identical to that obtained with the rod probe, showing that the gap effect had been successfully eliminated. Since the K_a values obtained using the rod and conductive silicone surface probes are the true values for the rock material, the calibration curves are independent of the probe configuration. The rod probe with gaps eliminated and conductive silicone surface probes give the same result; thus this establishes that the surface probes can be used in all the proposed experiments. The following are the calibration functions fitted with a second-order polynomial.

(a) For probe types A and C;

$$\theta = -0.000910K_a^2 + 0.0400K_a - 0.237 \tag{4.1}$$

(b) For probe type B;

$$\theta = -0.00103K_a^2 + 0.0438K_a - 0.220 \tag{4.2}$$

4.3 Hydraulic Diffusivity

4.3.1 Definition of Hydraulic Diffusivity $D(\theta)$

In this section, the mathematical definition of $D(\theta)$ based on *Bruce and Klute* [1956] is presented. They proposed a method for measuring $D(\theta)$ and it is probably most efficient when measured together with the sorptivity S. When the water content distribution over the whole length of the rock block at an instant t is known, $D(\theta)$ is calculated from the following equation (also see Figure 4-3).

$$D(\theta) = -\frac{1}{2}\frac{d\lambda}{d\theta}\int_{\theta_i}^{\theta}\lambda d\theta \tag{4.3}$$

where, $\lambda(\theta) = x/t^{1/2}$.

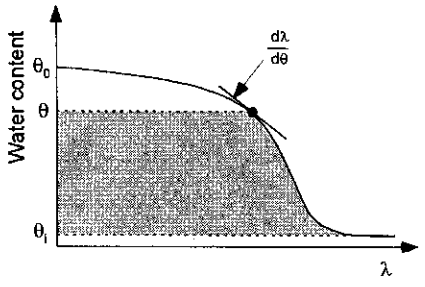

Figure 4-3. Calculation of diffusivity

4.3.2 Measuring Method

To obtain the water content distribution at pre-determined times, the apparatus shown in Figure 4-4 was used. At the wetting boundary, water was supplied at a constant head. Both the water reservoir and the block were placed on scales and their masses were monitored throughout the experiment to check the accuracy of the TDR measurement. The block has dimensions of 23.8(L) x 9.1(H) x 14.1(D)cm and a porosity

n=15.4%. The block was placed in an acrylic case to avoid unnecessary evaporation.

Jackson [1964a,b,c] measured hydraulic diffusivity using three different relatively dry soils (thus, only low water content) for both sorption and desorption cycles. His data showed that the peak due to the vapor diffusivity was observed both in sorption and desorption cycles, but the peak for the desorption cycle was less distinct, smaller in magnitude, and occurred at a higher water content than in the sorption cycle. Therefore, the hydraulic diffusivity for rocks is likely to be hysteretic and it will be measured separately for wetting and drying cycles. In this research, only the hydraulic diffusivity for the wetting cycle was obtained and discussed.

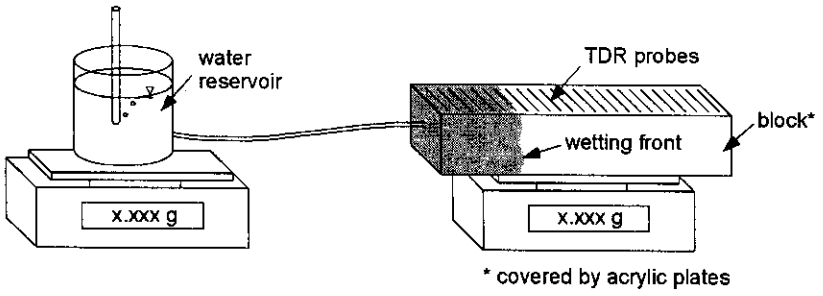

Figure 4-4. Experimental apparatus for diffusivity measurement (imbibition)

4.3.3 Experimental Results and Discussion

Photographs at selected times are presented in Photograph 4-1(A)-(B). In the photographs, the dark area on the left side of the block is the wetted region, and white lines are the conductive silicone strips. These strips were in contact with stainless steel screws that were connected to the coaxial cable. The wetting front migrated from left to right and reached the boundary (the other side of the block at x=23.8cm) at t=60hrs, after which the distribution of water content reflects the effect of the boundary.

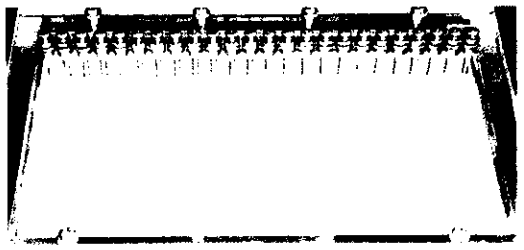

(a) t=0hours

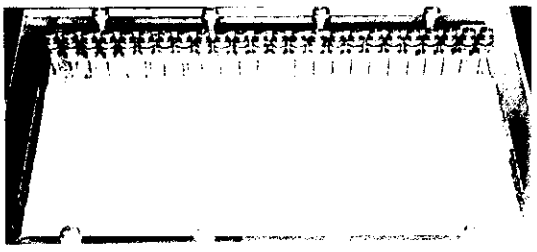

(b) t=2hours

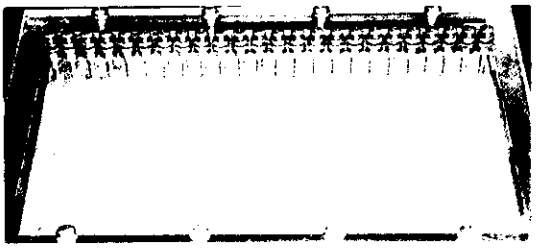

(c) t=3hours

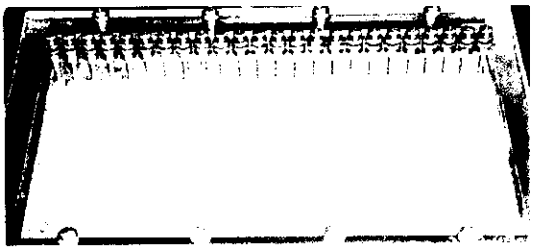

(d) t=4hours

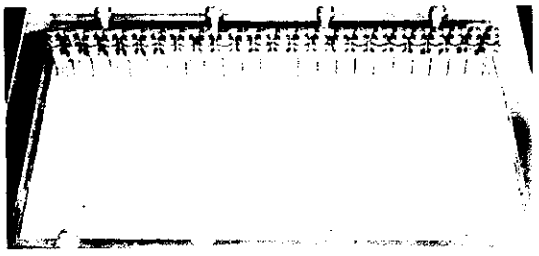

(e) t=6hours

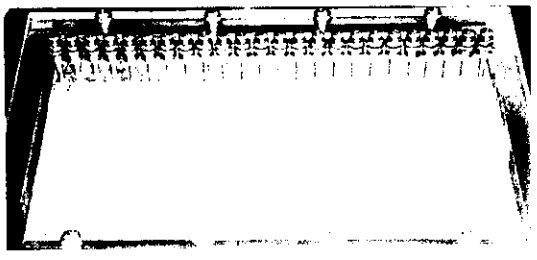

(f) t=8hours

Photo 4-1(A). Wetting front migration at selected times

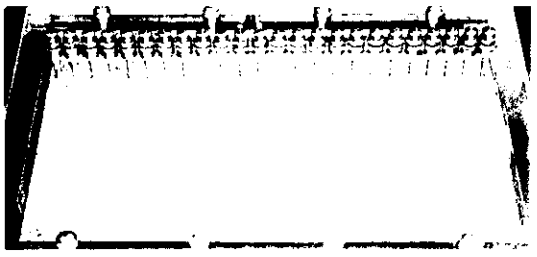

(g) t=10hours

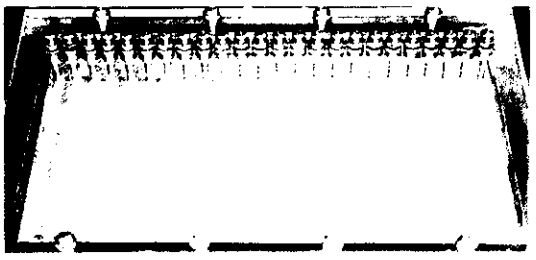

(h) t=12hours

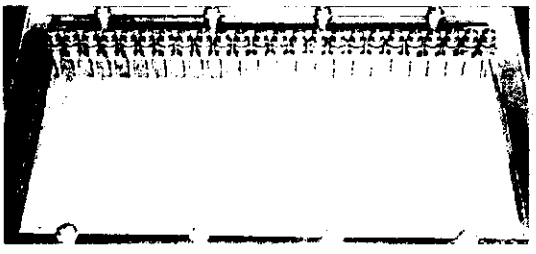

(i) t=18hours

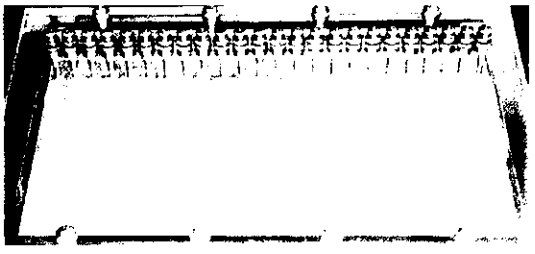

(j) t=24hours

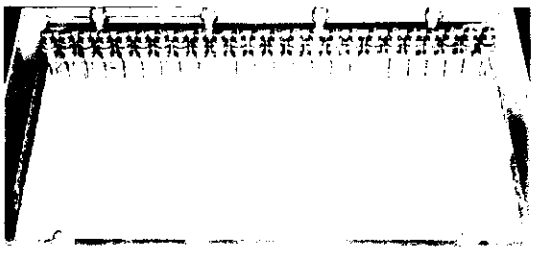

(k) t=36hours

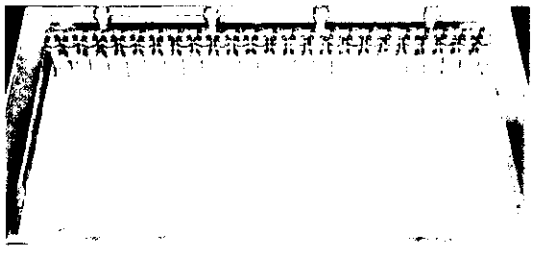

(l) t=48hours

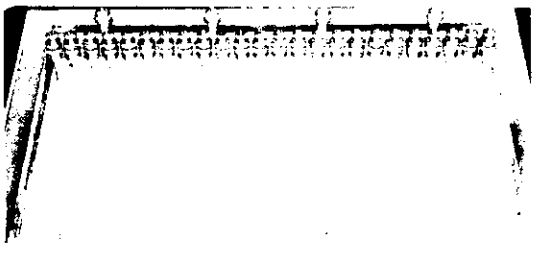

(m) t=60hours

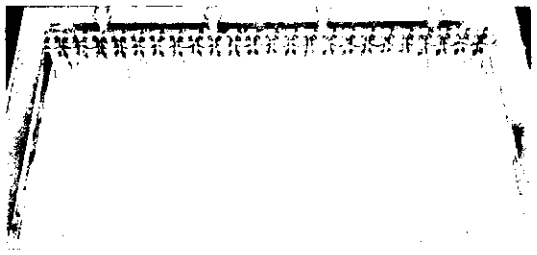

(n) t=72hours

Photo 4-1(B). Wetting front migration at selected times

The shape of the wetting front is more accurate after a certain time because there are more probes in the wet region. Thus, water content distributions at t=24, 36, and 48hours were chosen and plotted against $\lambda = x/\sqrt{t}$. As shown in Figure 4-5, the shape of the λ–θ curves for three different times was almost identical.

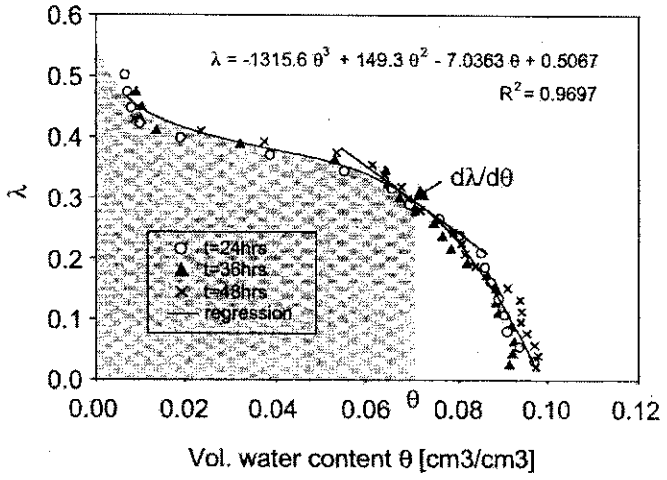

Figure 4-5. Water content distribution at selected times

The shape of the λ–θ curve was fitted with a third-order polynomial function. The function was differentiated and integrated according to eq. (4.3) and the hydraulic diffusivity $D(\theta)$ was computed. The obtained $D(\theta)$ is plotted in Figure 4-6 together with a sample exponential function. The $D(\theta)$ function ($D(\theta)$=0.0018exp(55θ)) follows the exponential function except for the low water content region. For the low water content, the $D(\theta)$ function is concave upward. This was observed for soils in the previous studies (example shown in Figure 2-3) and it was due to the water movement in vapor phase. It is difficult to measure diffusivity of liquid water and vapor separately. Therefore, the $D(\theta)$ function presented here is actually $D_{\theta v}(\theta)$, that contains both liquid water and vapor diffusivity (eq. (2.9)).

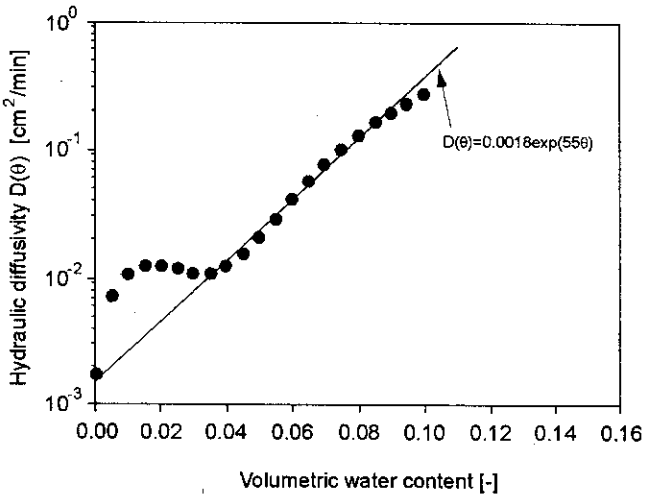

Figure 4-6. Diffusivity of Indiana limestone by the *Bruce and Klute* method

It should be noted that the $D(\theta)$ function was not obtained for θ>0.1 because the water content even near the water-supply boundary (the value at the boundary x=0 was not available because no probes were installed) did not exceed 0.092-0.10. This was about 65% of saturation and did not increase during the 24-48hour period. This is probably because entrapped air remains inside the matrix. Figure 4-7 shows the result of an alternative static imbibition experiment. The block used was the same one that had been used for the calibration with probe type C. The bottom end of the block was immersed in water to allow vertical upward imbibition. The block was enclosed in a container to avoid evaporation and its mass was measured for more than two moths. The average water content of the block at t=2days (when the wetting front reached the top boundary) was 0.092, which is only 60% of the full saturation. For t>2days, the average water content of the block increased gradually. After two months, the water content was still only 0.12, which is still only 80% of the full saturation. This slow change is probably due to entrapped air bubbles slowly dissolving into water. Supplying enough water at the boundary does not necessarily result in saturation at the boundary.

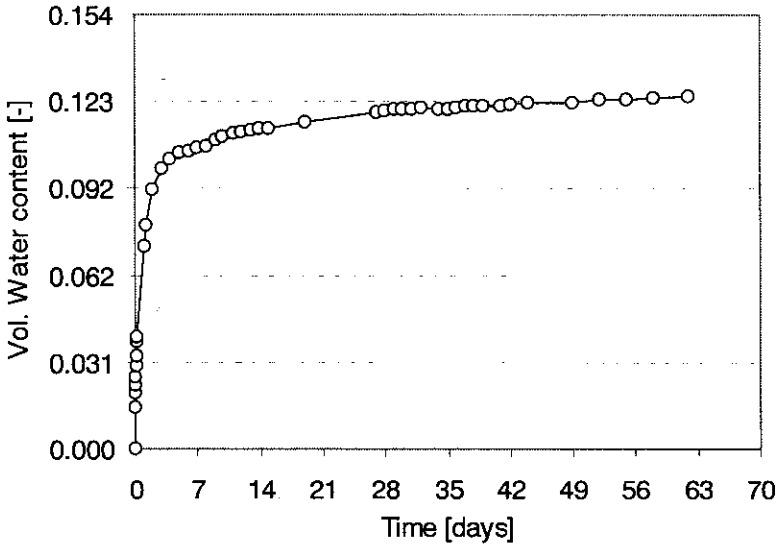

Figure 4-7. Water content change in Indiana limestone block (static imbibition test)

4.4 Sorptivity

4.4.1 Definition of Sorptivity S

Sorptivity is a parameter that quantifies the transitional flow process induced by the instantaneous water content change at the boundary. It includes effects of the matrix suction and hydraulic conductivity, both of which depend on initial water content θ_i and boundary water content θ_0. The mathematical definition of sorptivity S is given in eq. (4.4).

$$S = \int_{\theta_i}^{\theta_0} \lambda d\theta = I(t)/t^{1/2} \tag{4.4}$$

where, $\lambda(\theta) = x/t^{1/2}$ [*Philip*, 1967].

Figure 4-8 visualizes the definition in two ways. To measure sorptivity, water was continuously supplied at one end of the block. The water content distribution in the block was measured at pre-determined times. When the distribution is plotted against λ, its typical shape is as shown in Figure 4-8 (center). The cumulative absorbed water per unit area should show a straight line when plotted against $t^{1/2}$ as shown in Figure 4-8 (right).

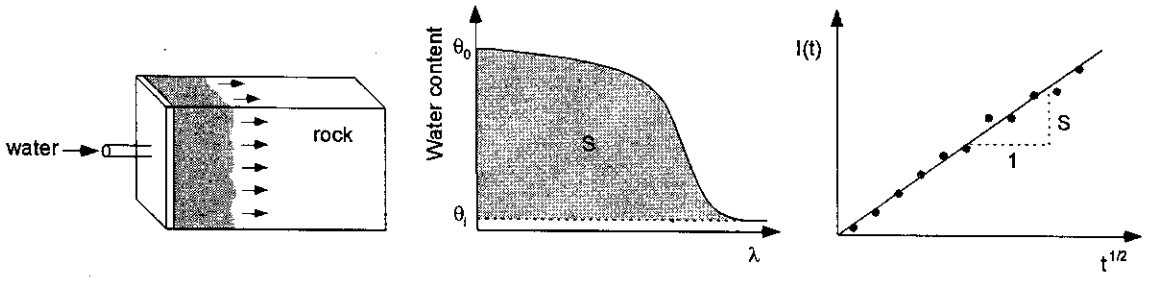

Figure 4-8. Measurement and calculation of sorptivity

The sorptivity of the block can be calculated either by integrating λ from θ_i to θ_0 or by calculating the slope of the cumulative infiltration per unit area $I(t)$ vs. $t^{1/2}$. Note

that S depends on both θ_i and θ_0. When the block is initially dry and the imposed boundary condition (θ_0) is full saturation, S takes on its maximum value. The value of S would also be affected by the heterogeneity of the matrix, dimensionality of the imbibition front, imbibition from a network of fractures, etc..

4.4.2 Measurement Technique

To measure the sorptivity, an apparatus identical to that used for the diffusivity measurement was employed (Figure 4-4). A constant-head water boundary was set at the left end of the block and the water content distribution was measured at pre-determined times.

1) *Integration method*:

Water content distribution at different times are plotted against λ. If possible, the λ–θ curves are fitted by a polynomial. Then the function is integrated and the area S is obtained.

2) *Slope method*:

The water content distribution measured by TDR is integrated over the block length and $I(t)$ is calculated. In addition, the masses of the water reservoir and block are measured and the cumulative infiltration $I(t)$ is computed from the mass change divided by the block cross section. $I(t)$ is plotted against square root of time and its slope S is computed.

This is the "representative" sorptivity value of the block under 1D imbibition and the effect of heterogeneity at scales smaller than the measurement scale (sampling volume of the probe) would not be detected.

4.4.3 Experimental Results and Discussion

(a) *Integration method*

Using the water content distributions at t=24, 36, and 48hours plotted against λ, a third-order polynomial was fitted to the data. The regression function was integrated according to eq. (4.4), and the sorptivity (shaded area in Figure 4-9) was found to be S=0.0324 cm/min$^{1/2}$.

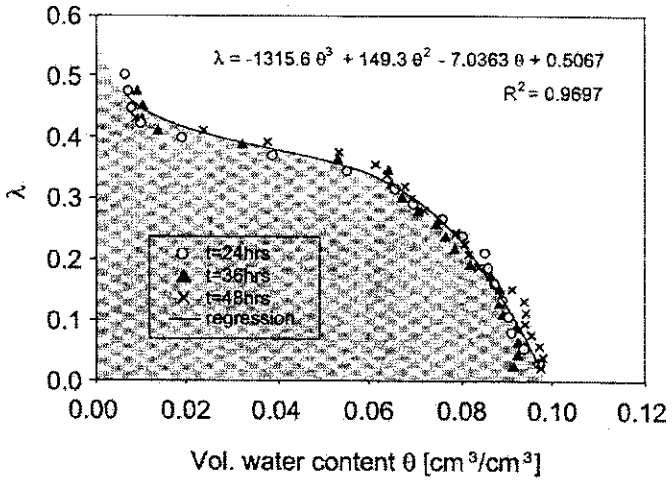

Figure 4-9. λ vs. θ at selected times

2) *Slope method*

Two balances did not respond well at the beginning and the data is erroneous at early times. Therefore, these data are not discussed. The TDR overestimated $I(t)$ up to t=3hours probably due to a slight disagreement between the fitted calibration function and measured calibration data (Figure 4-10). The cumulative absorbed water per unit area $I(t)$ was plotted against $t^{1/2}$. From the slope of $I(t)$ - $t^{1/2}$ curve, S=0.0329 cm/min$^{1/2}$ was obtained, which agrees closely with the integration method.

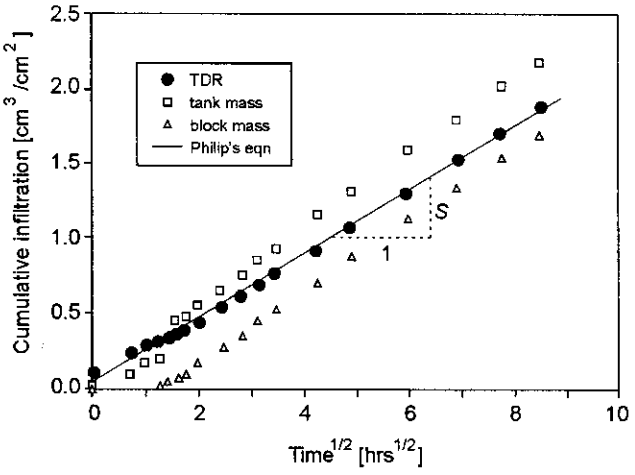

Figure 4-10. $I(t)$ vs. $t^{1/2}$

The slope estimated from TDR measurements was smaller than the estimates from mass measurements. The wetting front migration was slightly faster near the edge region where no probes were installed, showing a possibility that more water was being absorbed than measured by the TDR. This is probably the main reason for the discrepancy in slopes.

5. Matrix Wetting Experiment

The non-linear diffusion equation for matrix flow neglects the gravity effect. To verify the appropriateness of this approximation, a matrix wetting experiment was conducted and water imbibition in the horizontal and vertical directions were monitored.

5.1 Experimental Apparatus and Measurement Method

An Indiana limestone block with dimensions of 37.7(W) x 28.4(H) x 5.8(D)cm and no fractures, was subjected to water imbibition. The block was fan-dried for more than two weeks in the laboratory where the relative humidity is approximately 10-15% and temperature is $24 \pm 1°C$. As shown in Figure 5-1, a point source infiltration was applied at the middle of the top surface. Water was supplied by a pump and the head at the boundary was kept constant (approx. 0.5cm above the surface). Excess water was returned to a reservoir. This set-up should allow water to be absorbed purely by matrix suction and gravity.

As seen in the figure, nine TDR probes were installed on the vertical surface of the block. Five horizontal probes in the middle of the block were used to measure the water content distribution in the vertical direction. The two probes on the left and right measured the water content distribution in a near-horizontal direction. All the probes were aligned to be tangential to concentric circles. Due to the block size constraint, only two were installed in the horizontal direction. It was assumed that water content measured by each probe is the representative value at the midpoint of the probe. If the effect of gravity is negligible, the water content distribution as a function of r (= radial distance from the source) in the horizontal and vertical directions should be the same and the wetting front should be semi-circular. By monitoring the mass of water in the reservoir, the amount of water absorbed by the block was also measured. The

measurements were taken for 14 days.

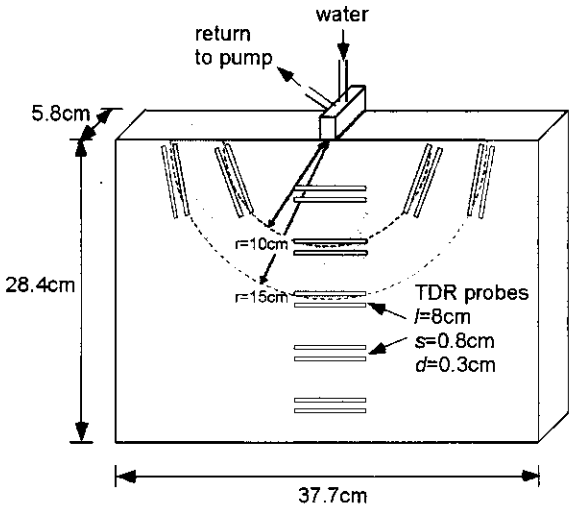

Figure 5-1. Experimental apparatus for matrix wetting experiment

5.2 Experimental Results and Discussion

Some photographs at selected times are presented in Photograph 5-1(A)-(G). The dark area is the wet region. As can be seen, the migration speeds in the horizontal and vertical directions were the same, showing a semi-circular wetting front. At t=144hours, the wetting front reached the side boundaries (r=18.9cm). Figure 5-2 shows the water content change with time at the location of the probes. The data from the center probes (vertical distribution) are shown in circles, and those from the left and right side probes are denoted by triangles and squares, respectively. Before t=96hrs, water content values at r=10cm were almost the same, except that the probe on the right side was showing slightly higher values. This slight disagreement is probably due to material heterogeneity and is not necessarily due to gravity effects. The data at r=15cm were almost identical in all directions.

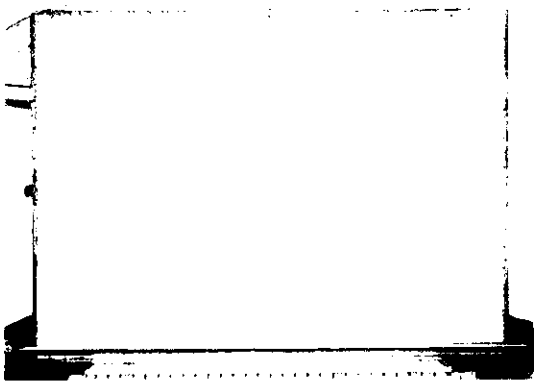

(a) t = 0hours

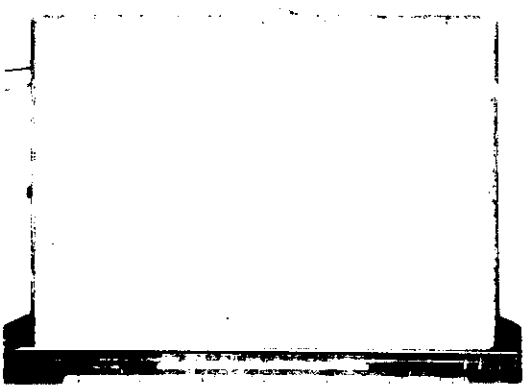

(a) t = 0hours (back)

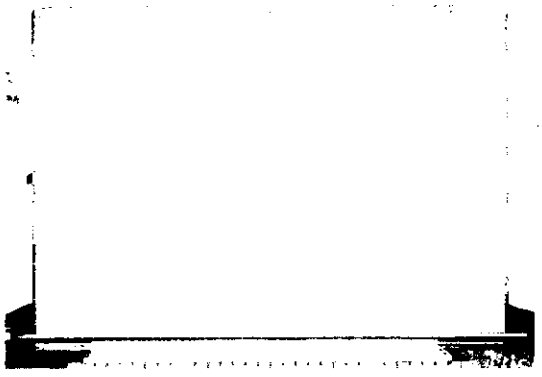

(b) t = 1hours

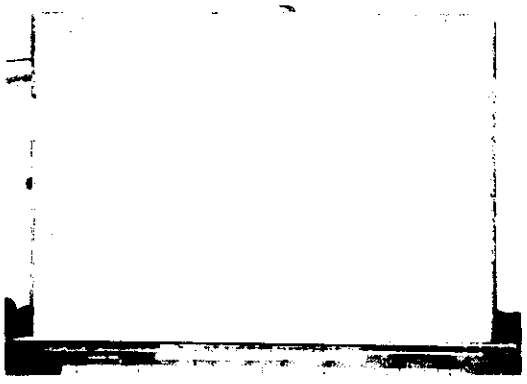

(b) t = 1hours (back)

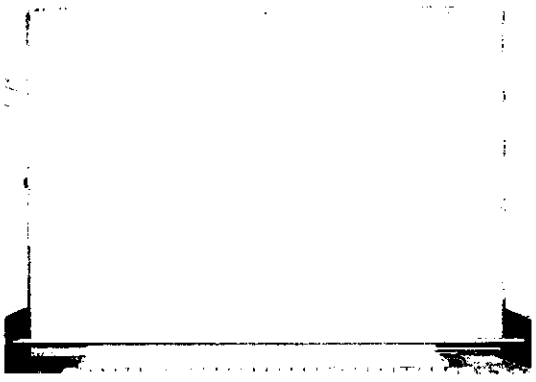

(c) t = 2hours

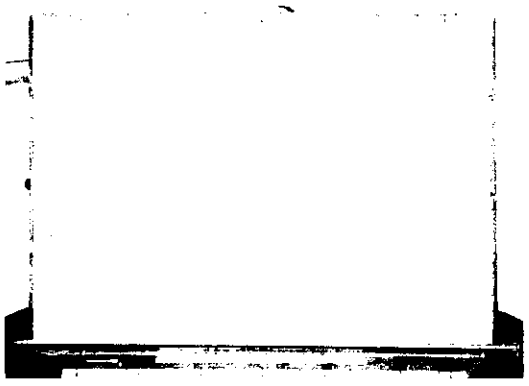

(c) t = 2hours (back)

Photo 5-1(A). Wetting front migration at selected times

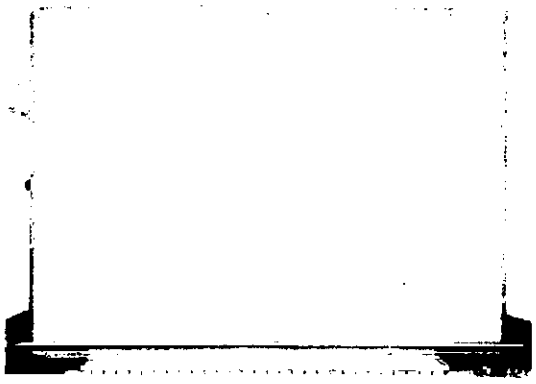

(d) t = 3hours

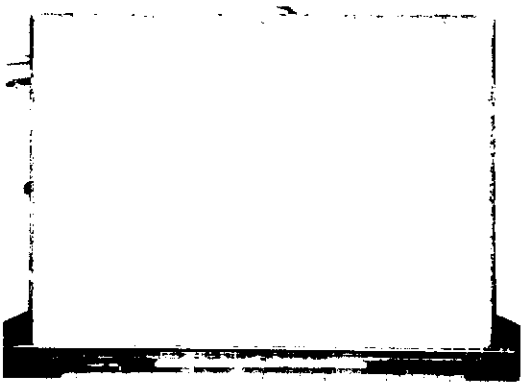

(d) t = 3hours (back)

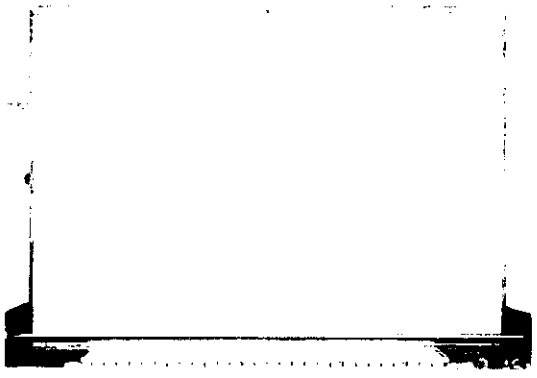

(e) t = 4hours

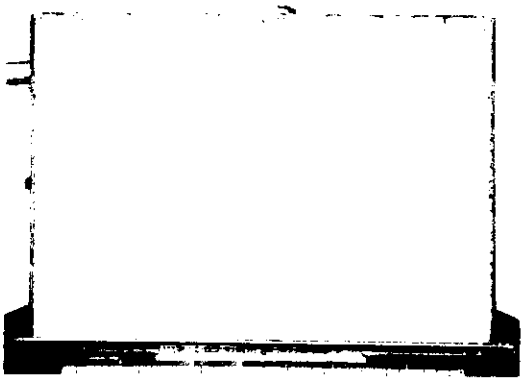

(e) t = 4hours (back)

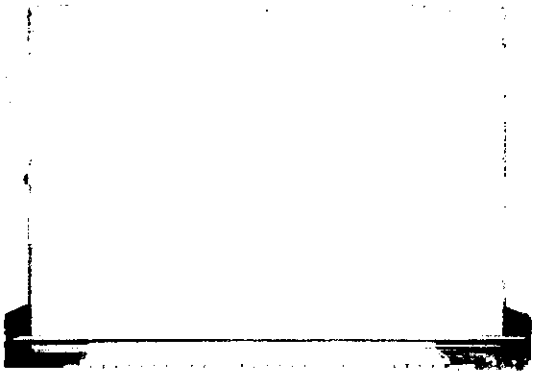

(f) t = 6hours

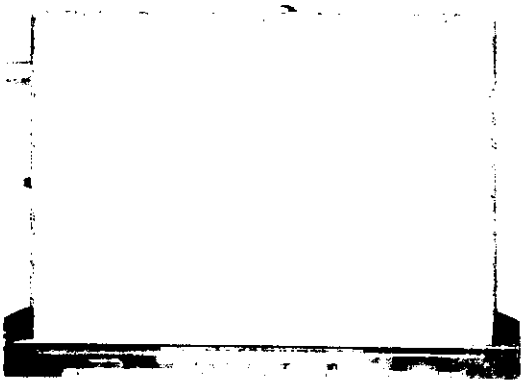

(f) t = 6hours (back)

Photo 5-1(B). Wetting front migration at selected times

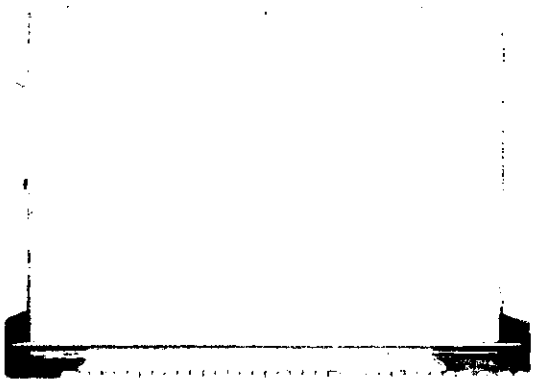

(g) t = 9hours

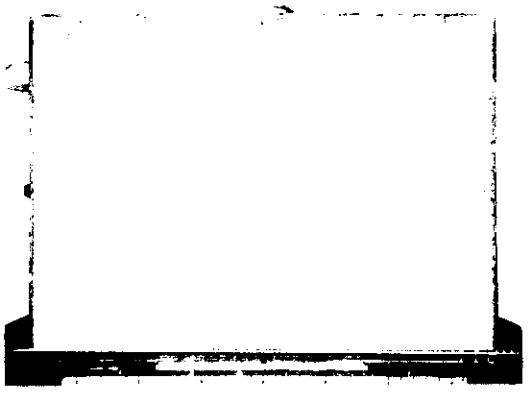

(g) t = 9hours (back)

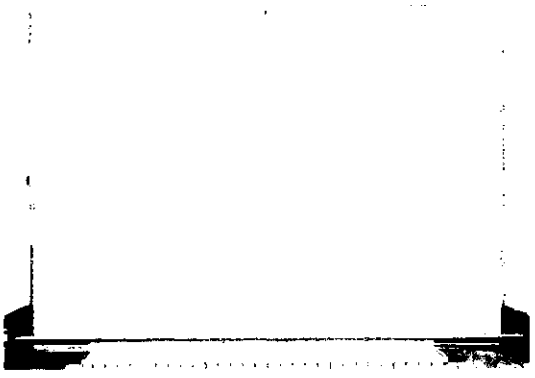

(h) t = 12hours

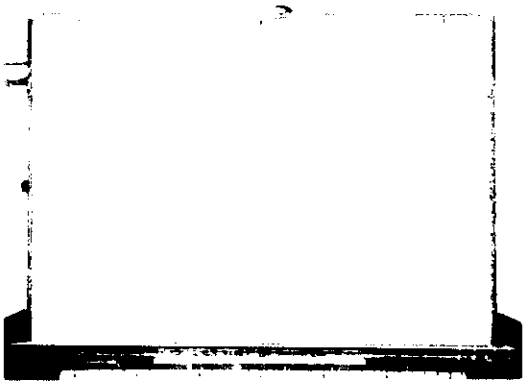

(h) t = 12hours (back)

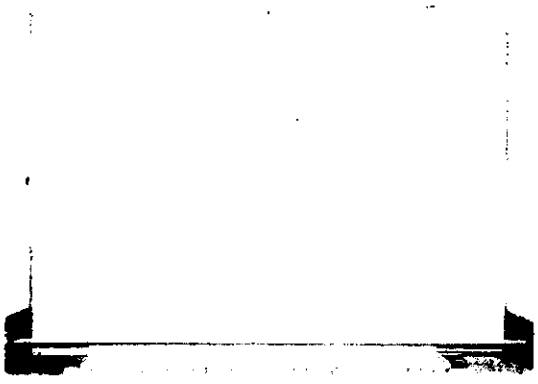

(i) t = 24hours

(i) t = 24hours (back)

Photo 5-1(C). Wetting front migration at selected times

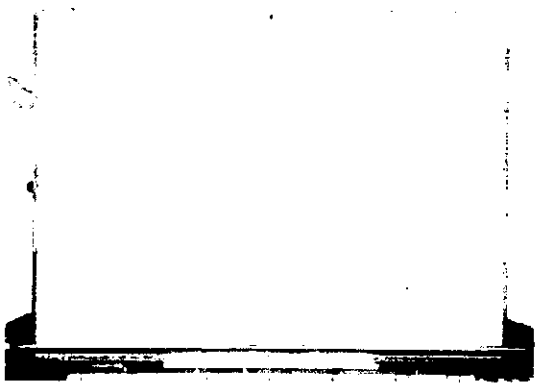

(j) t = 36hours

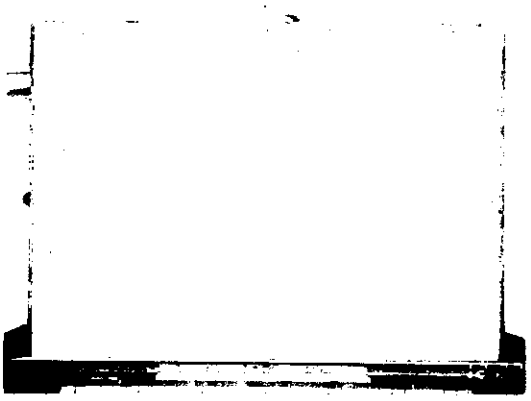

(j) t = 36hours (back)

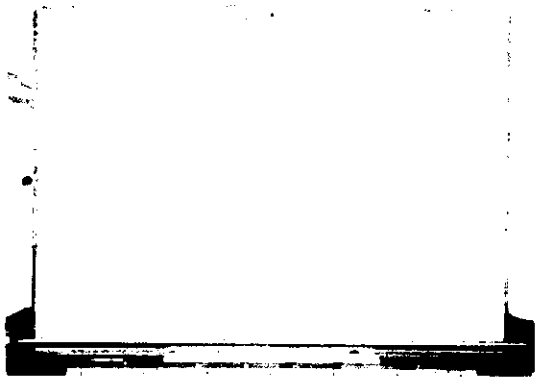

(k) t = 48hours

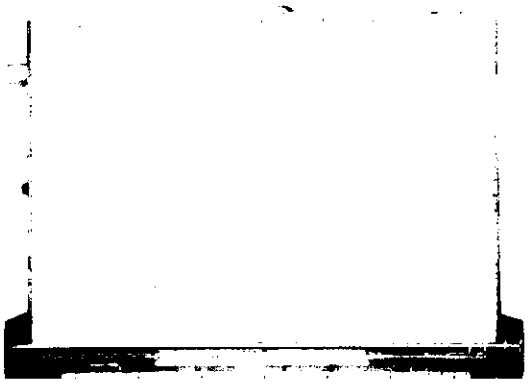

(k) t = 48hours (back)

(l) t = 72hours

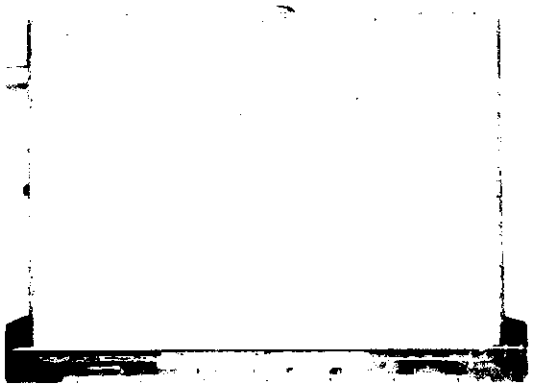

(l) t = 72hours (back)

Photo 5-1(D). Wetting front migration at selected times

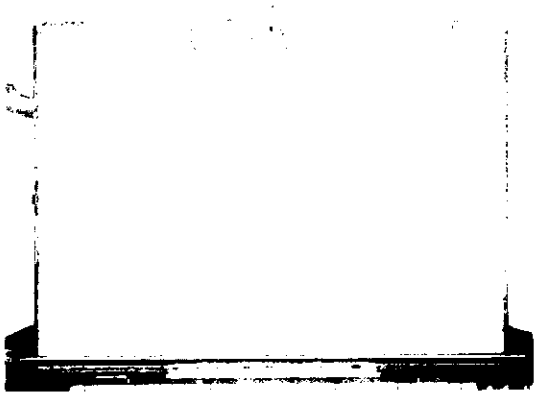

(m) t = 4days

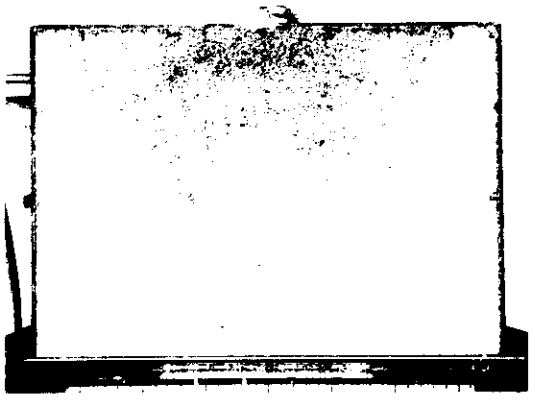

(m) t = 4days (back)

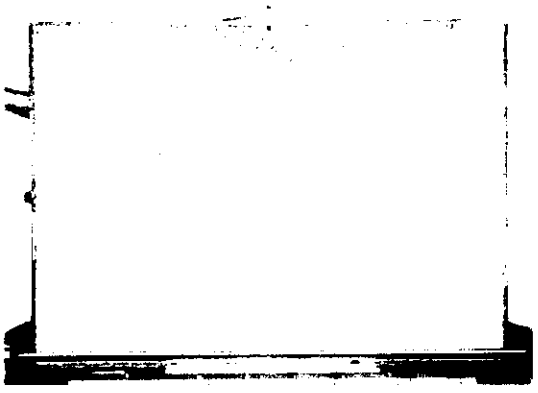

(n) t = 5days

(n) t = 5days (back)

(o) t = 6days

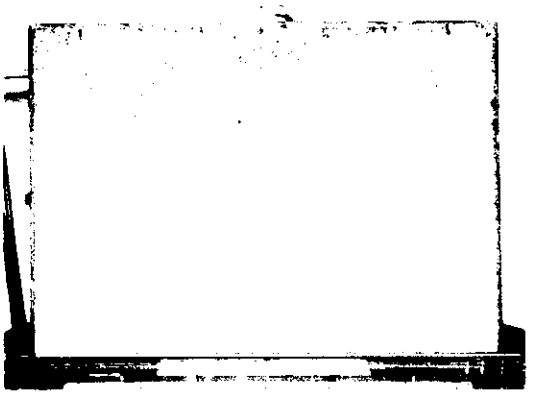

(o) t = 6days (back)

Photo 5-1(E). Wetting front migration at selected times

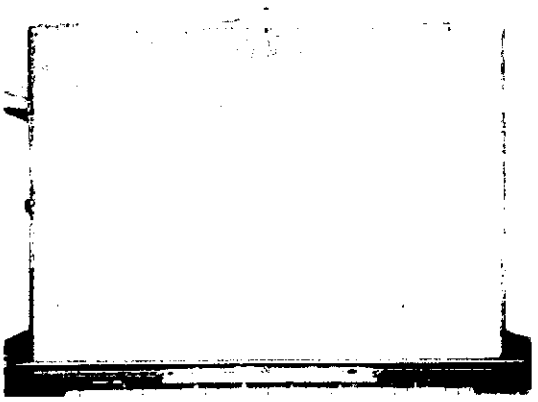

(p) t = 7days

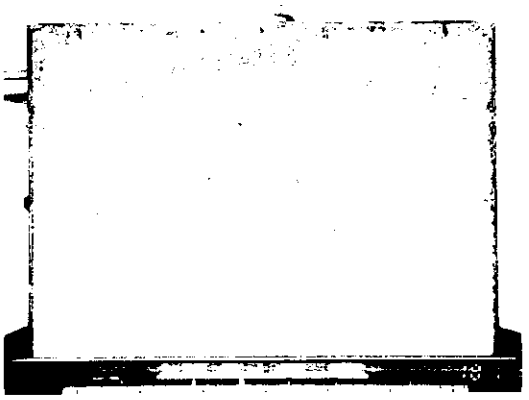

(p) t = 7days (back)

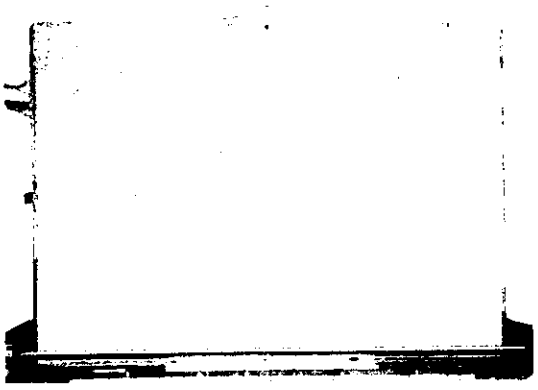

(q) t = 8days

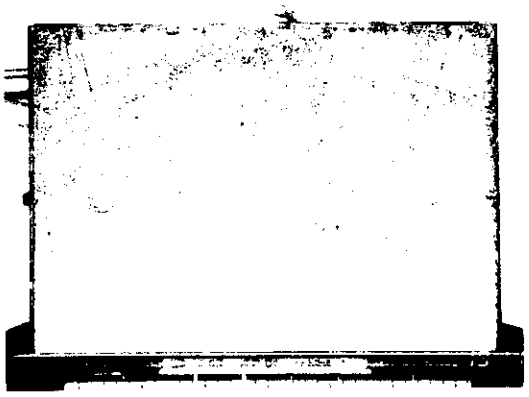

(q) t = 8days (back)

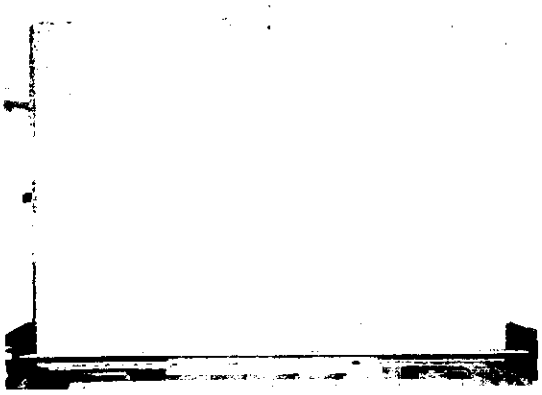

(r) t = 9days

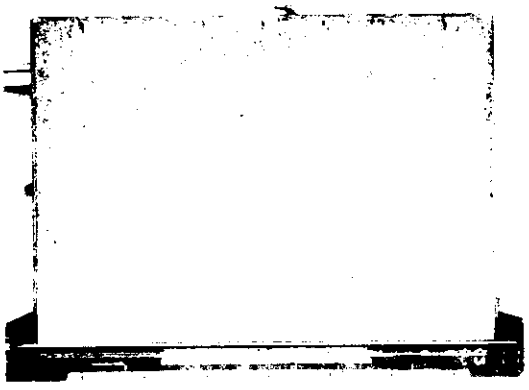

(r) t = 9days (back)

Photo 5-1(F). Wetting front migration at selected times

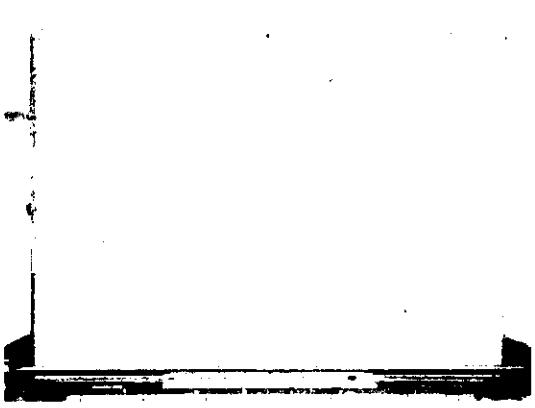

(s) t = 10days

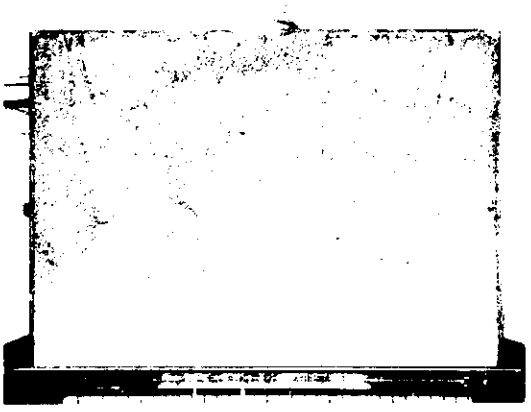

(s) t = 10days (back)

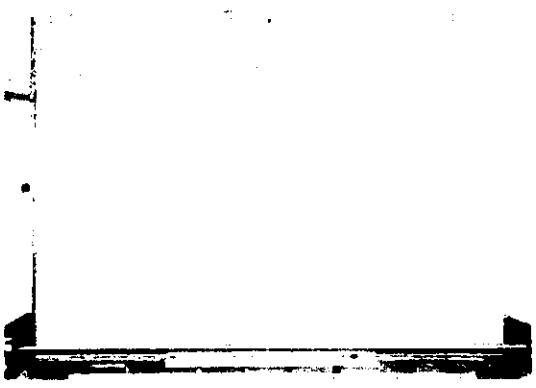

(t) t = 14days

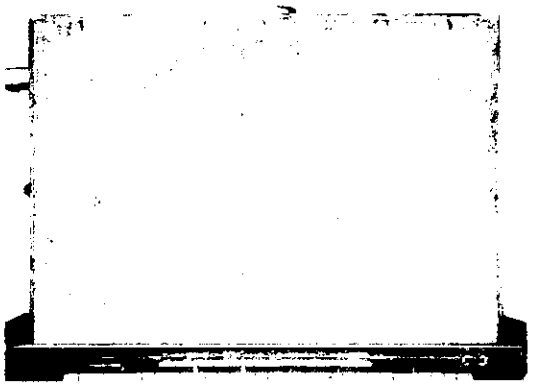

(t) t = 14days (back)

Photo 5-1(G). Wetting front migration at selected times

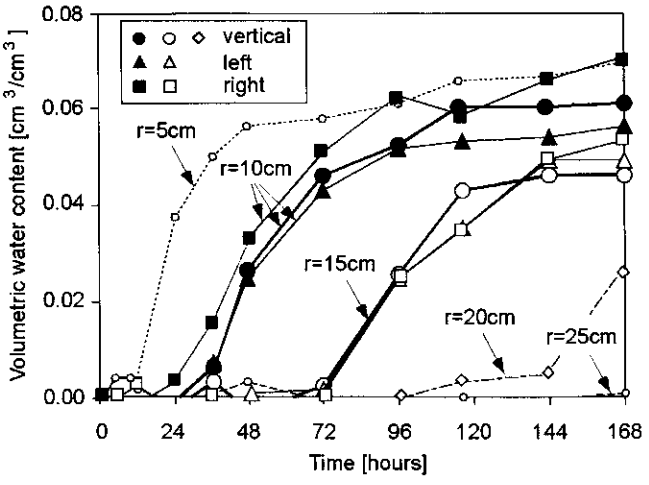

Figure 5-2. Water content change with time in vertical and horizontal directions

In general, rock is less hydraulically conductive than soil due to smaller pore sizes. The smaller pore size induces a larger suction gradient. Therefore, these results suggest that the suction gradient is dominant over gravity driven flow in dry rock. The neglect of gravity driven flow in the rock matrix seems appropriate for fractured rock masses. However, in the fractures themselves, gravity driven flow, including instabilities are potentially very important.

5.3 Summary

In the matrix wetting experiment, the wetting front was semi-circular and migrated in a radial direction. The water content measurement revealed that the water content distributions in the matrix were almost the same in the horizontal and vertical directions. These results qualitatively suggest that the effect of gravity is small and a large suction gradient is dominating the flow in a low permeability rock matrix. The neglect of gravity driven flow in the rock matrix seems to be appropriate for fractured rock masses, and makes the non-linear diffusion equation approach meaningful.

6. Single-Fracture Experiment (Wetting)

6.1 Experimental Apparatus and Measurement Method

As the simplest case of a fracture-matrix system, a single-fracture system was considered. A schematic view of the apparatus is shown in Figure 6-1. Two Indiana limestone blocks with dimensions of 16.8(W) x 26.8(H) x 5.3(D)cm were used. The effective porosity of the block was approximately n=14% and, it was cut using a diamond saw. The blocks were air-dried at room temperature ($24 \pm 1°C$) for more than two weeks in the laboratory, where the relative humidity was approximately 10-15%. The blocks were mated together to form a vertical fracture in the middle. A spacer film with a thickness of 0.1mm was used to ensure a uniform and known aperture. During the experiments, the blocks were completely covered by acrylic plates to avoid evaporation from the surfaces. At the top end of the fracture, water was injected at a constant rate and the bottom end was exposed to atmospheric pressure.

Eight TDR probes were aligned on the right-side block as shown in Figure 6-1. It was expected that the wetting front would migrate horizontally from the fracture due to large matrix suction. Therefore, the probes were aligned in such a way that the water content distribution in the horizontal direction can be measured. Each probe has a length of L=10cm and measures the mean water content along the probe.

Two wetting experiments were carried out with different water flow rates, to investigate the effect of flow rate on the infiltration from the fracture to the matrix. The first experiment (exp#1) had a water flow rate of 2.2cm^3/min. The second exp (exp#2) employed a flow rate of 4.0cm^3/min. The infiltration rate can be obtained by differentiating the Philip's equation (eq. 2.10) with respect to time. Using S=0.032cm/min^2, the inflow rates above exceed the infiltration rate at t=4.3min for exp#1 and t=1.29min for exp#2, respectively. Therefore, in both cases, the infiltration will be

"matrix-controlled".

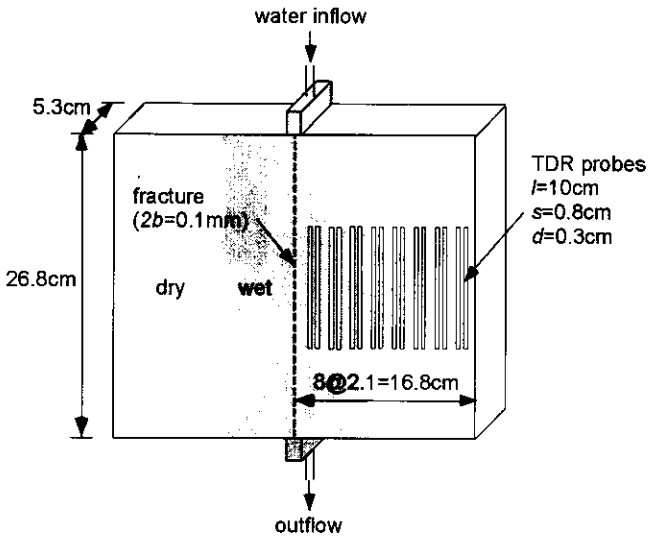

Figure 6-1. Single-fracture experiment apparatus (Wetting)

6.2 Experimental Results and Discussion (exp#1)

A series of photographs are presented in Photograph 6-1(A)-(C) (some are dark due to low exposure). The dark area is the wet region. The wetting front was nearly parallel to the fracture and penetrated in the horizontal direction, although at early times it was not perfectly uniform. The horizontal penetration of the wetting front suggests that the effect of gravity is small and the flow is driven by the suction gradient. At t=60hours, the wetting front reached the boundary at x=16.8cm, after which the wetting behavior would be affected by the boundary.

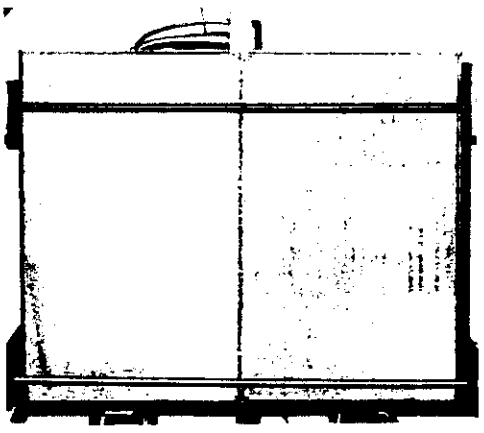

(a) t=0hours

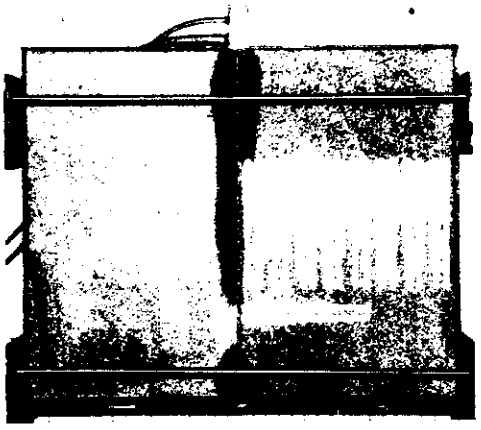

(b) t=1hours

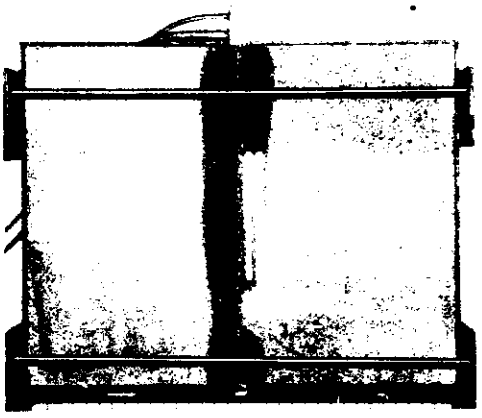

(c) t=2hours

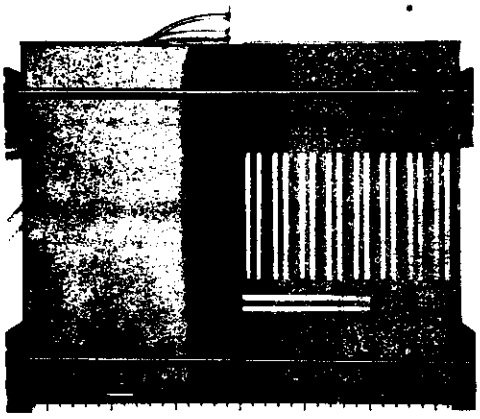

(d) t=4hours

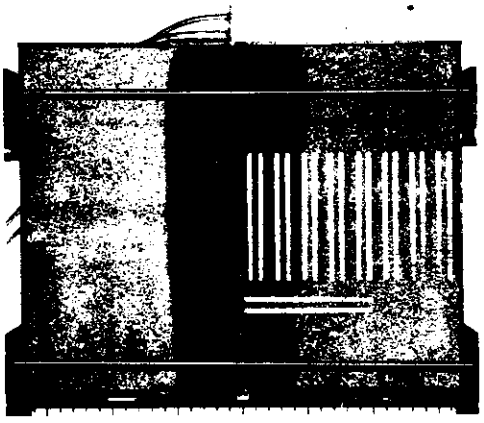

(e) t=6hours

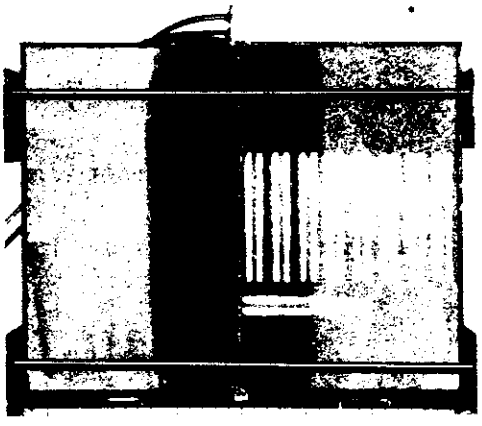

(f) t=9hours

Photo 6-1(A). Wetting front migration at selected times (exp#1)

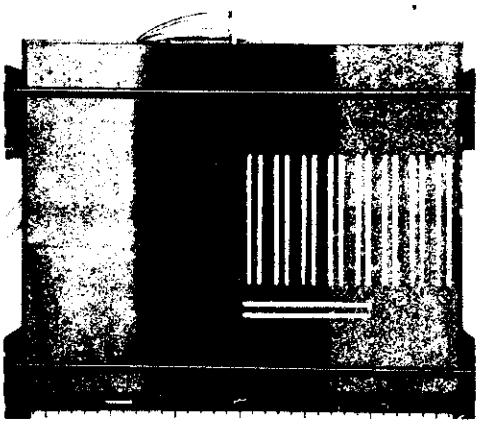

(g) t=12hours

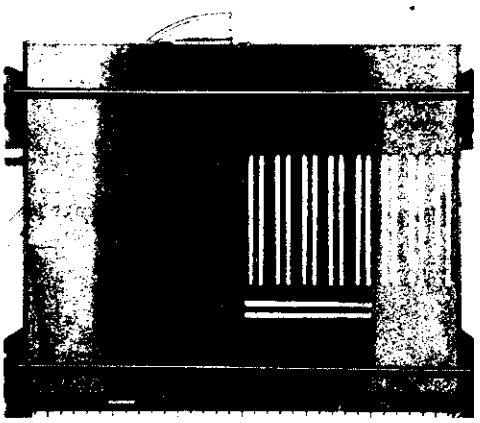

(h) t=24hours

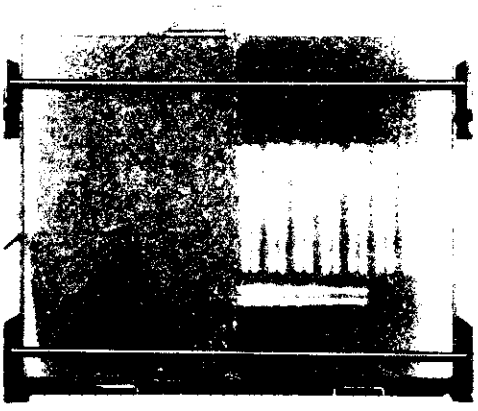

(i) t=48hours

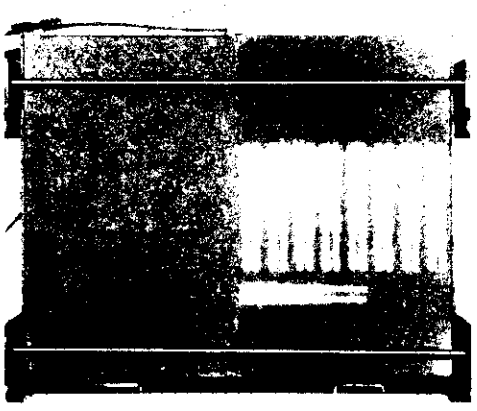

(j) t=60hours

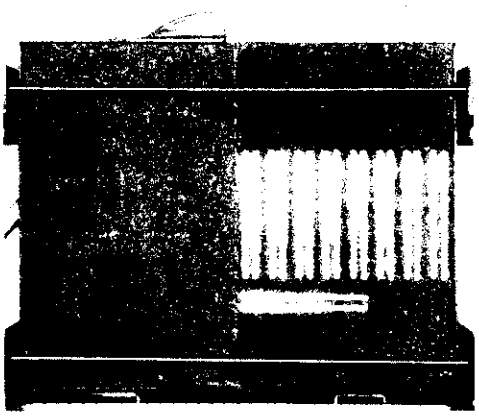

(k) t=72hours

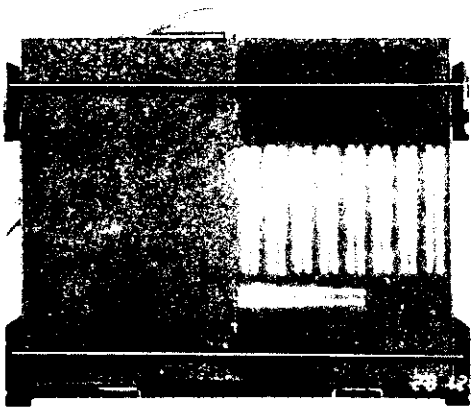

(l) t=96hours

Photo 6-1(B). Wetting front migration at selected times (exp#1)

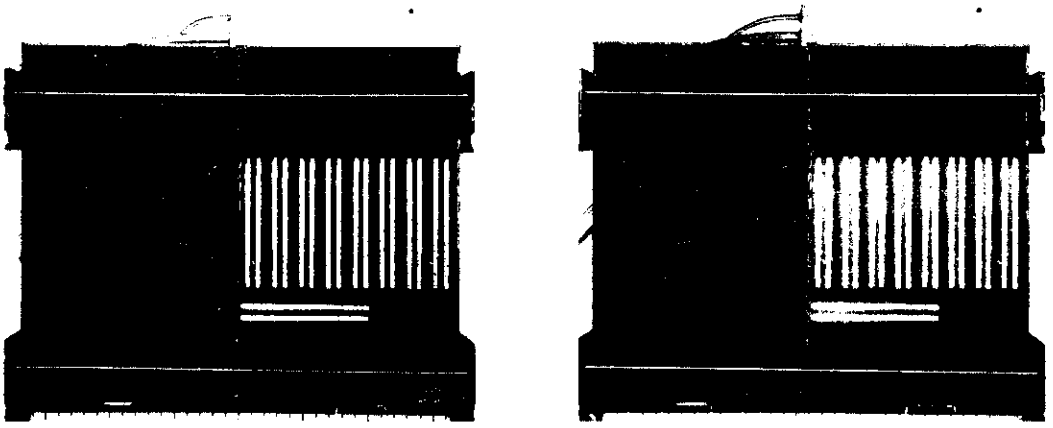

(m) t=132hours (n) t=168hours

Photo 6-1(C). Wetting front migration at selected times (exp#1)

Figure 6-2 shows the water content distributions in the right-side block on which the probes were installed at selected times. The Y-axis (i.e., x=0) corresponds to the location of the fracture. After the wetting front passed, water content immediately increased up to θ=0.1 (65% of saturation) and further increased gradually. This is consistent with the results from the static imbibition experiment mentioned previously (Figure 4-7).

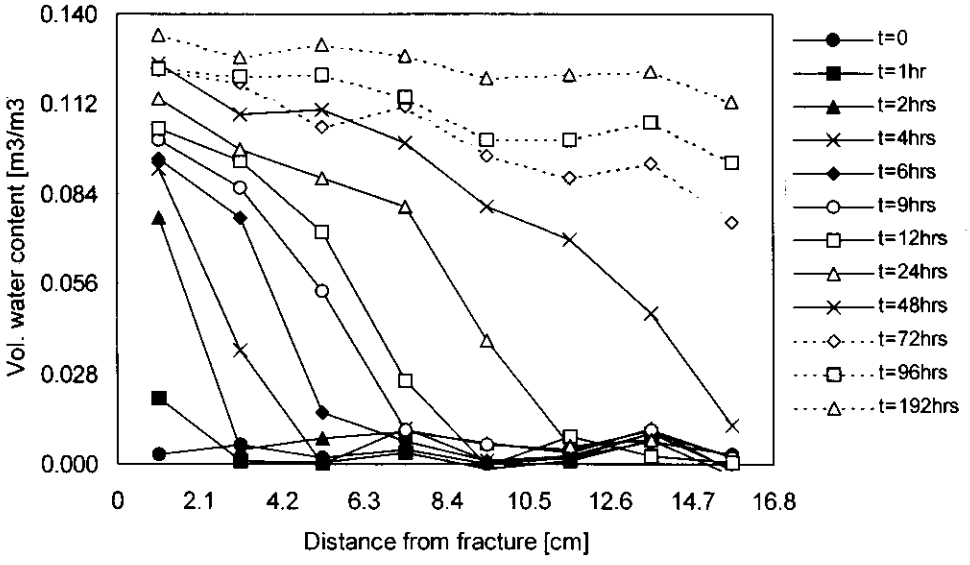

Figure 6-2. Water content distribution (Wetting exp.#1)

The plot of cumulative infiltration $I(t)$ vs. $time^{1/2}$ in Figure 6-3 shows that $I(t)$ is proportional to $t^{1/2}$ until the wetting front reaches the boundary of the block at t=60hours(thus, $t^{1/2}$=7.7hour$^{1/2}$). The linear relationship was still observed until t=84hours (thus, $t^{1/2}$=9.2hour$^{1/2}$). There is good agreement between $I(t)$ obtained from the difference between the inflow and outflow rates (denoted as I-O in the graph) and $I(t)$ obtained from the TDR measurement. The macroscopic imbibition from a fracture to matrix until the front reaches the boundary, can be quantified by the *Philip's equation*. In this particular case, the value of the sorptivity was found to be S = 0.026cm/min$^{1/2}$. This is slightly less than the 0.033cm/min$^{1/2}$ value obtained from the sorptivity experiment. This is probably because of the slight difference in material and perhaps because the water was not absorbed from the entire fracture surface, but only a part of it, due to possible fingering phenomena within the fracture. Figure 6-4 shows the change of infiltration $i(t)$ rate with time, which is simply the time derivative of $I(t)$. The infiltration rate also tends to follow the Philip's equation well.

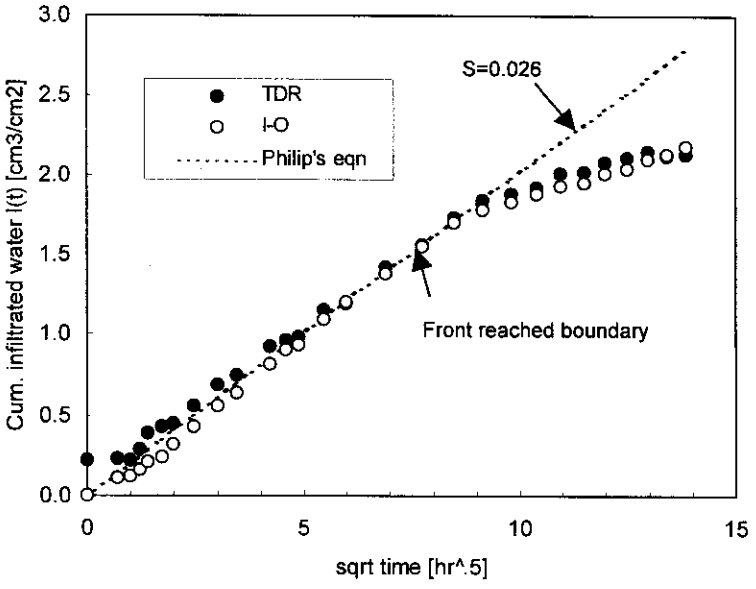

Figure 6-3. Cumulative infiltration $I(t)$

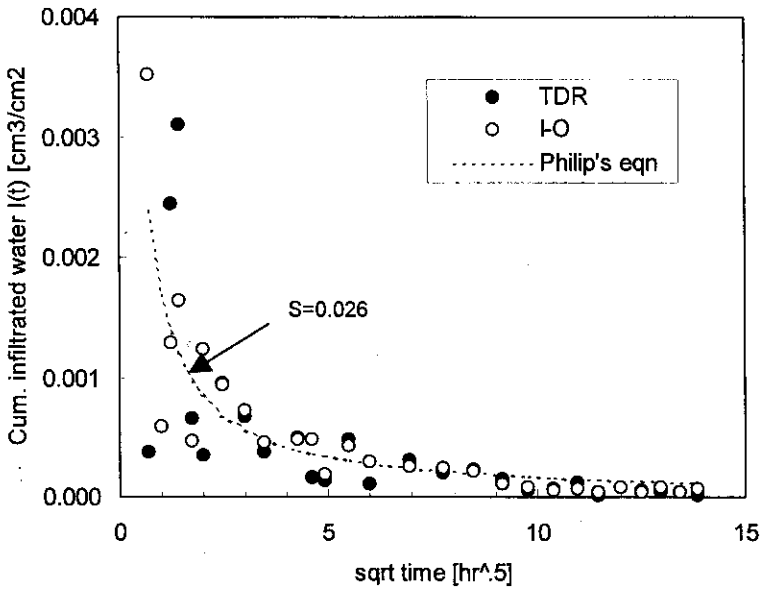

Figure 6-4. Infiltration rate *i(t)*

Figure 6-5 shows the time trend of outflow from the system. At the beginning, since the matrix was dry and its suction was very large, a large portion of water (e.g., 44% at t=0.5hours) flowing through the fracture was absorbed by the matrix. After 12hours, roughly 96% of water was coming out of the system, showing that most of the water was just passing through the system without being absorbed by the matrix. This outflow would consequently flow into the next system in a real fractured rock mass.

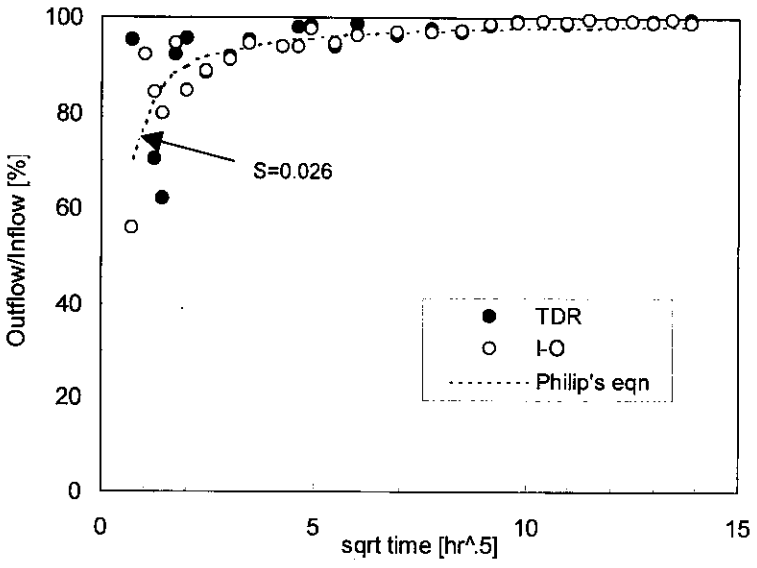

Figure 6-5. Outflow/Inflow rate

6.3 Experimental Results and Discussion (exp#2)

A series of photographs for exp#2 are presented in Photograph 6-2(A)-(C). Most of the results are nearly identical to the previous case (exp#1). The wetting front was nearly parallel to the fracture and penetrated in the horizontal direction showing small gravity effect. At t=48-60hours, the wetting front reached the boundary at x=16.8cm, after which the wetting behavior would be affected by the boundary.

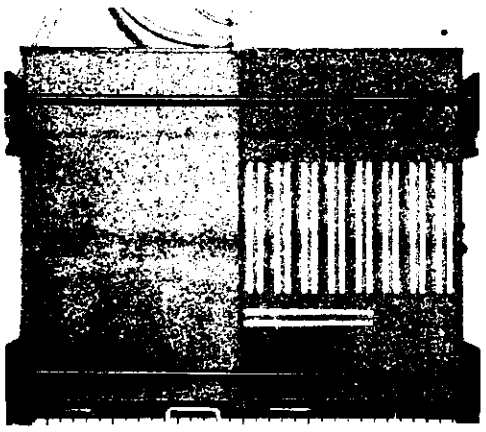

(a) t=0hours

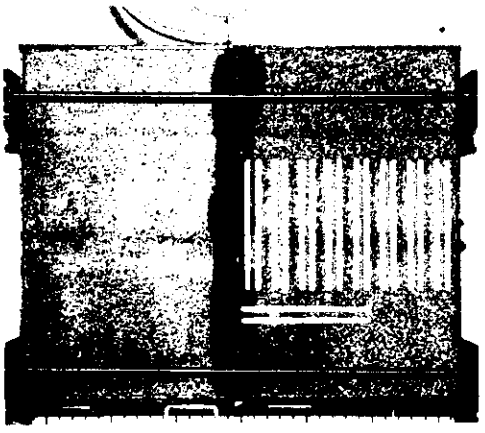

(b) t=1hours

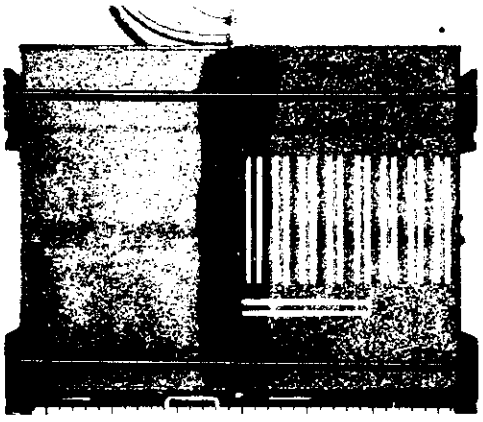

(c) t=2hours

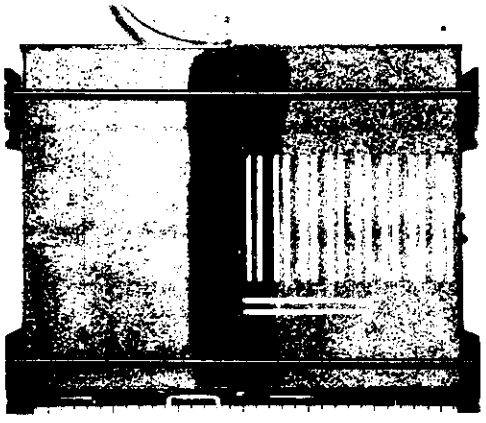

(d) t=3hours

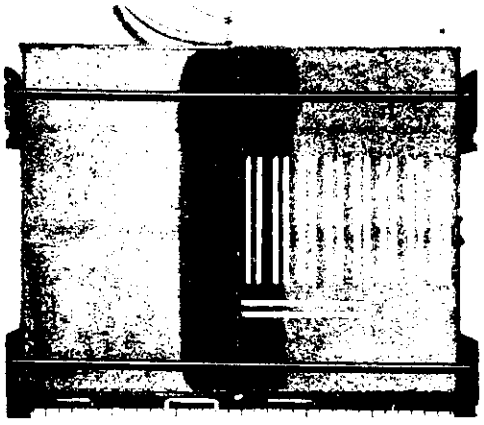

(e) t=4hours

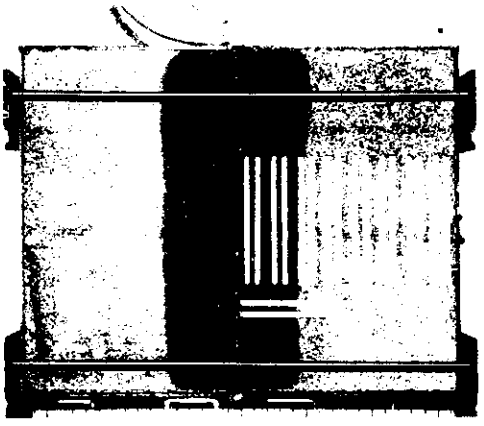

(f) t=6hours

Photo 6-2(A). Wetting front migration at selected times (exp#2)

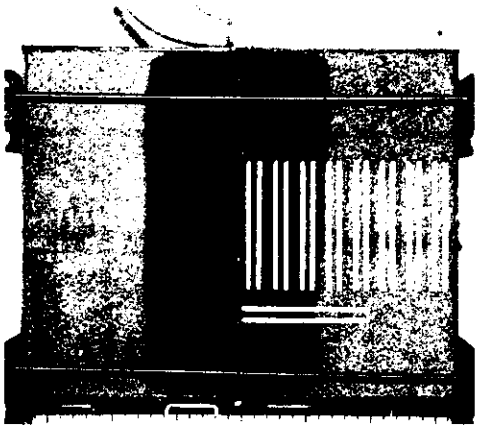

(g) t=9hours

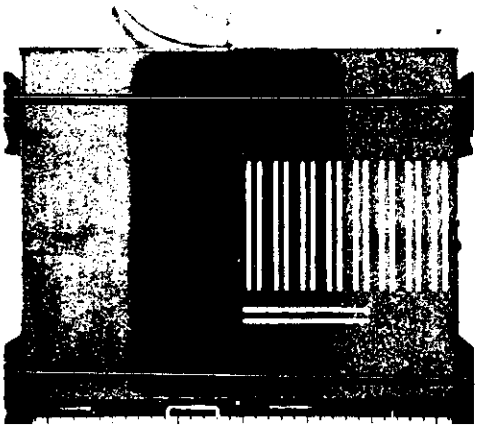

(h) t=12hours

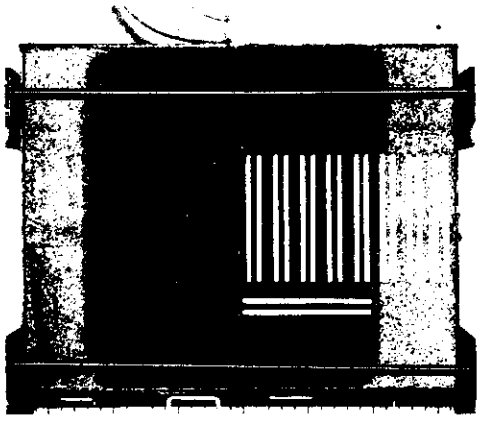

(i) t=24hours

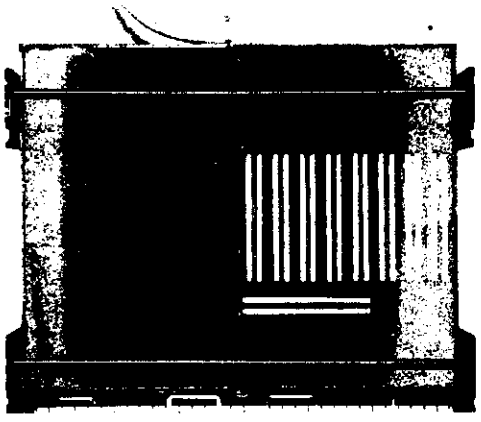

(j) t=30hours

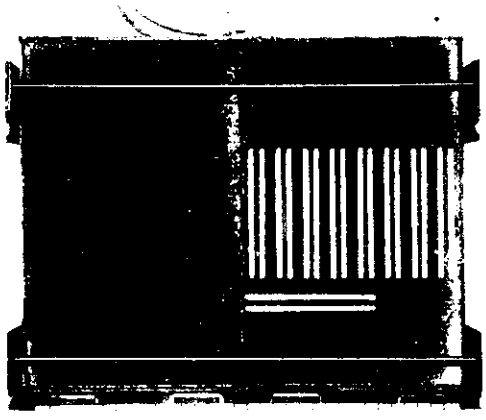

(k) t=48hours

(l) t=77hours

Photo 6-2(B). Wetting front migration at selected times (exp#2)

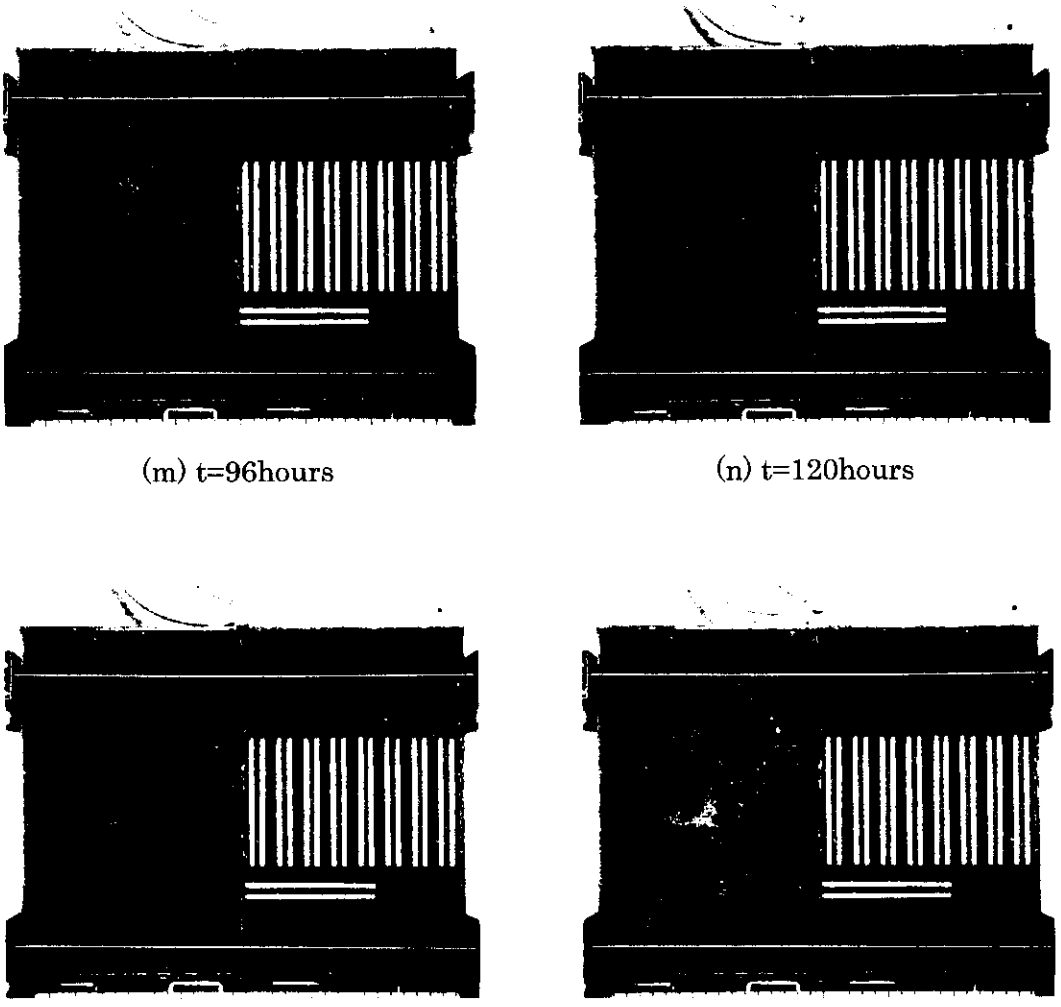

(m) t=96hours (n) t=120hours

(o) t=144hours (p) t=192hours

Photo 6-2(C). Wetting front migration at selected times (exp#2)

Figure 6-6 shows the water content distributions in the right-side block at selected times. The Y-axis (i.e., x=0) corresponds to the location of the fracture. After the wetting front passes, water content immediately increases up to 65% or more. This is, again very similar to the previous case (exp.#1).

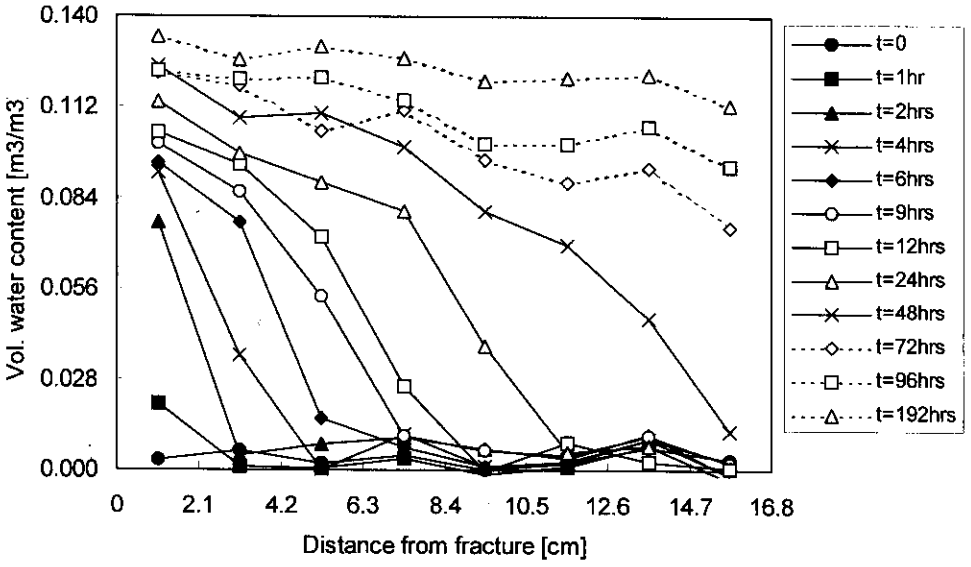

Figure 6-6. Water content distribution (Wetting exp.#1)

The cumulative infiltration $I(t)$ vs. $time^{1/2}$ in Figure 6-7 shows that $I(t)$ is proportional to $t^{1/2}$ until the wetting front reached the boundary of the block at t=60hours(thus, $t^{1/2}$=7.7hour$^{1/2}$). The macroscopic imbibition from a fracture to matrix until the front reaches the boundary can be quantified by the Philip's equation. In this particular case, the value of the sorptivity was found to be S = 0.026cm/min$^{1/2}$, which is identical to that obtained in exp#1. Figure 6-8 shows the change of infiltration $i(t)$ rate with time, that also tends to follow the Philip's equation.

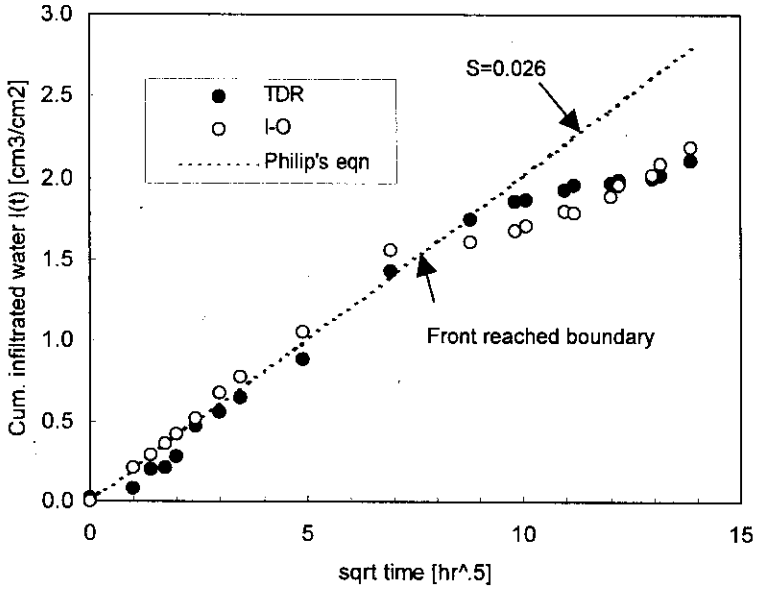

Figure 6-7. Cumulative infiltration *I(t)*

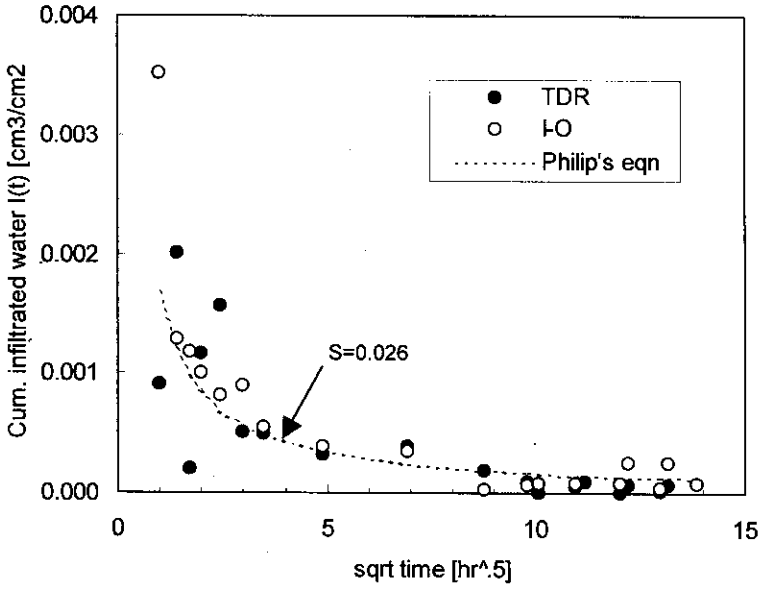

Figure 6-8. Infiltration rate *i(t)*

Figure 6-9 shows the time trend of outflow from the system. At the beginning, since the matrix was dry and its suction was very large, a large portion of water (e.g., 77% at t=0.5hours) flowing through the fracture was absorbed by the matrix. In the

previous case, 44% was flowing out at t=0.5hours. For both cases, the amount of water absorbed is the same because of the same sorptivity values. However, since the inflow rate at the fracture entrance is higher for exp#2, more water is forced to come out of the system without being absorbed by the matrix. After 12hours, roughly 96% of water was coming out of the system showing that most of the water was just passing through the system without being absorbed by the matrix.

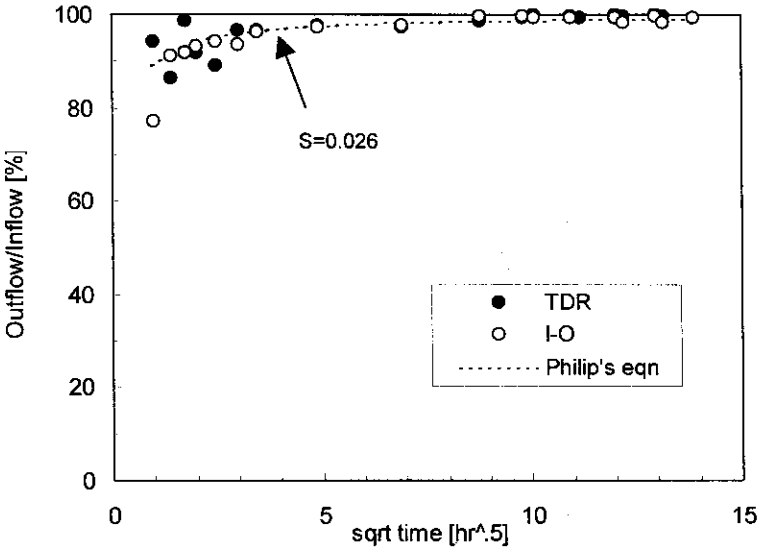

Figure 6-9. Outflow/Inflow rate

6.4 Summary

The infiltration of water into the porous rock matrix from a single flowing fracture was predominantly one-dimensional and in the horizontal direction, thus confirming that gravity driven flow can be neglected. The cumulative infiltration and the infiltration rate followed the Philip's equation until some time after the wetting front reached the boundary. The fact that the effect of gravity is small suggests that the non-linear diffusion equation approach will be appropriate for water flow in the matrix

in large fractured rock masses.

At early times, the matrix absorbed a large fraction of the water. After a certain time, most of water came out of the system without being absorbed by the matrix. This outflow would consequently flow into the next system in a real fractured rock mass. Fracture-matrix interaction thus alters the hydraulic properties of a fractured rock mass until some time after the imbibition starts. In other words, the fracture-matrix system works as a damper such that a sharp excitation such as an episodic precipitation event results in very high absorption and low outflow. In contrast, the damping effect becomes smaller in the case of a sustained continuous precipitation event. However, this picture can be further modified in a large-scale fracture system, where the aperture variability in natural fractures triggers gravitational instability of an infiltration front within the fracture. In our experiment, due to the limited size and fairly uniform fracture, such features were not observed.

The amount of water flowing through the system is larger in exp#1 than the previous case where inflow rate was nearly half. Nonetheless, both cases yielded the same sorptivity. This implies that the amount of water to be absorbed by the matrix is independent of the amount of water flowing through the fracture, when the flow rate is sufficiently large (the "matrix-controlled" case mentioned previously). In such cases, the Philip's equation allows us to quantitatively relate the cumulative infiltration $I(t)$ to $t^{1/2}$ by a single parameter 'sorptivity'. This information is of great importance when predicting the travel time of solutes through unsaturated fractured rock masses. For cases where flow rate in fracture is less than the matrix imbibition rate, further investigation is necessary.

7. Single-Fracture Experiment (Drying)

7.1 Experimental Apparatus and Measurement Method

For the single-fracture drying experiments, the apparatus illustrated in Figure 7-1 was used. It was identical to the one used in the wetting experiments except that the blocks were initially wet and dry air was pumped through the fracture. Two drying experiments were carried out with different dry air flow rates to investigate the influence of the air flow rate on the evaporation behavior from the fracture. In the first experiment (exp#1), which was initiated 24hours after the wetting exp.#1 was stopped, the air flow rate was 700cm^3/min. In the second experiment (exp#2), initiated 24hours after the wetting exp.#2, an air flow rate of 400cm^3/min was used. During the experiments, the air flow rate and water content distribution were monitored for 28days for exp#1, and 35days for exp#2. For both cases, the blocks were completely covered by acrylic plates to avoid evaporation, except when taking photographs. The air flow rate and water content in the right-side block were measured at pre-determined times.

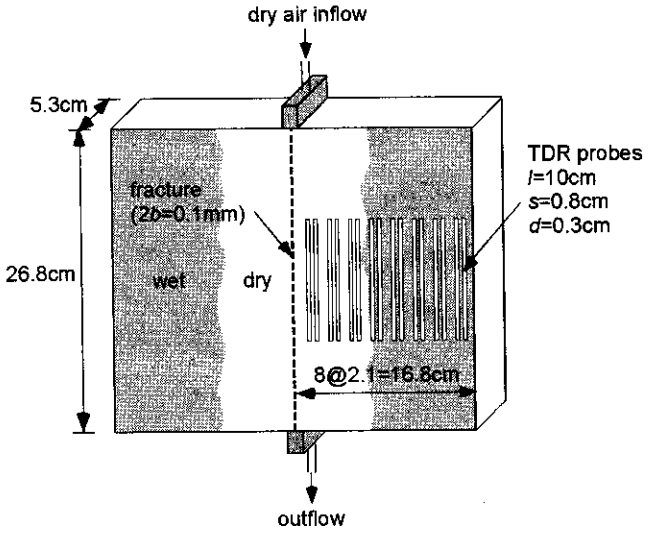

Figure 7-1. Single-fracture experiment apparatus (Drying)

7.2 Experimental Results and Discussion (exp#1)

The first experiment (exp#1) involved an air flow rate of 700cm^3/min for 28 days. A series of photographs at selected times are presented in Photograph 7-1(A)-(C). The drying front first became visible near the inlet at t=4days and was not as distinct as the wetting cases. Its horizontal migration was slightly faster in the upper part of the block, causing a V-shaped front (see photographs). The drying front reached the bottom at t=6days. When Indiana limestone is subjected to drying, it was found that the color change (from dark-wet to light-dry) occurs when saturation becomes roughly less than 20% (thus volumetric water content is 0.028). Therefore, the dark color does not necessarily correspond to high saturations.

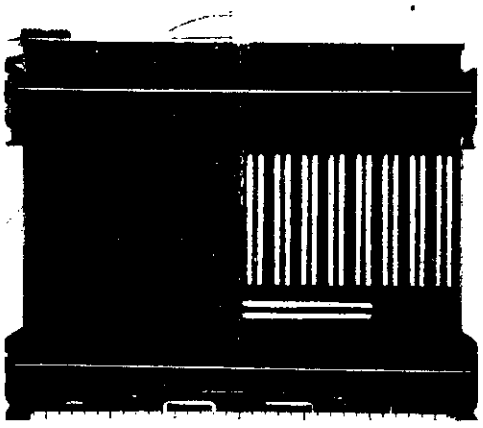

(a) t=0days

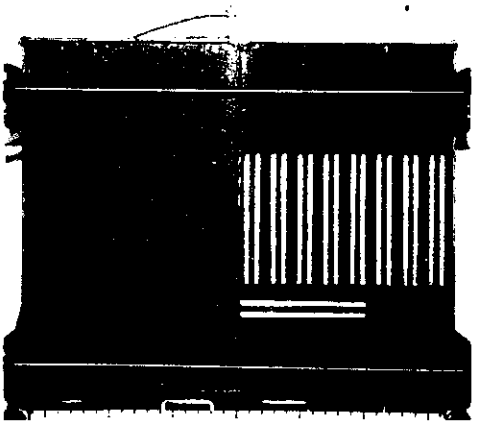

(b) t=3days

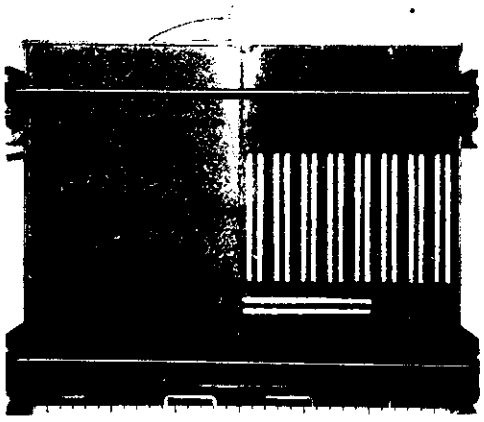

(c) t=4days

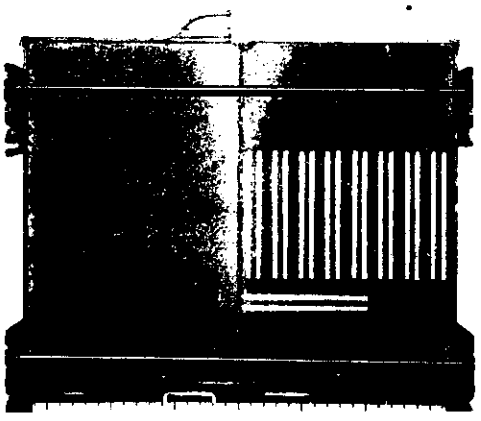

(d) t=4.5days

(e) t=5days

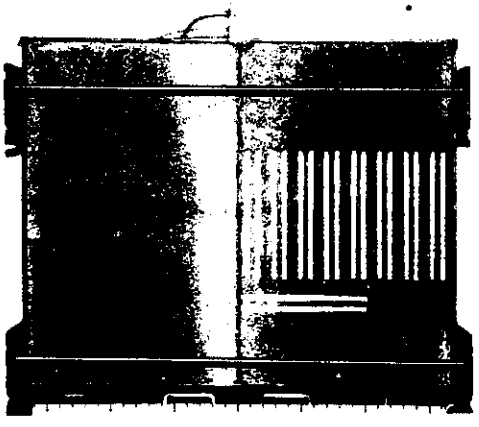

(f) t=6days

Photo 7-1(A). Drying front migration at selected times (exp#1)

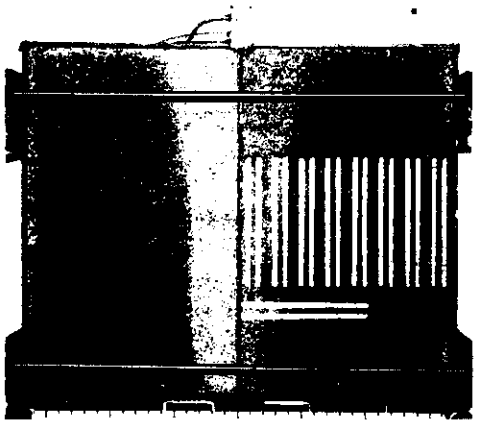

(g) t=7days

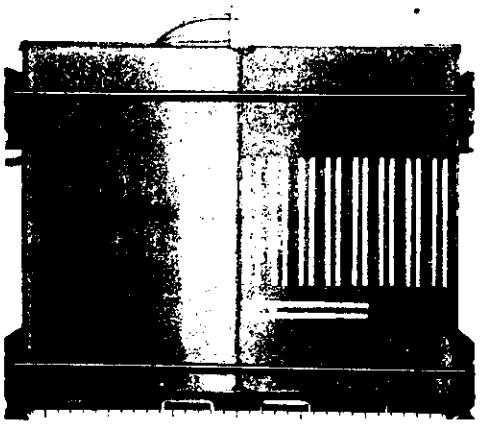

(h) t=8days

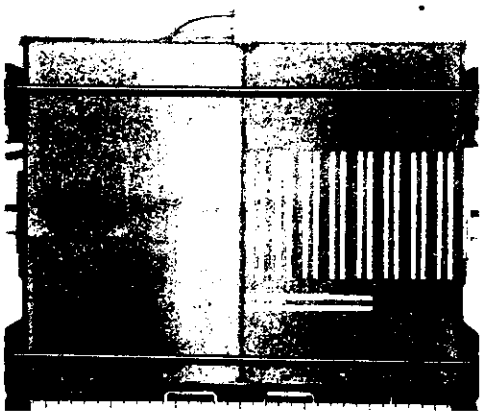

(i) t=9days

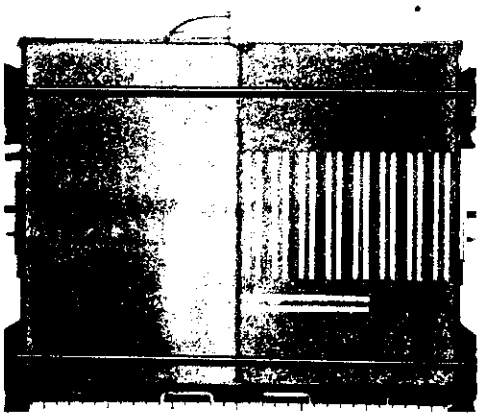

(j) t=10days

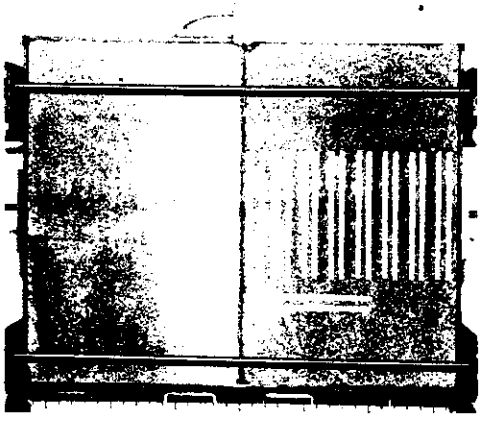

(k) t=11days

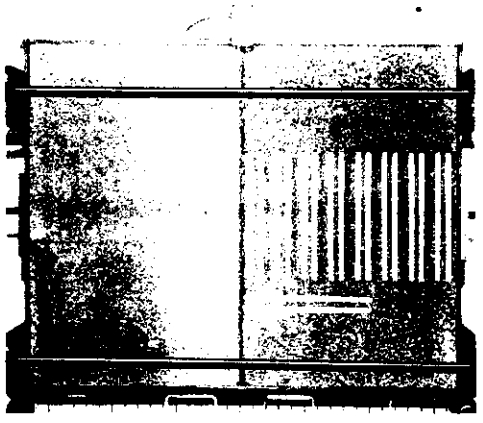

(l) t=12days

Photo 7-1(B). Drying front migration at selected times (exp#1)

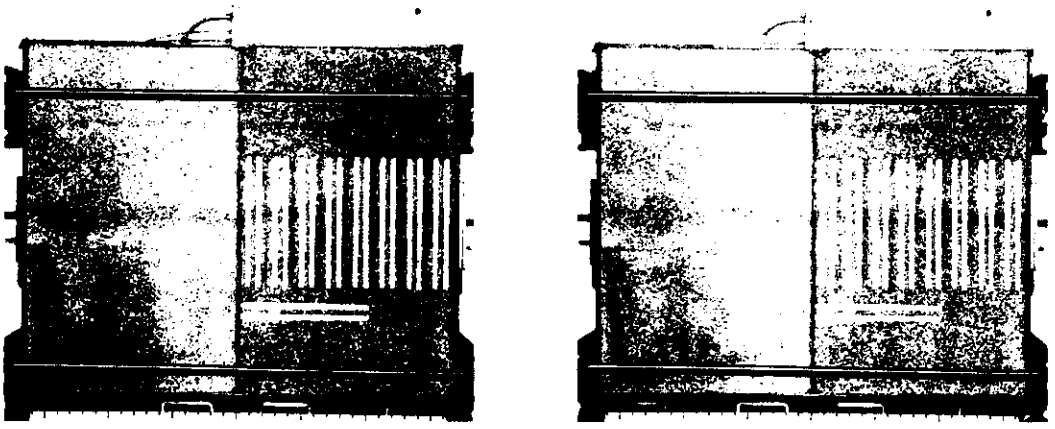

(m) t=13days (n) t=14days

Photo 7-1(C). Drying front migration at selected times (exp#1)

Figure 7-2 shows the one-dimensional water content distributions at selected times. It was very much consistent with the general drying patterns presented in Figure 2-2 except that the water content decreased uniformly within the block at early times due to the boundary effect. This uniform decrease during $0 \leq t \leq$ 3days actually corresponds to Stage I (Figure 2-2) when the system is not semi-infinite but somewhat short. After a certain period of time ($t \leq$ 4days in this case) more distinct drying near the fracture was observed (Stages II and III). According to Figure 2-2, $4 \leq t \leq$ 7days corresponds to Stage II, and $t \geq$ 8days is Stage III. It should be noted that the boundary effect invalidates one of the assumptions (semi-infinite column assumption) on which the Philip's equation is based, as explained below.

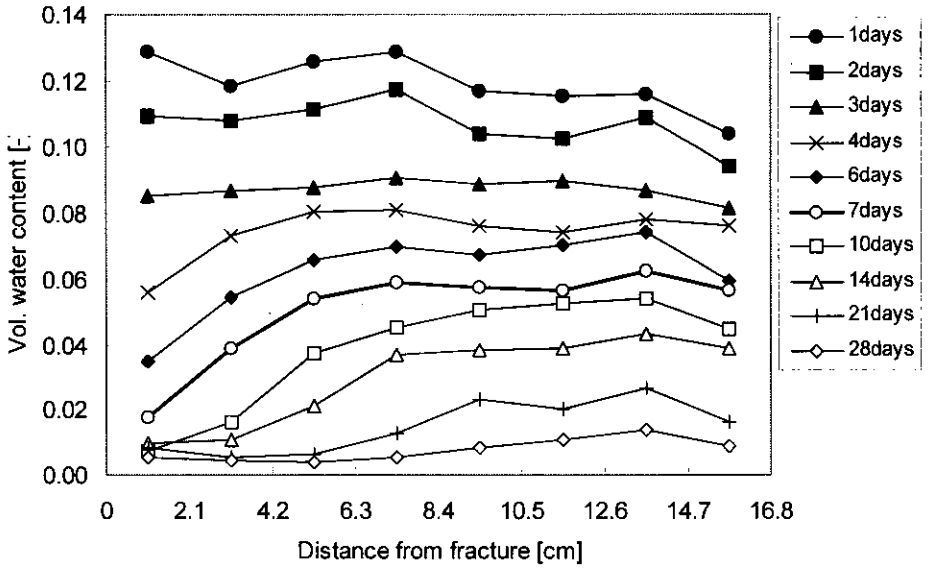

Figure 7-2. Water content distribution (Drying exp.#1)

The cumulative evaporation $E(t)$ is shown in Figure 7-3. The $E(t)$ - $t^{1/2}$ relationship is not as straight as $I(t)$ - $t^{1/2}$ for the wetting cycle. This is because the block has a finite length and one of the boundary conditions on which the Philip's equation is based, is not satisfied. The slope which may be termed as the "desorptivity" was roughly $S_E = 0.013\text{cm/min}^{1/2}$. This is half of the sorptivity and it suggests that it will take roughly four times longer for the same amount of water to evaporate than to be absorbed.

In this case, as mentioned above, one of the boundary conditions on which the Philip's equation is based was not satisfied. In the case of wetting experiment, the wetting front was sharp and no boundary effect was seen until the front reached the boundary. On the other hand, in drying experiments, the water content decreased uniformly within the entire block from the beginning. Thus, the assumption of 'semi-infinite' domain no longer holds. This is the major reason that $E(t)$ was not perfectly proportional to $t^{1/2}$. Numerical simulation of the nonlinear diffusion equation will be appropriate for modeling such a case.

In Figure 7-4, the evaporation rate is shown as a function of the square root of time. Since $E(t)$ was not perfectly proportional to $t^{1/2}$, the evaporation rate $e(t)$ does not follow the Philip's equation, either.

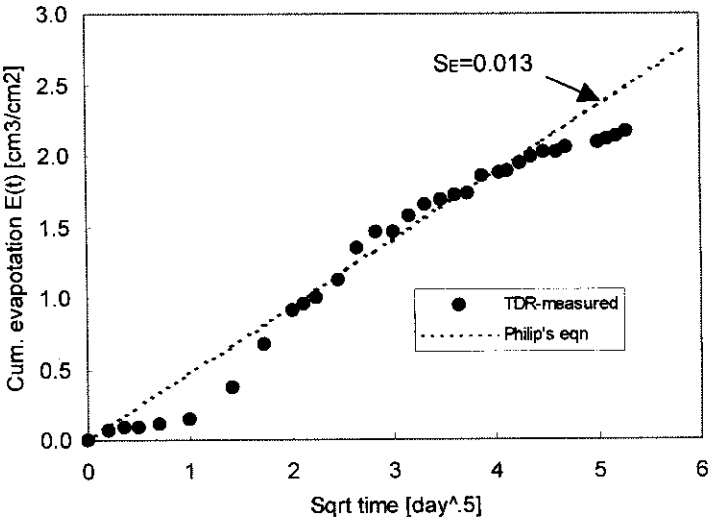

Figure 7-3. Cumulative evaporation $E(t)$

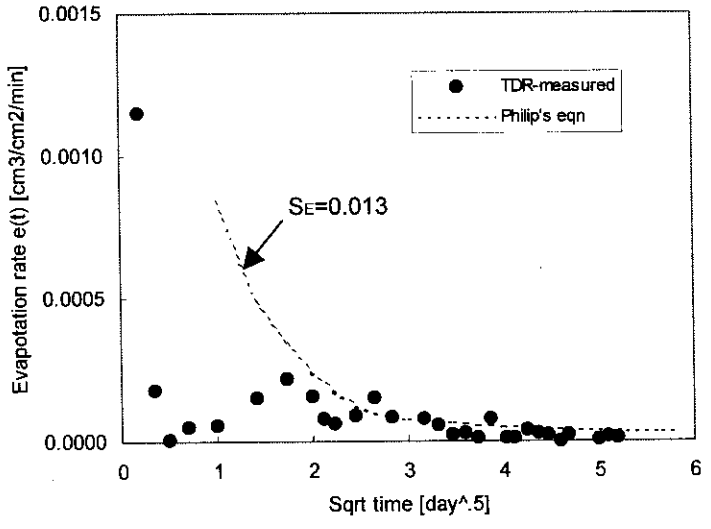

Figure 7-4. Evaporation rate $e(t)$

It should also be mentioned that the dry air flow rate was set to 350cm^3/min during the first 24hours, that can be seen as the distinct increase in the slope at t=1day in Figure 7-3. It was found, however, that the valve controlling the air flow rate was not stable for a such small flow rate. Thus, the flow rate was increased to 700cm^3/min at t=1day. The valve was replaced after exp#1 had been completed. It should be noted that the drying front migration was not perfectly one-dimensional, but due to the alignment of the probes, the measured water content distribution and thus amount of water evaporated may be influenced by some level of measurement errors.

7.3 Experimental Results and Discussion (exp#2)

In the second exp (exp#2), that was initiated 24hours after the wetting exp.#2, a dry air flow rate of 400cm^3/min was used. A series of photographs are presented in Photograph 7-2(A)-(D). Most of the results were similar to the previous case (exp#1) in which the air flow rate was roughly twice as much. The drying front first became visible at t=10days and was not as distinct as the wetting cases. Just like in exp#1, its horizontal migration was slightly faster in the upper part of the block, resulting in a V-shaped wetting front. The V-shape was slightly more distinct than exp#1. This is probably due to the smaller air flow rate for which the vapor density becomes saturated within a short distance. Thus, as the air flows along the fracture, the evaporation rate becomes smaller. After the drying front reached the bottom at t=15days, it migrated predominantly in the horizontal direction. Again, the dark color does not necessarily mean that the region is highly saturated. Due to the smaller air flow rate, the drying speed is slower than in exp#1.

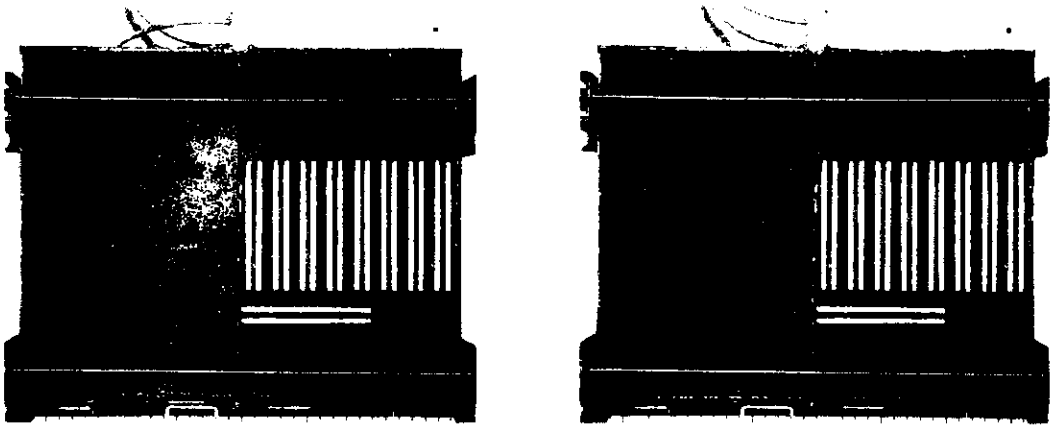

(a) t=0day (b) t=1day

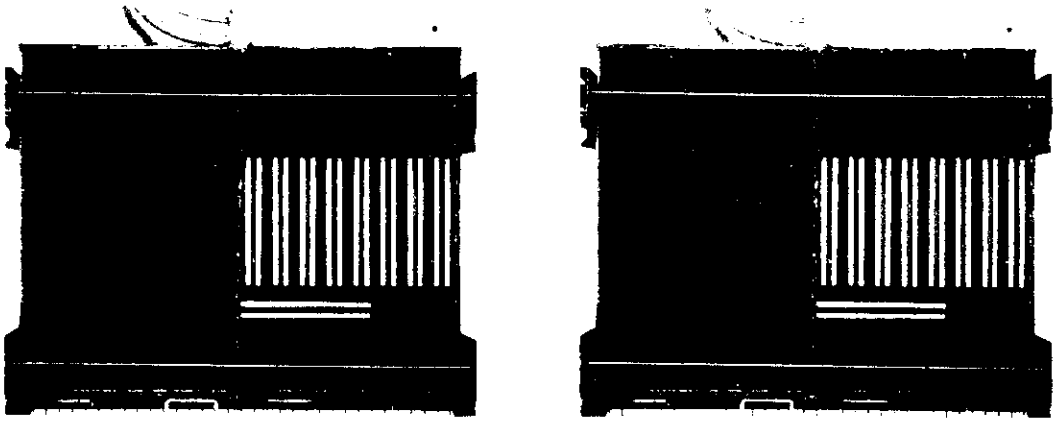

(c) t=2days (d) t=3days

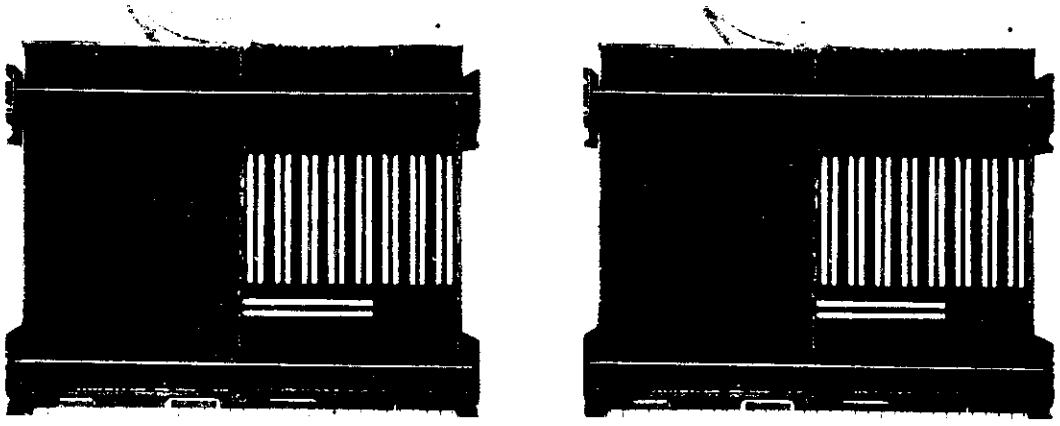

(e) t=4days (f) t=5days

Photo 7-2(A). Drying front migration at selected times (exp#2)

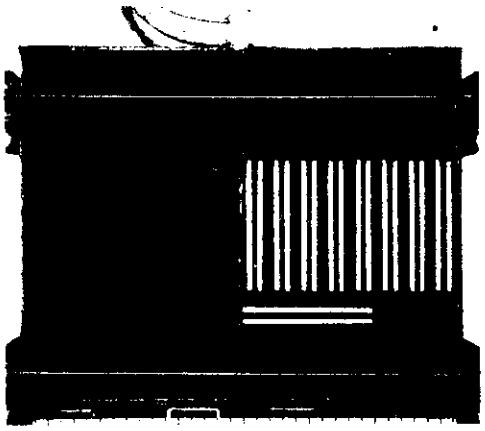

(g) t=6days

(h) t=7days

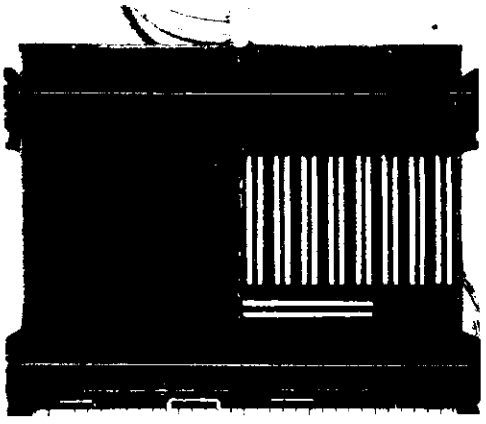

(i) t=8days

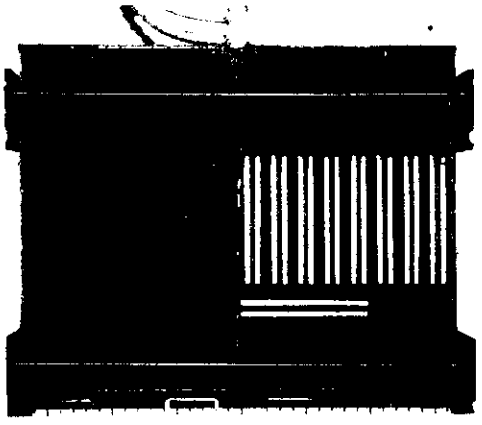

(j) t=9days

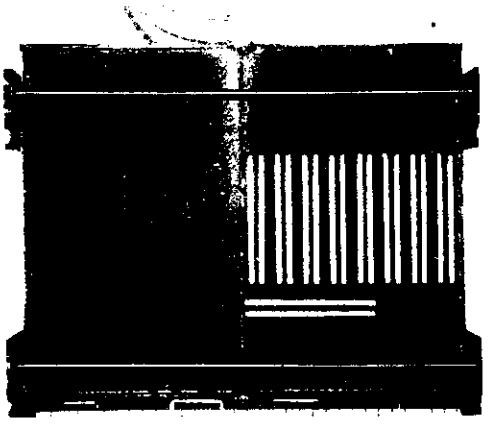

(k) t=10days

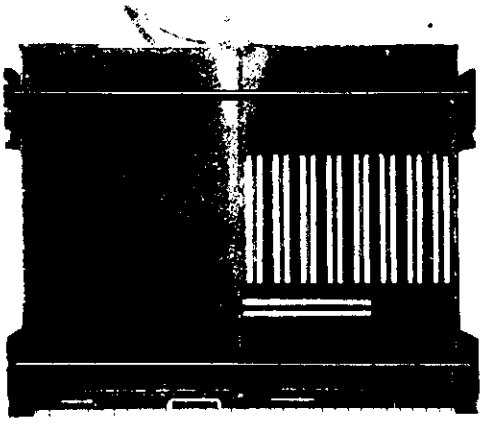

(l) t=11days

Photo 7-2(B). Drying front migration at selected times (exp#2)

(m) t=12days

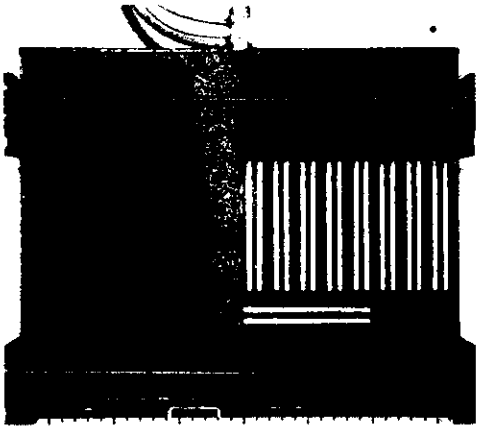

(n) t=13days

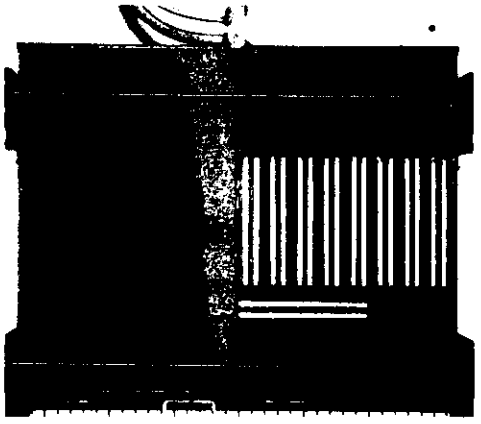

(o) t=14days

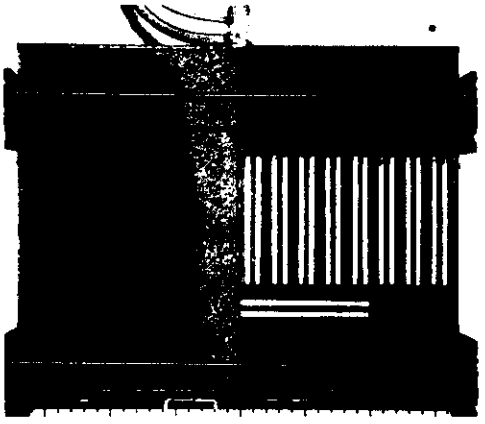

(p) t=15days

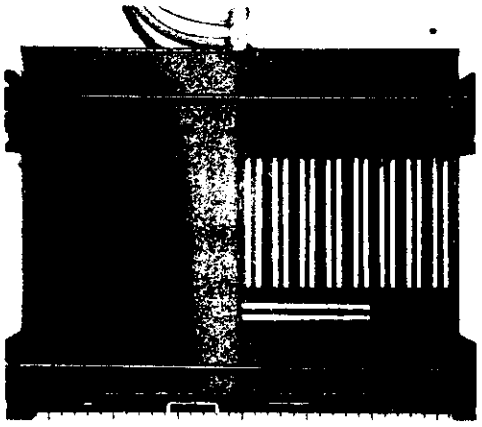

(q) t=16days

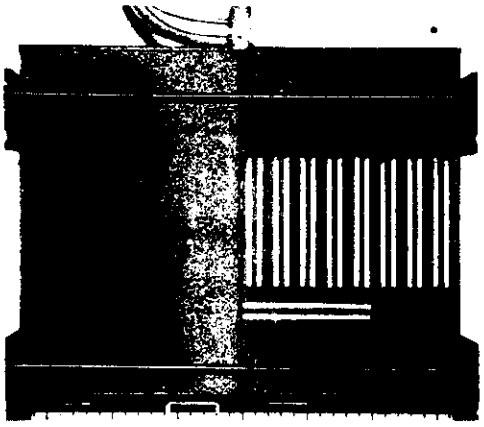

(r) t=17days

Photo 7-2(C). Drying front migration at selected times (exp#2)

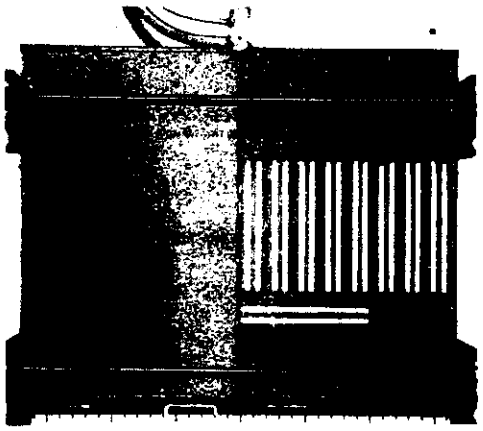

(s) t=18days

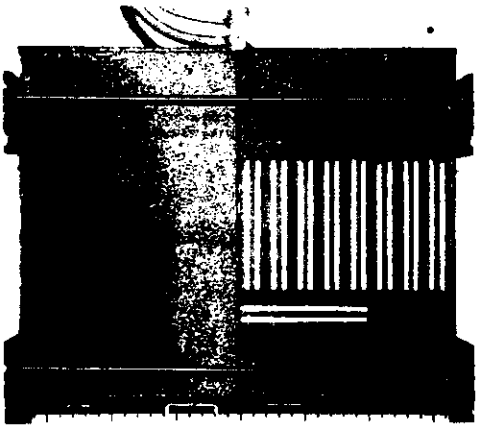

(t) t=19days

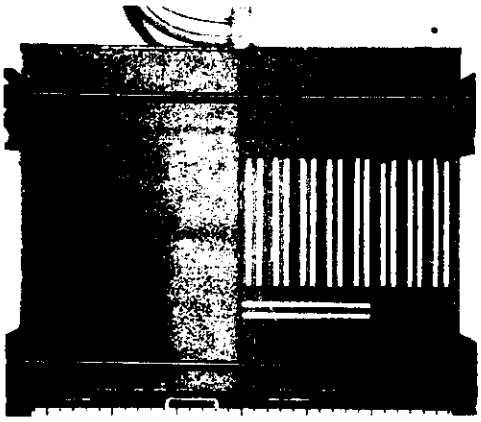

(u) t=20days

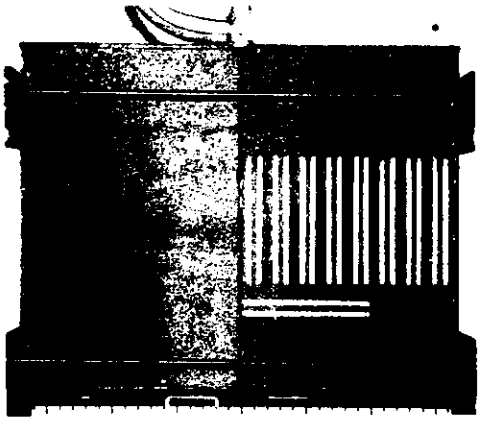

(v) t=21days

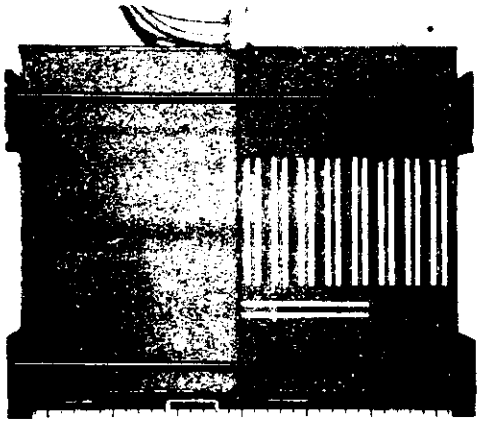

(w) t=28days

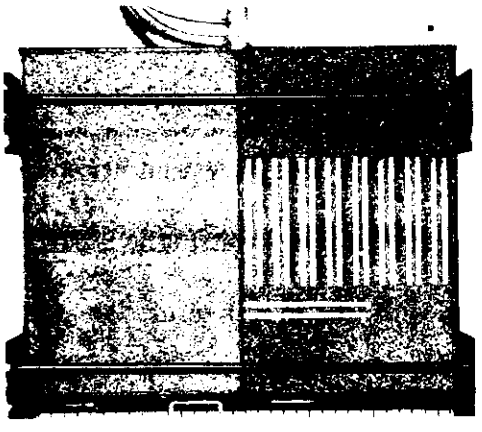

(x) t=35days

Photo 7-2(D). Drying front migration at selected times (exp#2)

Figure 7-5 shows the water content distributions in the right-side block at selected times. It can be seen that the water content decreased uniformly within the block at early times. After a certain period of time ($t \geq$ 11days in this case) more distinct drying near the fracture was observed. According to Figure 2-2, $0 \leq t \leq$ 10days corresponds to Stage I, $11 \leq t \leq$ 21days is Stage II, and $t \geq$ 22days is Stage III. The boundary effect is seen as the uniform decrease during Stage I.

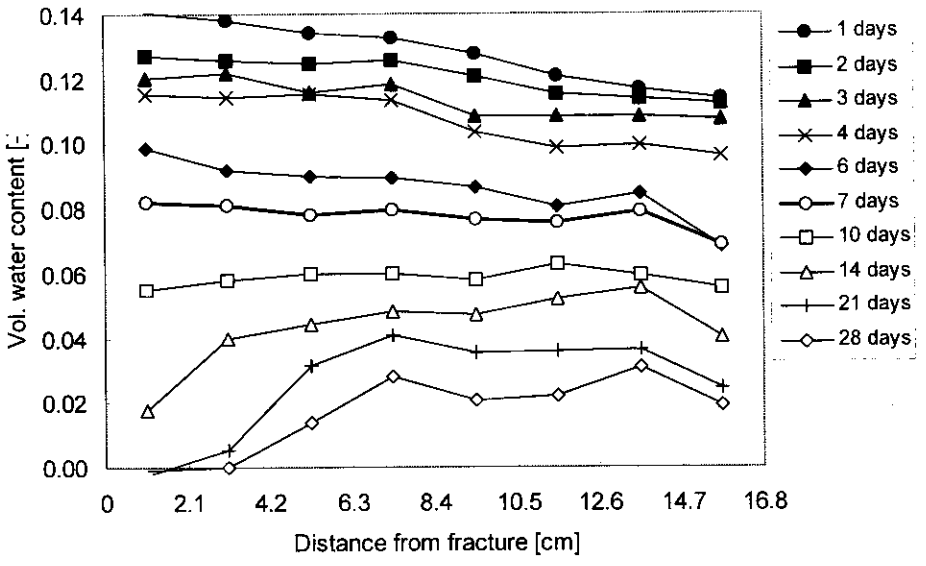

Figure 7-5. Water content distribution (Drying exp.#2)

The cumulative evaporation $E(t)$ is shown in Figure 7-6. The $E(t)$ - $t^{1/2}$ relationship was not as straight as $I(t)$ - $t^{1/2}$ for the wetting cycle. This is because the block has a finite length and one of the boundary conditions on which the Philip's equation is based, is not satisfied. The value of "desorptivity" was roughly S_E = 0.011cm/min$^{1/2}$. This is 85% of the desorptivity for the drying exp#1. It will take roughly 1.4 times longer for the same amount of water to evaporate than the drying exp#1, although the air flow rate ratio was 1.75.

In Figure 7-6, the evaporation rate is shown as a function of the square root of time. Since $E(t)$ was not perfectly proportional to $t^{1/2}$, the evaporation rate $e(t)$ does not follow the Philip's equation, either.

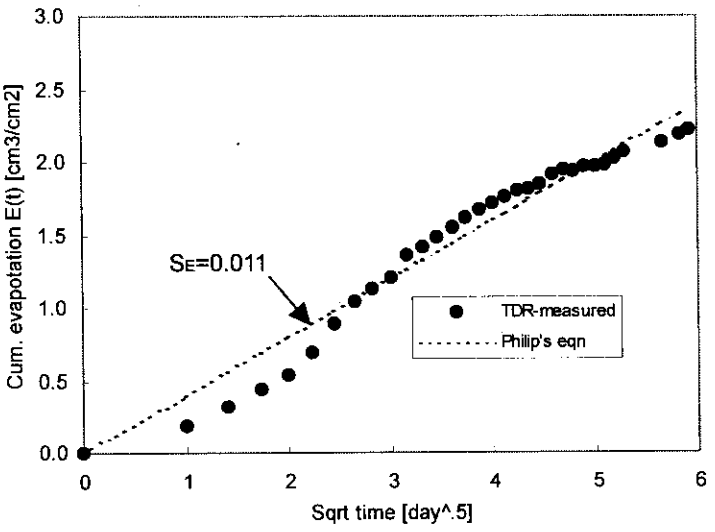

Figure 7-5. Cumulative Evaporation $E(t)$

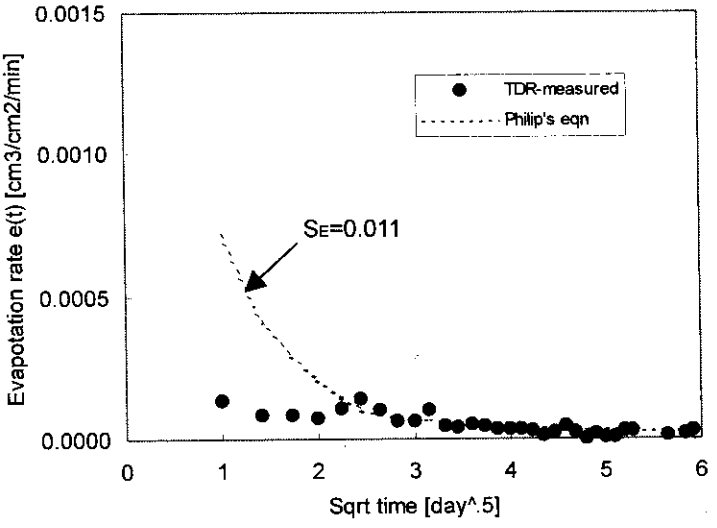

Figure 7-6. Evaporation rate $e(t)$

7.4 Summary

Unlike the wetting cycle, the cumulative evaporation did not perfectly follow the Philip's equation. This is because the width of the matrix blocks used in our experiment is not large enough, thus the effect of the boundary becomes important from the beginning. *Covey* [1963] mathematically showed that similar behavior was seen in the drying of a short soil column drying. The numerical simulations of drying presented in chapter 9 confirm this type of behavior during drying, i.e., uniform decrease in water content in short columns. The drying front migration was somewhat two-dimensional at very early times and thus the alignment of the probes were not appropriate. For future experiments, the probes should be aligned so that such two-dimensional water content distribution can be measured.

Due to a large contrast ($>10^3$) in the permeabilities of the fracture and the matrix, it had been expected that the air going into the fracture would not flow into the matrix. Nonetheless, it is possible that some air was flowing through the matrix in the vicinity of the fracture, especially near the top entrance. This advective air flow in matrix possibly caused some evaporation inside the matrix and exited from the surface on which the TDR probes were attached. For the future experiments, complete sealing of the block surface is recommended. Of course, this should be done without affecting the TDR probes (perhaps by not using the sealant in a region surrounding the probe locations).

In addition, unlike in the wetting cycle with a sufficient water inflow rate, the vapor density of the dry air in the fracture increases as it removes vapor from the matrix. This results in a decrease in evaporation rate along the fracture. The change in vapor density might also cause buoyant forces to be mobilized, because moist air has a lower bulk density than dry air. For a more detailed understanding of the drying behavior of fractured rock masses due to dry air flow through the fractures, some of these additional influences may need to be considered.

8. Fracture-network Wetting Experiment

8.1 Experimental Apparatus and Measuring Method

Following the single-fracture system, a fracture-network system is considered. A schematic view of the apparatus is presented in Figure 8-1. The network is relatively simple but complex enough to investigate the water migration behavior. A total of 15 square Indiana limestone tiles with dimensions of 13(W) x 13(H) x 2.1(D)cm and four rectangular tiles with 6.5(W) x 13(H) x 2.1(D)cm were assembled to form a network of fractures as shown in Figure 8-1. The tiles were cut using a diamond saw. The effective porosity was approximately n=12-13% but the tiles were not as homogeneous as the blocks used in the previous sections. A preliminary static imbibition test, using six similar tiles, showed that the value of sorptivity for the tiles was in the range of 0.0015-0.0032cm/min$^{1/2}$, which was roughly ten times smaller than the sorptivity value of the blocks (Figure 8-2).

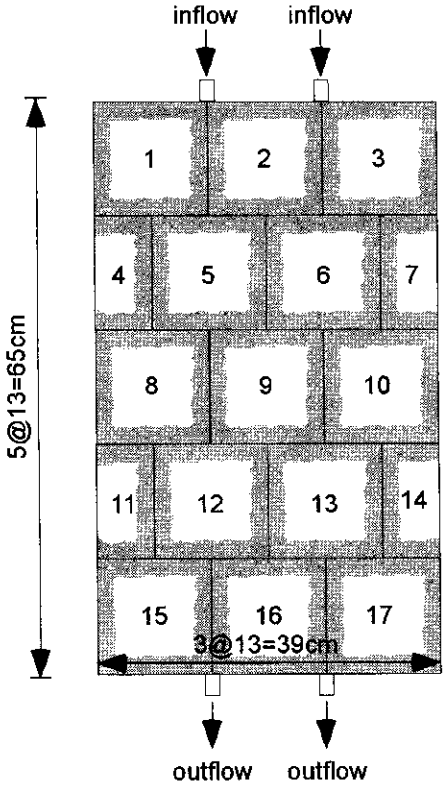

Figure 8-1. Fracture-network experiment apparatus

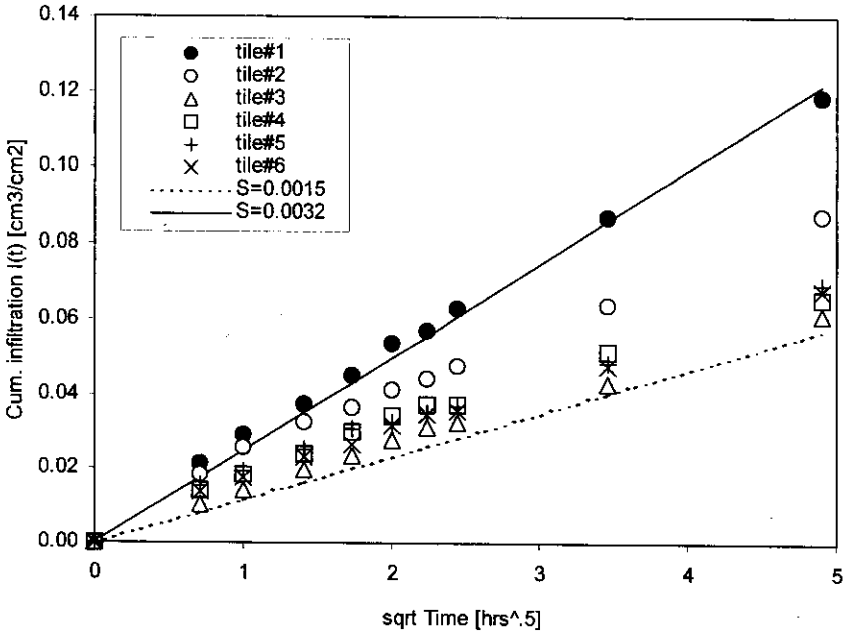

Figure 8-2. Static imbibition test for Indiana limestone tiles

The tiles were air-dried at room temperature ($24 \pm 1°C$) for more than a week in the laboratory where the relative humidity was approximately 10-15%. A spacer string with a diameter of 0.2mm was used to ensure a uniform and known aperture. Although the tiles were cut very carefully, it was found that the resulting apertures were not perfectly uniform. Slight differences in the size of the tiles caused a variation in apertures. Thus, 0.2mm should be considered as the minimum aperture. The edges of the fractures were sealed using a silicone sealant so that water would not leak directly from the fractures. During the experiments, the tiles were completely covered by acrylic plates to avoid evaporation from the surfaces.

At the top end of the fracture, two inlets were attached and water was provided at a constant rate. The two outlets at the bottom were exposed to the atmospheric pressure. In the experiment, the inflow and outflow rates were measured for 7 days. The wetting experiment was done with a constant water flow rate and the infiltration from the fracture to the matrix was investigated. The water flow rate was set to $2.3cm^3/min$

(1.15cm^3/min per inlet). At selected times, photographs of the surface were taken as well. All the outer boundaries were closed to flow thus water could flow only through fractures between the tiles.

As mentioned above the tiles were not as homogeneous as the blocks used in the previous sections. A series of wetting tests were conducted to check if any leaks occur on the surface of the tiles. Some leaks did occur mainly at two locations (between tile#1 and #2, between #6 and #10). Careful observation of the tile surfaces revealed that somewhat larger pores were concentrated in these areas. These areas were sealed with silicone sealant prior to the wetting experiment.

8.2 Experimental Results and Discussion

A Series of photographs are presented in Photograph 8-1(A)-(F). Water flowed mostly in the fractures in the central area. This is perhaps because the flow in fractures is gravity-driven (although the matrix imbibition is suction-dominated), thus water tended to flow in vertical fractures rather than in the horizontal ones. At early times only the left outlet was discharging, despite inflow from two inlets, one of which was closer to the right outlet. The right outlet started to discharge at t=30hours, an increased wetted zone in the vicinity of the outlet is visibly evident in the photograph at around this time. At t=132hours, the leaks at two locations (between tile#1 and #2, between #6 and #10) increased and the experiment was terminated at t=168hours.

The mean migration of the wetting fronts was roughly perpendicular to the fracture. Despite the silicone sealing of the leaking areas, slight leaks still occurred. The leaked water occasionally dripped along the tile surface and made surface of tiles wet (especially on tiles #5 and #10) and apparently evaporated, leaving a precipitate behind.

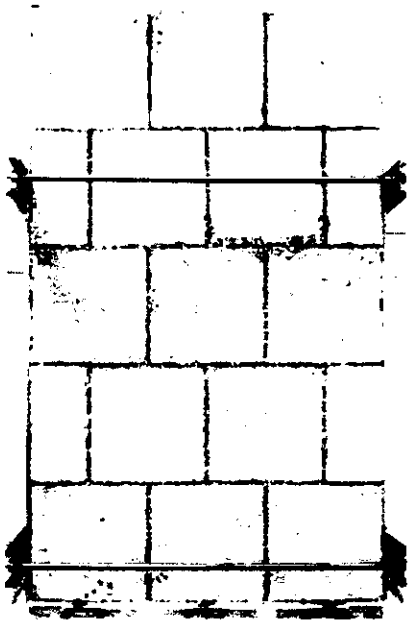

(a) t=0hours

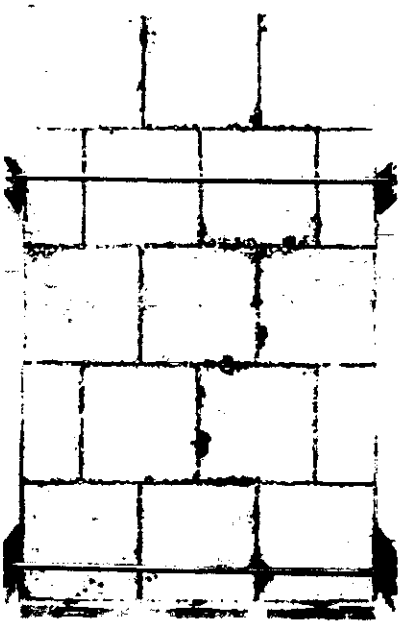

(b) t=0.5hours

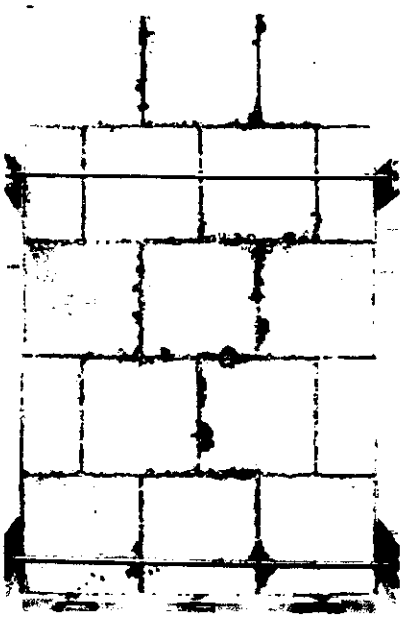

(c) t=1hour

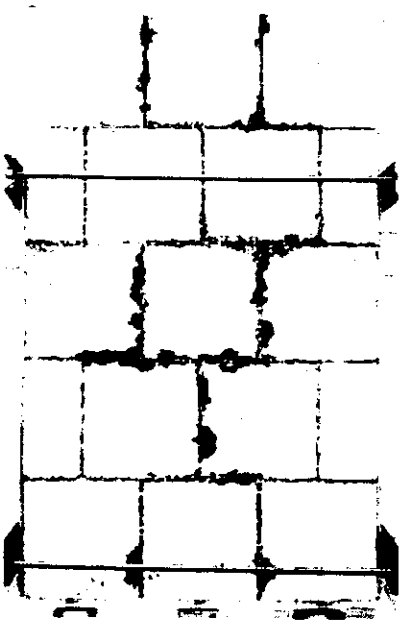

(d) t=2hours

Photo 8-1(A). Wetting front migration at selected times (Network exp)

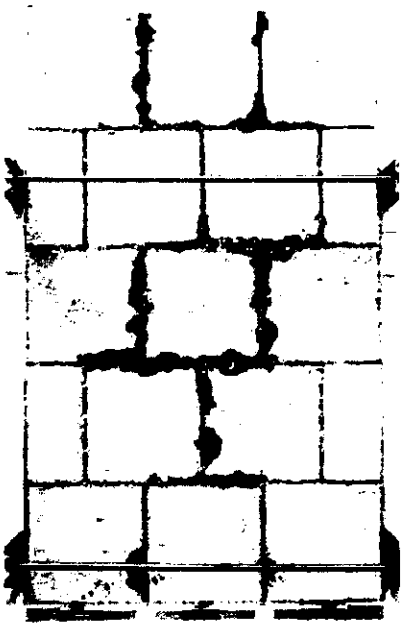

(e) t=3hours

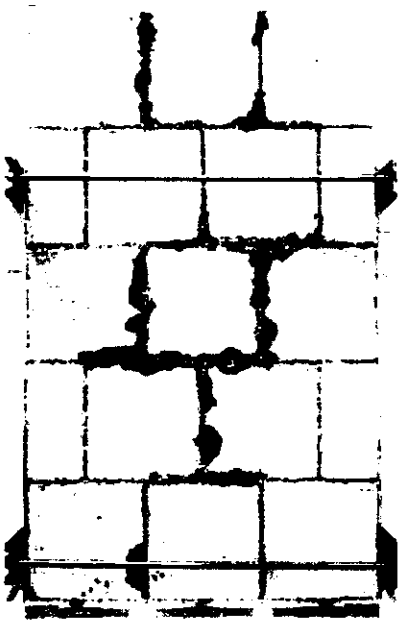

(f) t=4hours

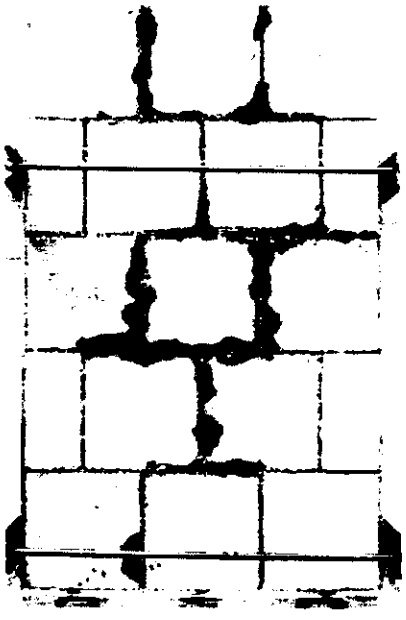

(g) t=6hours

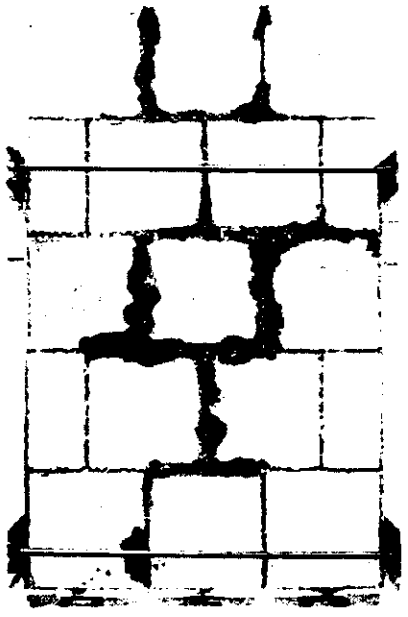

(h) t=9hours

Photo 8-1(B). Wetting front migration at selected times (Network exp)

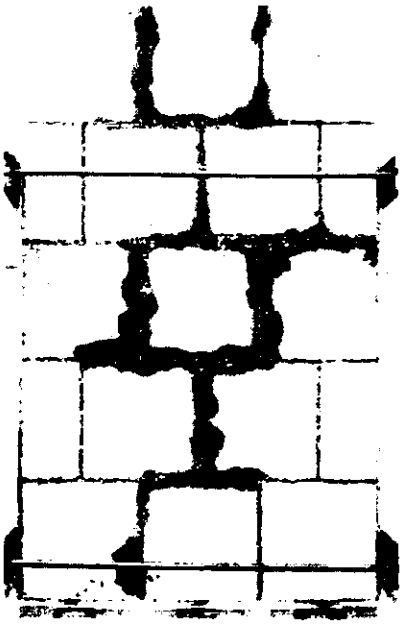

(i) t=12hours

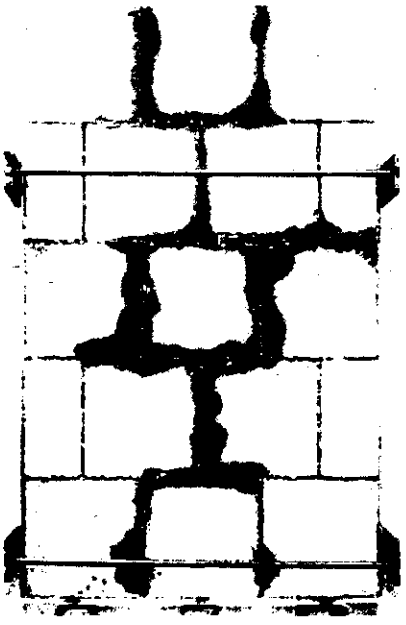

(j) t=18hours

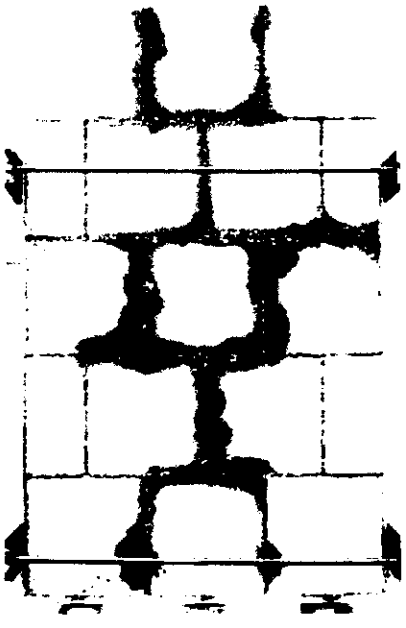

(k) t=24hours

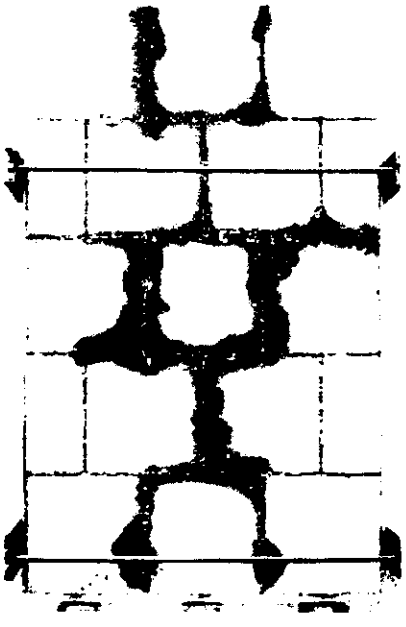

(l) t=30hours

Photo 8-1(C). Wetting front migration at selected times (Network exp)

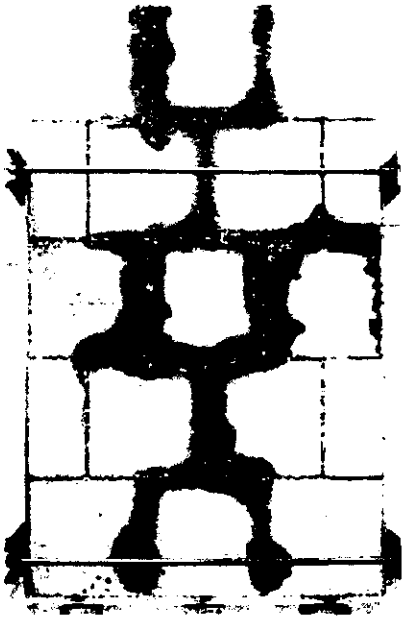

(m) t=36hours

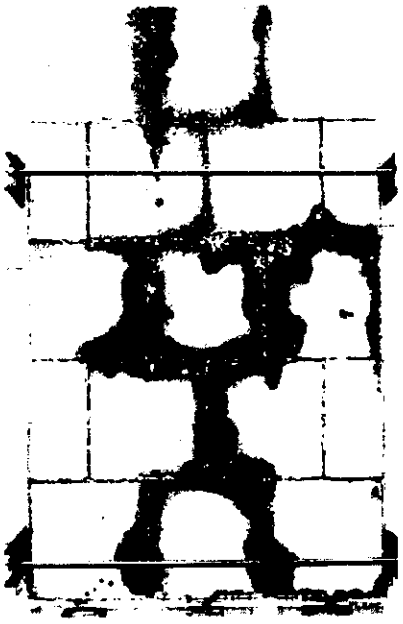

(n) t=48hours

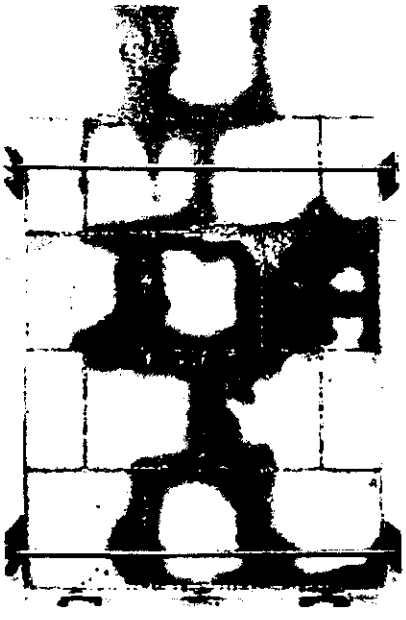

(o) t=60hours

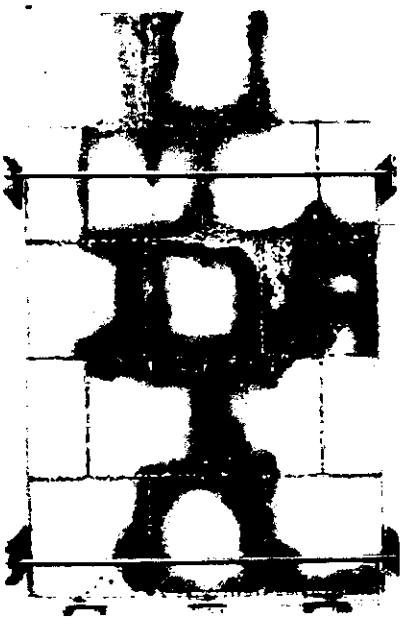

(p) t=72hours

Photo 8-1(D). Wetting front migration at selected times (Network exp)

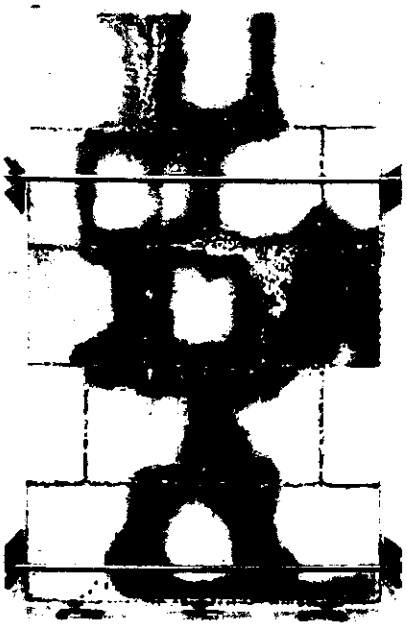

(q) t=84hours

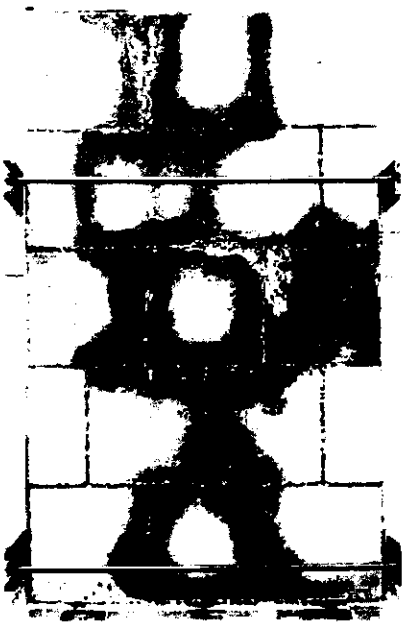

(r) t=96hours

(s) t=108hours

(t) t=120hours

Photo 8-1(E). Wetting front migration at selected times (Network exp)

(u) t=132hours

Photo 8-1(F). Wetting front migration at selected times (Network exp)

The cumulative infiltration $I(t)$ vs. $time^{1/2}$ in Figure 8-3 shows that $I(t)$ - $t^{1/2}$ relationship follows a piecewise linear relationship with two distinct slope changes. The first increase in the slope corresponds to when the right outlet started to discharge at t=30hours (thus, $t^{1/2}$=5.5hour$^{1/2}$). It is possible that at this moment, the flow pattern in the fracture network changed (water flows through more fractures) thus the infiltration rate increased. At t=132hours (thus, $t^{1/2}$=11.5hour$^{1/2}$), the second increase in the slope occurred. This corresponds to the increase in the leakages at the two locations mentioned above. At t=132hours, the penetration of the wetting fronts were roughly half way to the center of the tiles.

The macroscopic imbibition from a fracture to matrix did not follow Philip's equation, however, two straight-line portions were identifiable, with the break in slope corresponding to t=30hours, when the right outlet started discharging. In this particular

case, the values of the effective sorptivity (defined for the entire fractured rock mass, that is the cumulative infiltrated water divided by the sum of all the fracture areas although some of the fractures were not transmitting water) were found to be S=0.0018cm/min$^{1/2}$ for t<30hours and 0.004cm/min$^{1/2}$ for 30<t<132hours. This is obviously less than 0.032cm/min$^{1/2}$ obtained from the sorptivity experiment but is consistent with the static imbibition test results mentioned in section 8.1 (Figure 8-2). It is because of the difference in materials between the tiles and the block. Figure 8-4 shows the time trend of the infiltration rate $i(t)$ with time (calculated with S=0.0018cm/min$^{1/2}$), which is simply the time derivative of $I(t)$. The infiltration rate roughly to follow the Philip's equation up to t=30hours (thus, $t^{1/2}$=5.5hour$^{1/2}$). For t>30hours, the infiltration rate is slightly larger than calculated values because, in fact, S=0.004cm/min$^{1/2}$ should have been used after t=30hours.

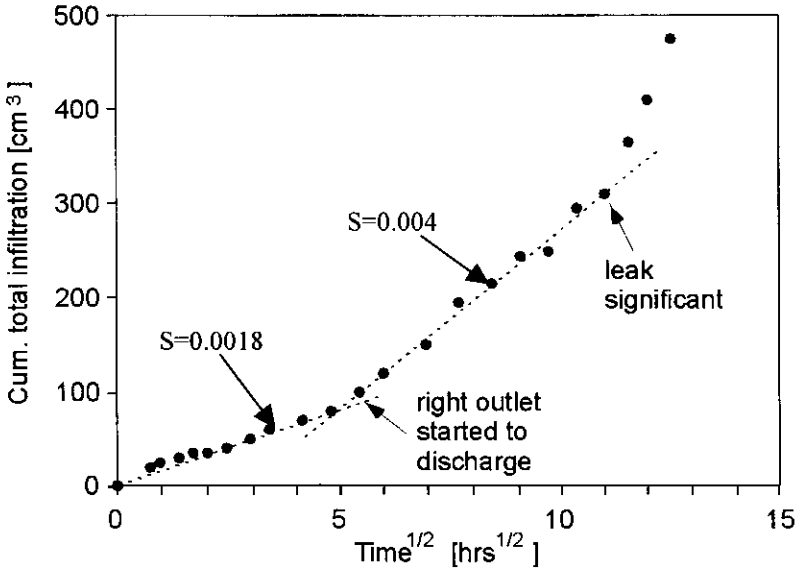

Figure 8-3. Cumulative infiltration $I(t)$

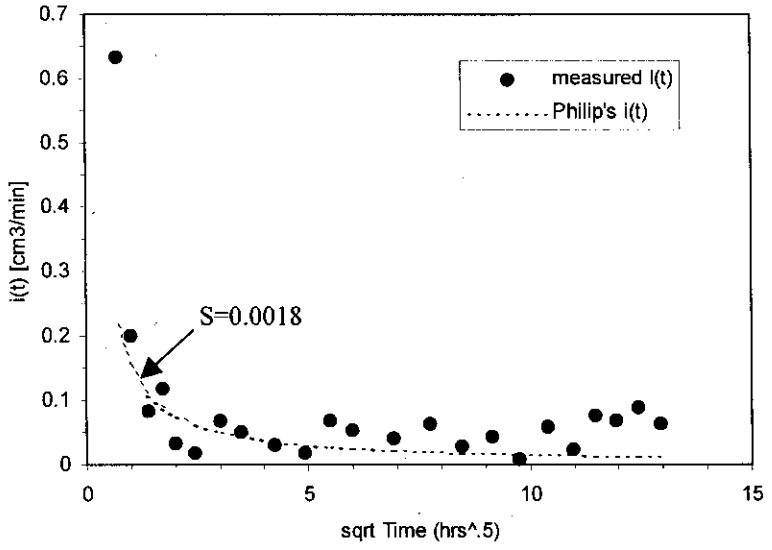

Figure 8-4. Infiltration rate *i(t)*

Figure 8-5 shows the time trend of the cumulative inflow and outflows. At t=30hours, the right outlet started to discharge. As mentioned above, the flow pattern changed at this moment. At t=132hours when the leakage increased, the right outlet stopped discharging. In a partially saturated fracture network, it was found that the flow pattern could change in time. This observation is consistent with those of other researchers [*Glass et al.,* 2002].

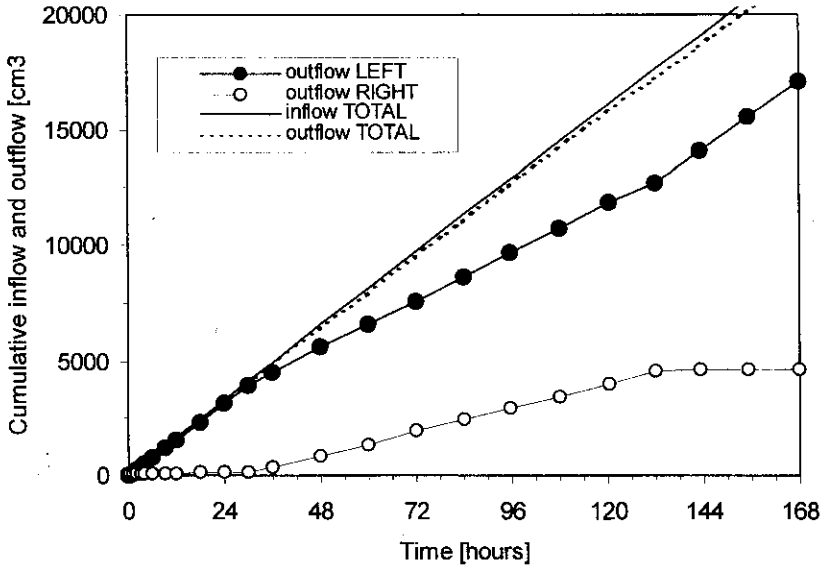

Figure 8-5. Inflow and outflows with time

Figure 8-6 shows the time trend of the ratio of the outflow to inflow. At the beginning, since the matrix was dry and its suction was very large, a large portion of water (e.g., 28% at t=0.5hours) flowing through the fracture network was absorbed by the matrix. After 2hours, roughly 96% of water was coming out of the system, showing that most of the water was just passing through the system without being absorbed by the matrix. Just like the single-fracture system, the fracture-matrix system works as a damper such that a sharp excitation such as an intermittent precipitation event decays and the damping effect becomes smaller as the event gets more continuous.

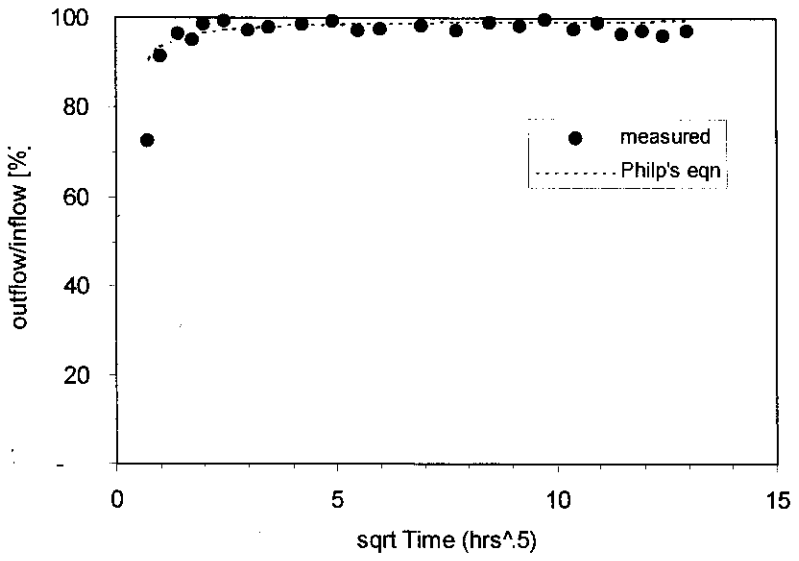

Figure 8-6. Outflow/Inflow rate

8.3 Summary

In this chapter we described a wetting experiment carried out in a fracture network. Water was allowed to flow into the fracture network through two inlets, and flow out through two symmetrically placed outlets. At early times (t < 30 hours), only one of the outlets (the left one) was flowing. At t=30hours, the right outlet started to discharge and the flow pattern changed noticeably. At t=132hours, the leakages increased and the flow pattern changed again. The cumulative infiltration into the fracture network exhibited a piecewise linear variation with time$^{1/2}$, with different slopes (i.e. different effective sorptivities), during the time ranges $0<t<30$hours and $30<t<132$hours. The break in slope is clearly associated with the activation of the second outlet, and is plausibly due to an increase in actual area across which absorption occurs. This experiment confirms that flow pathways can change and discrete changes in behavior can occur in partially saturated fractured networks, as also seen by Glass et al. [2002].

Roughly speaking, until the wetting fronts are at half way to the center of the tiles, the Philip's equation allowed us to quantitatively relate the cumulative infiltration $I(t)$ to $t^{1/2}$ by a parameter 'sorptivity'. The values of the macroscopic sorptivity of the network system were roughly ten times smaller than the ones obtained for the uniform blocks, but were consistent with the results from the static imbibition test using similar tiles (Figure 8-2). It can be concluded that the overall qualitative behavior of the network was similar to that of the single-fracture system at least until the wetting fronts are at the midpoint of the tiles. For future experiments, it is recommended that a surface sealing method be developed and the infiltration behavior after the wetting front passes the midpoint of the tiles be investigated.

9. Numerical Simulations

In the previous chapters, we presented the results of several experiments that included various degrees of complexity, from single fractures to fracture network. The results confirmed the insignificance of gravity-driven flow in the rock matrix and suggested that the non-linear diffusion equation approach was applicable to model the water migration in fractured rock masses. Although the development of a numerical model that contains detailed representations of water exchange between the fracture and matrix is beyond the scope of this research, selected experiments were numerically simulated as a preliminary validation of the non-linear diffusion equation approach. We used a simple one-dimensional numerical simulator that is based on the finite difference method, and a commercial finite-element code ABAQUS. In this chapter, the numerical results are presented and discussed.

In the 1D finite difference method, the non-linear diffusivity equation is discretized as follows. Recall the non-linear diffusion equation;

$$\frac{\partial \theta}{\partial t} = \frac{\partial}{\partial x}\left(D(\theta)\frac{\partial \theta}{\partial x} \right) \tag{9.1}$$

where θ=water content, $D(\theta)$=hydraulic diffusivity.

Eq. (9.1) is discretized as;

$$\frac{\theta_i^{n+1} - \theta_i^n}{\Delta t} = \frac{1}{\Delta x}\left[D\left(\theta_{i+1/2}^{n+1/2}\right)\frac{\theta_{i+1}^{n+1} - \theta_i^{n+1}}{\Delta x} - D\left(\theta_{i-1/2}^{n+1/2}\right)\frac{\theta_i^{n+1} - \theta_{i-1}^{n+1}}{\Delta x} \right] \tag{9.2}$$

where, subscripts *i-1, i, i+1* denote the discrete points in space, superscripts n and n+1 denote the time steps.

Rewriting eq. (9.2) yields,

$$\theta_i^n = -\frac{\Delta t}{\Delta x^2}\left[D\left(\theta_{i-1/2}^{n+1/2}\right)\theta_{i-1}^{n+1} - \left(D\left(\theta_{i-1/2}^{n+1/2}\right) + D\left(\theta_{i+1/2}^{n+1/2}\right) + \frac{\Delta x^2}{\Delta t}\right)\theta_i^{n+1} + D\left(\theta_{i+1/2}^{n+1/2}\right)\theta_{i+1}^{n+1}\right] \tag{9.3}$$

Eq (9.3) shows a nonlinear tri-diagonal system of equations. It was solved using a Newton-Raphson iterative scheme, employing the Thomas algorithm within each iteration.

9.1 1-D Simulation of the Diffusivity Experiment

The diffusivity measurement experiment was numerically simulated first. The 24cm-long block is discretized into 24 elements as illustrated below (Figure 9-1).

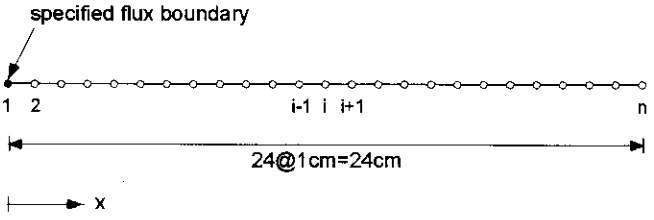

Figure 9-1. One-dimensional model discretization and conditions

As the initial condition, θ=0.001 was used. At the water-supply boundary (x=0), the flux $q(t)$ was specified according to the obtained sorptivity. As shown in Figure 9-2, for early times (t<6hours), the sorptivity was slightly less than 0.032cm/min$^{1/2}$. It was found that the value of sorptivity for 0<t<6hours was 0.026cm/min$^{1/2}$. Based on these numbers, the flux at the boundary was calculated by $q(t) = i(t) = \frac{1}{2}\frac{S}{\sqrt{t}}$. At this moment, it was important to investigate how accurately the non-linear diffusion equation model can predict the water infiltration into the rock block. Thus, the diffusivity functions and the

sorptivity values for the boundary condition were chosen so that they represent the measured data as accurate as possible.

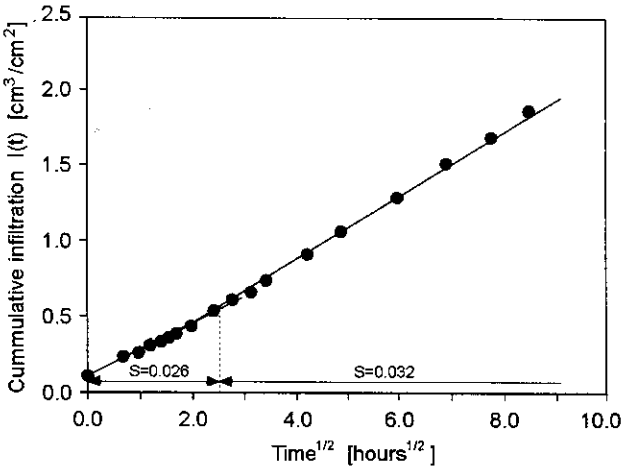

Figure 9-2. Determination of flux at the boundary

For the hydraulic diffusivity, based on the results presented in chapter 4, four exponential functions were used to describe the measured data (Figure 9-3). The coefficients of the functions are also given in the figure.

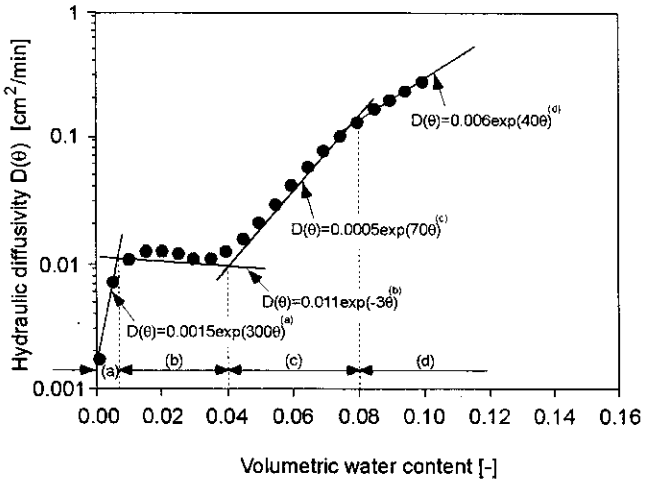

Figure 9-3. Hydraulic diffusivity used for simulation

Figures 9-4(a), (b) show the numerical simulation results. The water content distribution within the block at various times, and thus the wetting front migration, is predicted well in the numerical simulation. With the appropriate boundary conditions and hydraulic diffusivity, the non-linear diffusion approach yields reasonable predictions for the water infiltration into the rock matrix.

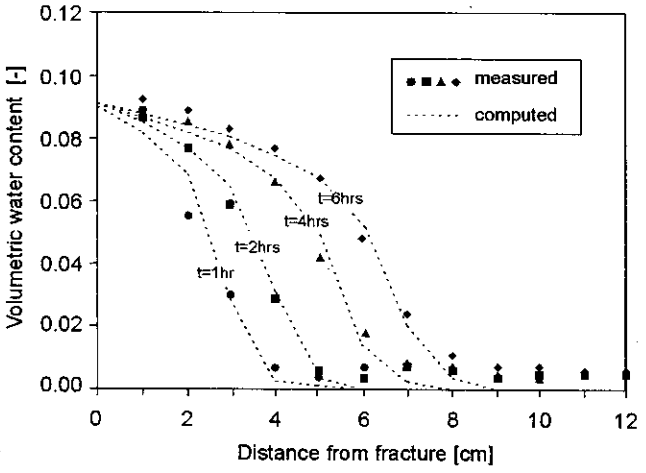

Figure 9-4(a). Water content distribution (t<6hours)

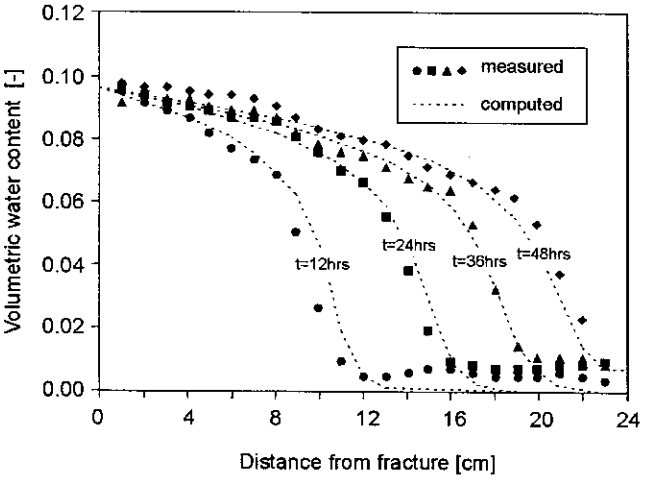

Figure 9-4(b). Water content distribution (12<t<48hours)

It should be noted that although the inflow flux at x=0 was specified, the resulting water content at the boundary is almost unchanged (0.092<θ<0.095).

9.2 1-D Simulation of the Single-Fracture Experiment (Wetting)

In this section, the 1-D simulation results of the single-fracture wetting experiment are presented and discussed. The 16.8cm-long block was discretized into 16 elements as illustrated in Figure 9-5. Since the wetting front migrated in the horizontal direction, it was assumed that the infiltration behavior from the fracture was one-dimensional.

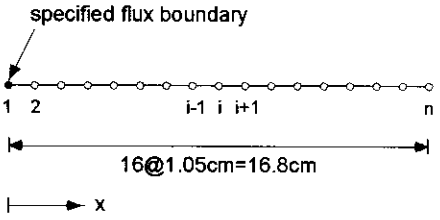

Figure 9-5. One-dimensional model discretization and conditions

As the initial condition, θ=0.002 was used. At the fracture-matrix interface (x=0), the flux $q(t)$ was specified according to the Philip's equation $q(t) = i(t) = \frac{1}{2}\frac{S}{\sqrt{t}}$ with S=0.026cm/min$^{1/2}$. For the hydraulic diffusivity, the four exponential functions described in the previous section were used.

Figure 9-6 shows the water content distribution in the right block at selected times. The fracture-matrix interface is at x=0. In the numerical simulation, the water content at x=0 is almost unchanged although the inflow flux was specified. However, the water content at x=0 from the experiment shows a monotonic increase with time. The discrepancy between the measured and computed water content distribution is large for early times. The possible reasons for this discrepancy are discussed below.

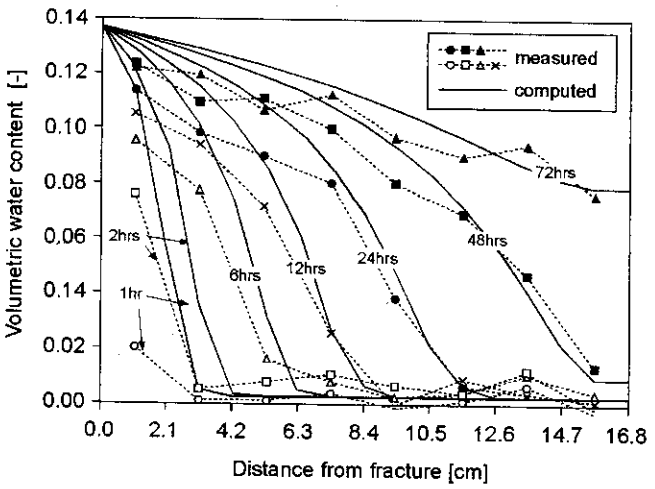

Figure 9-6. Water content distribution

(1) There was no probe on the fracture-matrix interface. The closest probe is at x=1.05cm, which measures the averaged water content for $0<x<2.1$cm. Lack of data at x=0 suggests that the measurements were not properly representing the water content distribution near the fracture. Increasing the number of probes may improve the results.

(2) The fracture might have been partially saturated. That is, channeling or fingering might have occurred. Under such conditions, water is absorbed from a part of the fracture-matrix interface. The absorbing area may have increased with time, resulting in a possible increase of water content near the fracture. In the numerical simulation, the channeling and fingering were not considered.

(3) In the $I(t)$-$t^{1/2}$ relationship in Figure 6-3, it can be seen that the slope (=sorptivity) is smaller at early times. Using a smaller sorptivity at early times may improve the results.

9.3 1-D Simulation of the Single-Fracture Experiment (Drying)

In this section, the 1-D simulation results of the single-fracture drying experiment are presented and discussed. The 1-D finite-difference model is identical to the one used for the wetting case. As shown in chapter 8, the experimental data showed two-dimensional drying. The drying rate near the dry-air inlet was faster, resulting in a V-shaped drying front. However, in this research, only the preliminary level of validation of the non-linear diffusion equation approach is done, and the modeling of such a multi-dimensional drying phenomena is beyond the scope of this research. Therefore, a one-dimensional model was used to simulate the single-fracture drying cycle.

As the initial condition, θ=0.002 was used. At the fracture-matrix interface (x=0), the evaporation flux q_e was specified according to the Philip's equation $q(t) = e(t) = \frac{1}{2}\frac{S_E}{\sqrt{t}}$ with S_E=0.013cm/min$^{1/2}$ (thus exp#1 was simulated). For the hydraulic diffusivity, the four exponential functions from the previous section were used.

Figure 9-7 shows the water content distribution in the right block at selected times. The fracture-matrix interface was at x=0. The numerical simulation captured the trend in the water content distribution but tended to overestimate the actual values. The discrepancy between the simulated results and the actual water contents became larger with time. The possible reasons for this discrepancy are discussed below.

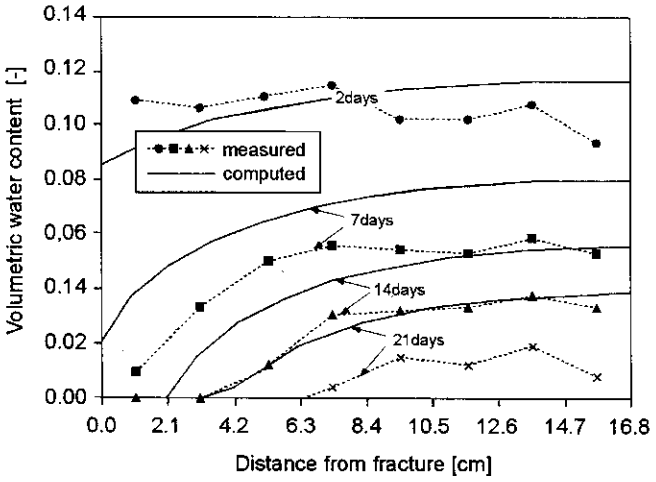

Figure 9-7. Water content distribution

(1) When specifying the evaporation rate at the boundary (x=0), the desorptivity was used but as can been seen in Figure 7-3, unlike the wetting cycle, desorptivity does not explain the measured data perfectly. Specifying the evaporation rate more precisely may improve the results.

(2) Using a one-dimensional model for the two-dimensional drying of the matrix exceeded the model's capacity. Using two-dimensional model may be an alternative.

(3) The alignment of the TDR probes, that were installed to measure the one-dimensional wetting/drying front migrations, was not sufficient to describe the water content distribution, from which the evaporation rate was calculated, in the block properly. If a two-dimensional model is developed in the future, it is recommended that the water content in the block should be measured such a way that the two-dimensional distribution is obtained.

(4) In the one-dimensional model, it is automatically assumed that the evaporation rate is constant along the entire length of the fracture. In reality, dry air enters the fracture, removes some water from the matrix, flows further down still removing water if not vapor-saturated. Thus, the vapor saturation of the air increases along

the fracture. That is, the evaporation rate actually decreases along the fracture. This should also be included in the future modeling.

(5) The hydraulic diffusivity used for the drying cycle was measured from a wetting experiment. For dry soils, it was reported that the hydraulic diffusivity was hysteretic, that is, the diffusivity is different for drying. The diffusivity measurement from the drying cycle should be done and such property should be used to investigate this further.

9.4 2-D simulation of the Infiltration into a Tile

In the fracture-network experiment, some leakages occurred when the wetting fronts were halfway to the center of the tiles. Due to the leaks, the infiltration rate kept increasing whereas it was supposed to decrease. In this section, using a commercial finite-element code ABAQUS, the water infiltration behavior into a square tile was investigated. The non-linear diffusion equation was solved with the material property shown in section 9.1. The schematic model is shown in Figure 9-8. For the 2-D model, a 1/4 of the 13x13cm tile was discretized into 0.5x0.5cm square elements. At the water-supply boundary, water content was fixed to 0.09 (=approximately 65% of the porosity 14%). For comparison, a 1-D model was also used with the same length of water-supply boundary.

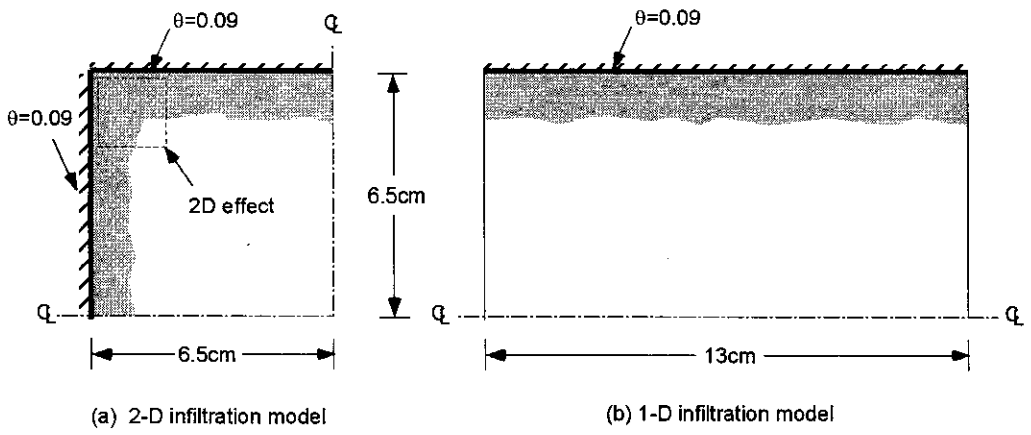

Figure 9-8. 2-D and 1-D models of a square tile

Figure 9-9 shows the cumulative infiltration into the square tile. For comparison, the results for 1-D infiltration is also presented. The 2-D infiltration shows quite the same infiltration until t=1hour in this particular case. After that, it starts to deviate from the line for the 1-D case. However, until roughly t=2hours (thus $t^{1/2}$=1.4 $hrs^{1/2}$), the infiltration is almost linearly related to the square root of time although the constant of proportionality is slightly smaller.

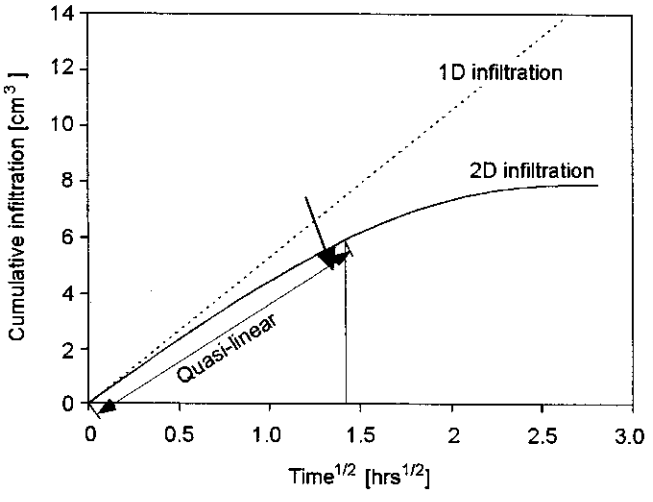

Fiugre 9-9. Cumulative infiltration in 1-D and 2-D

Figure 9-10 shows the water content profiles within the tile at selected times. It was mentioned above that until roughly t=2hours, the cumulative infiltration was linearly proportional to the square root of time, that means that the 2-D infiltration behavior can still be described using the sorptivity. As can be seen in Figure 9-10, at t=2hours the wetting front is half way to the center of the tile (x=6.5cm). Therefore, roughly speaking, the cumulative infiltration into fractured rock masses follows the Philip's equation until the wetting front reaches half way to the center of the mean size of the matrix (in this case, the tiles). It is also expected that the macroscopic sorptivity will be smaller than the 1-D sorptivity. After this point, the infiltration rate will decrease with time. In the experiment, the decrease would have been observed if the significant leaks did not occur.

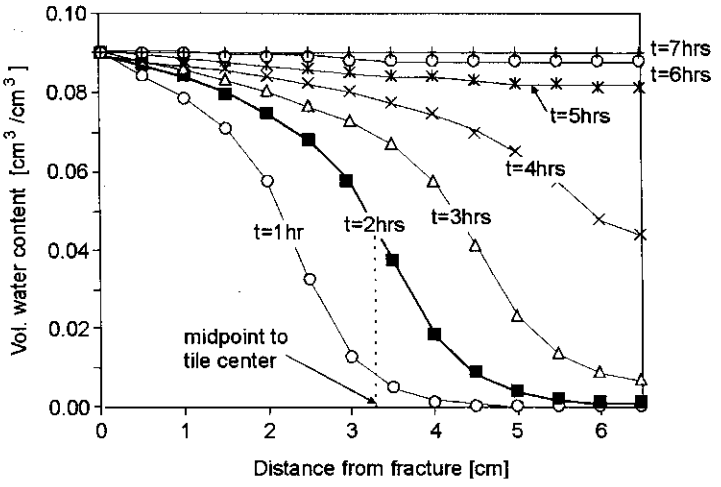

Fiugre 9-10. Water content distribution in tile at selected times

9.5 Summary

In this chapter, only the first level of validation of the non-linear diffusion equation approach was conducted using 1-D and 2-D models. The simulation of the diffusivity measurement experiment agreed well with the measured data when solved

with proper material property and boundary conditions.

For the single-fracture wetting cycle, there was a little disagreement between the measured and computed water content values near the fracture at early times. To better understand or eliminate this discrepancy, we need to install more probes, or use more detailed infiltration rate measurements at the boundary. In case of the single-fracture drying cycle, the drying occurred in two-dimension although the measured data was based on the one-dimensional assumption. The desorptivity concept did not perfectly represent the evaporation rate. The material property is known to be hysteretic and the diffusivity function for the wetting cycle was used to simulate the drying phenomenon. These are the main reasons for why the numerical simulation did not predict the water content distribution in the block well. For the drying of the matrix due to air flow in the fracture, the above issues must be examined more carefully.

The 2-D simulation of the water infiltration into a square tile, and thus into fractured rock masses, showed that the cumulative infiltration would follow the Philip's equation until the wetting front reaches halfway to the center of the mean size of the matrix block. This is of great importance when predicting the infiltration behavior into fractured rock masses.

10. Biofilom Formation and Hydrophobicity

10.1 Outline of Biofilim Formtion Experiment

There has been a growing realization that hydrophobic interactions play a role in many microbial processes in association with adhesion and biofilming phenomena, including microbial adhesion to tissues of plants and animals, implants and prostheses, contact lenses, glass, oil, steel, teeth, and rocks. Despite numerous literatures on this subject, the structural basis of microbial hydrophobicity has been little discussed in relevance to biofilm formation and microbial cellular morphogenesis [*Rosenberg and Doyle*, 1990]. As microbial growth on rock surfaces are considered to interact with fluid flow and material transport [*Fletcher and Murphy*, 2001], formation of biofilm having different hydrophobic features should be a focus of the fluid flow studies.

During this study, we have obtained several pure cultures of microorganisms showing various features of cell surface hydrophobicity (ex. Fig. 10-3). An unidentified bacterial species of the genus *Halomonas* showed a very low hydrophobicity, *i.e.* high hydrophilicity, and was used for experimental biofilm formation on crack surface of "Kimachi sandstone" from Kimachi, Shimane Prefecture, Japan. The crack surface was regarded as the simulation of rock fractures that are discussed in other chapters of this study.

Observation by electron scanning microscopy (SEM) revealed that the *Halomonas* cells attach and grown on surfaces of sandstone mineral grains. Aggregates, or microcolonies, of the attached cells on microcracks (grain boundary cracks) were also observed, which corresponds to the initial process of biofilm formation. Biofilm were also formed on wider areas of microcracks. The biofilm consisted of loosely interconnected

cells, and showed non-sheet-like form against the expectation of sheet-like or film-like structure. It was thus difficult to determine the hydrophobicity of "film-like" biofilms by conventional method such as the measurement of contact angle. Technical developments are further needed to establish the practical approaches to: 1) measurement of attached cell surface hydrophobicity (free-living cell surface hydrophobicity is easily measurable), and 2) formation of real "film-like" biofilms of various hydrophobic features on various rock surfaces.

10.2 Biofilm Hydrophobicity Relevant to Fluid Flow and Transport

Both the degree of water saturation and the velocity of the water influence bacterial transport and biofilm formation. Importance of water saturation can be seen in the unsaturated zone where retention of water in the pore spaces controls the transport of water. As the water content of unsaturated zones decreases, water is contained in increasingly smaller capillary spaces between the sediment grains. Accordingly, as the thickness of the water film decreases, inhibition of biofilm formation on fracture surface becomes significant. Reducing the distance between the bacteria and the fracture surface increases the probability that the bacteria will contact with the surface and form biofilm thereon. Studies have shown that cell surface hydrophobicity is a major factor controlling the amount of bacterial retention in unsaturated zones [*Fletcher and Murphy*, 2001]. These cell properties result in removal by straining and adhesion mechanisms (Fig. 10-1). Also, in partially saturated systems, the surface area of gas-water interfaces increases and the dynamics of the air-water interface can clearly influence bacterial distribution. It is presumed that bacteria having high hydrophobicity preferentially sorb to gas-water interfaces over silica surfaces.

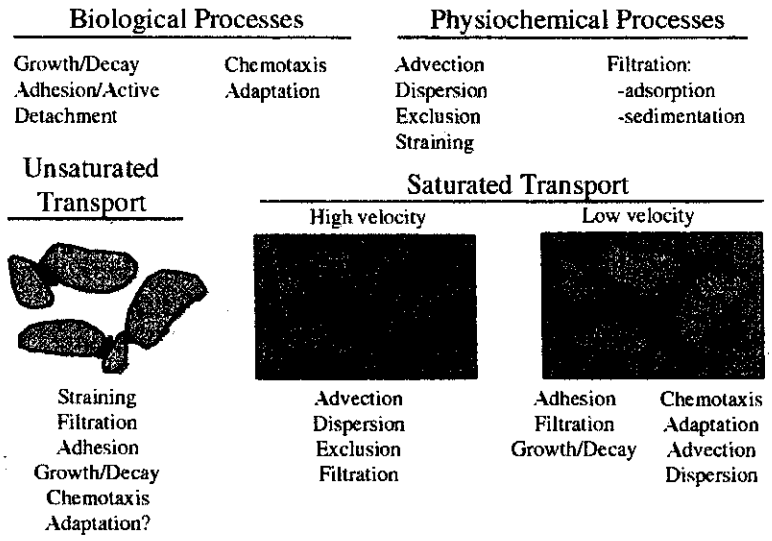

Fig. 10-1. Biological and physicochemical processes involved in bacterial transport and the potential importance of these processes under unsaturated and saturated flow conditions [cited from *Fletcher and Murphy*, 2001].

Because the time scales are usually short for laboratory and field experiments, bacterial transport and biofilm formation are often studied for relatively rapid processes such as the preferential flow [*Fletcher and Murphy*, 2001]. Preferential flow occurs where large pores or fractures in the porous matrix become saturated with water; usually from an intense rainfall event. When saturated, these pore/fracture structures preferentially conduct the water in a vertical soil column. Microorganisms undergoing rapid transport from preferential flow to depths in the vadose zone would encounter difficulties in competing effectively with an established community, as well as adapting cell surface hydrophobicity to a new condition. Therefore, the types and degrees of interactions among fluid flow, biofilm formation and bacterial/material transport may be shaped in different ways depending on the tempo-spatial scales of a study (Fig. 10-2).

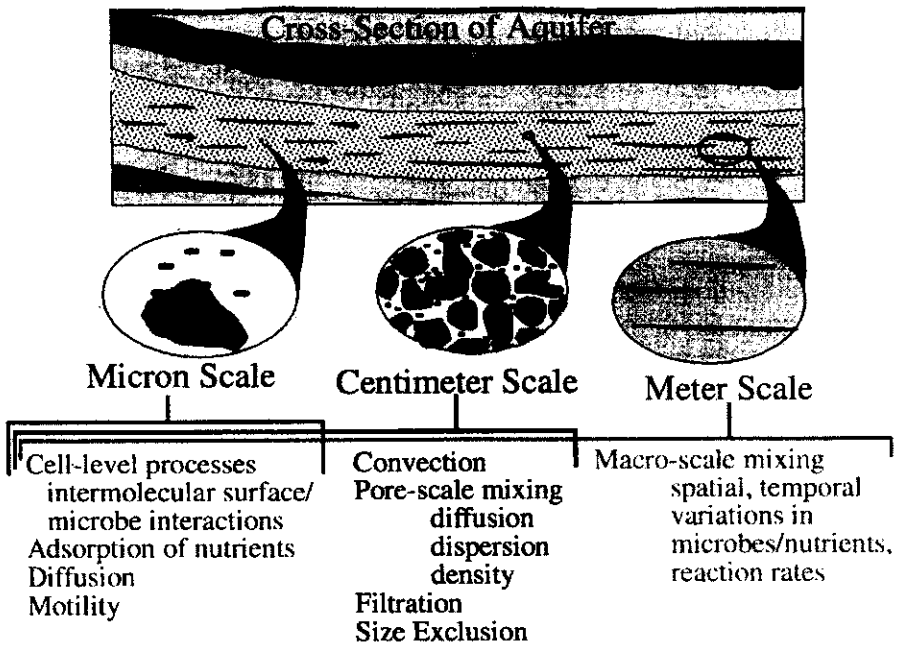

Fig. 10-2. Different scales of biofilm-related processes [cited from *Fletcher and Murphy*, 2001].

Certain species of bacteria have the ability to vary or retain their cell surface hydrophobicity according to surrounding conditions. For example, the common bacterium *Escherichia coli* exhibits a wide range of cell surface hydrophobicity according to the growth condition such as salinity, while the euryhaline halophilic bacterium *Halomonas* sp. shows relatively constant hydrophobicity over a salinity range (Fig. 10-3). Therefore, types of biofilm-forming bacteria may greatly influence the hydrophobic property of the rock fracture surface. That is, at the salinity of 7% NaCl in Fig. 10-3, whether the biofilm in question is formed by *E. coli* or *Halomonas* sp. will strongly influence the fracture surface hydrophobicity, and thus the properties of fluid flow and transport along the fracture will be affected accordingly.

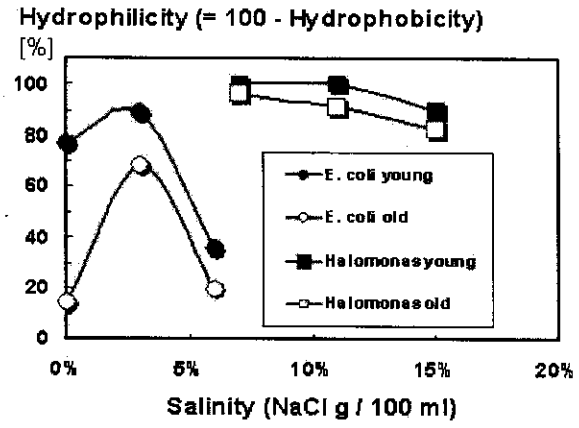

Fig. 10-3. Cell surface hydrophobicity of different microbial species at different growth salinities.

10.3 Biofilm Formation on Rock Surface

Several pure cultures of microorganisms showing various features of cell surface hydrophobicity were obtained from various environmental samples including rocks. An unidentified bacterial species of the genus *Halomonas* showed a very low hydrophobicity, *i.e.* high hydrophilicity, and was used for experimental biofilm formation on crack surface of "Kimachi sandstone" from Kimachi, Shimane Prefecture, Japan.

Pieces of Kimachi sandstone were crashed with a hammer, and the relatively flat fragments of 5-10 mm were collected and sterilized by autoclaving for subsequent microbial culture experiment. Autoclaved sandstone fragments were immersed in a fresh microbiological medium (0.5% peptone, 0.25% yeast extract, 0.1% glucose and 4% NaOH in distilled water; pH ca. 7) at different salinities of 0.5% NaCl and 20% NaCl. This fresh medium with rock fragments was then added with portions of the pre-incubated *Halomonas* liquid culture and incubated at room temperature (ca. 20°C). After 3-7 days of incubation, the sandstone fragments were transferred to 50% EtOH to fix bacterial

cells for SEM microscopy. After 30 min of 50% EtOH immersion, the rock fragments were then transferred to an EtOH-series of 70%, 80%, 90%, 95%, 98%, 99% and 100% EtOH for 30 min each immersion, which resulted in gentle and complete dehydration of bacterial cells for SEM observation.

SEM observation revealed that the *Halomonas* cells attach and grown on surfaces of the sandstone mineral grains. No significant difference was observed between the 0.5% and 20% NaCl incubations. As the experimental bacterium, *Halomonas* sp., is known to maintain relatively a high hydrophilicity over a wide range of salinity (e.g. Fig. 10-3), the experimental salinities of 0.5% and 20% NaCl may have caused only limited difference in hydrophobic/hydrophilic features of the cells on grain surfaces.

The *Halomonas* cells on smooth flat surfaces were easily observed (Fig. 10-4), while the cells grow among micrograins were difficult to identify. Aggregates (microcolonies) of the attached cells on microcracks (grain boundary cracks) were also observed, which corresponds to the initial process of biofilm formation (Fig. 10-5). Microcolonies result from *in situ* and *de novo* proliferation of attached cells, rather than the attachment of already proliferated cell aggregates. The *in situ* and *de novo* proliferation of the *Halomonas* cells by binary fission was observed on grain surface (Fig. 10-6).

Biofilm were also formed on wider areas of microcracks. The biofilm consisted of loosely interconnected cells, with the cells serving as the initiation cores of biofilm formation and as the pit-fillers of inter-grain cavities (Fig. 10-7). Against the expectation of sheet-like or film-like structure, we have observed non-sheet-like bacterial interconnections as the "biofilm" in most sapmles. It was thus difficult to determine the hydrophobicity of "film-like" biofilms by conventional method such as the measurement

of contact angle. Technical developments are further needed to establish the practical approaches to: 1) measurement of attached cell surface hydrophobicity (free-living cell surface hydrophobicity is easily measurable), and 2) formation of real "film-like" biofilms of various hydrophobic features on various rock surfaces.

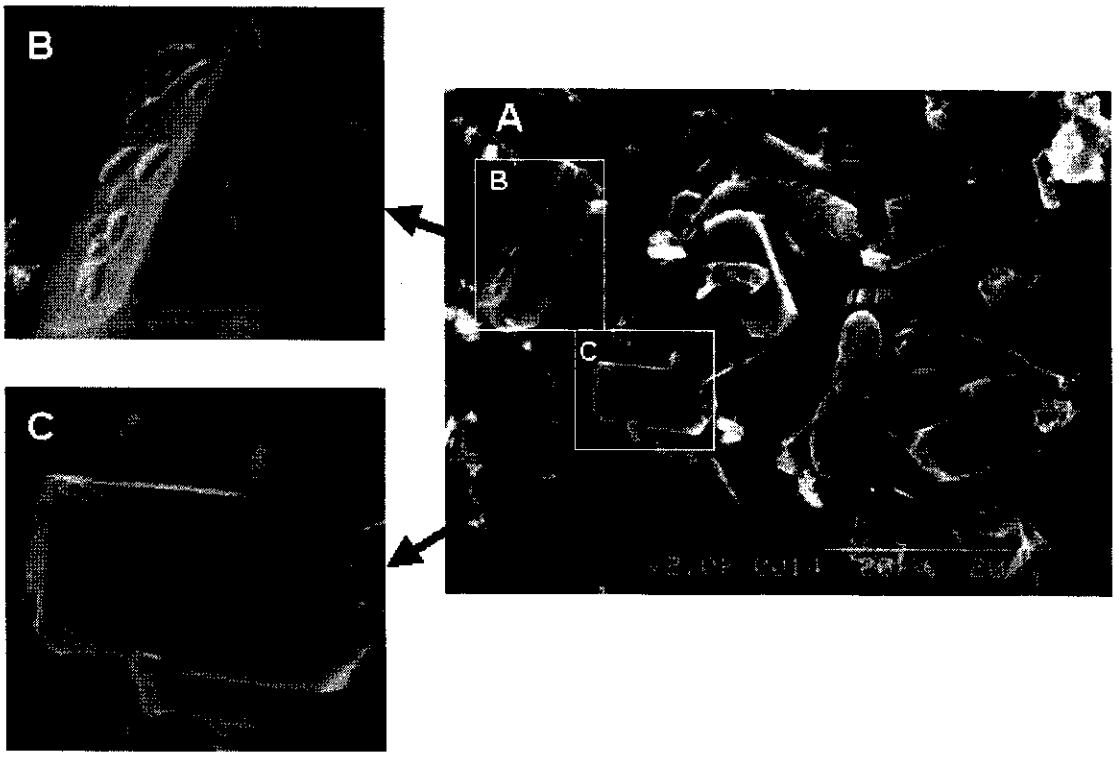

Fig. 10-4. Scanning electron micrographs of mineral grains and attached cells of the highly hydrophilic bacterium, *Halomonas* sp. incubated at a salinity of 0.5% NaCl. Scale bars, 20 μm (A) and 5 μm (B and C).

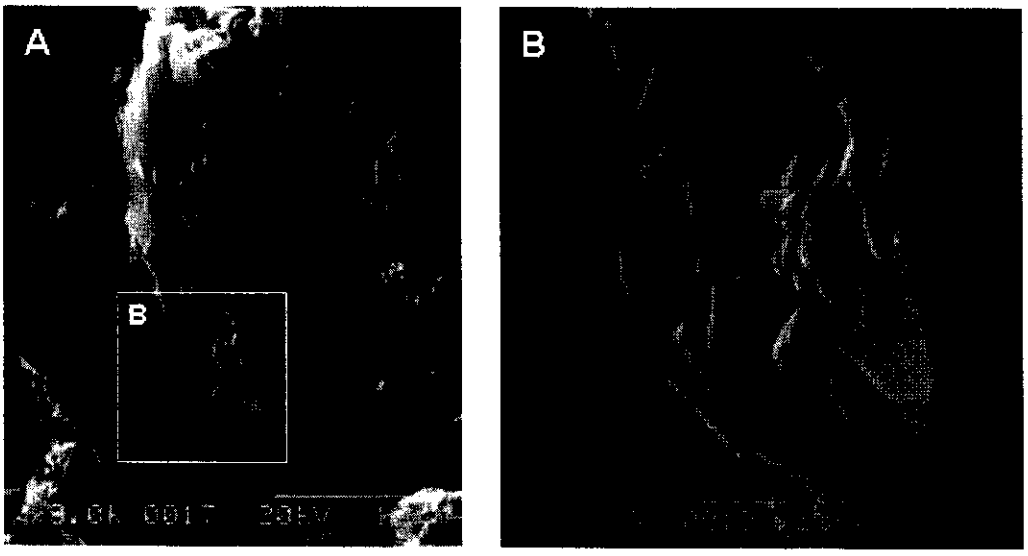

Fig. 10-5. Scanning electron micrographs of mineral grains and attached cells of *Halomonas* sp. incubated at a salinity of 0.5% NaCl. Initiation of microcolony formation is seen. Scale bars, 10 μm (A) and 5 μm (B).

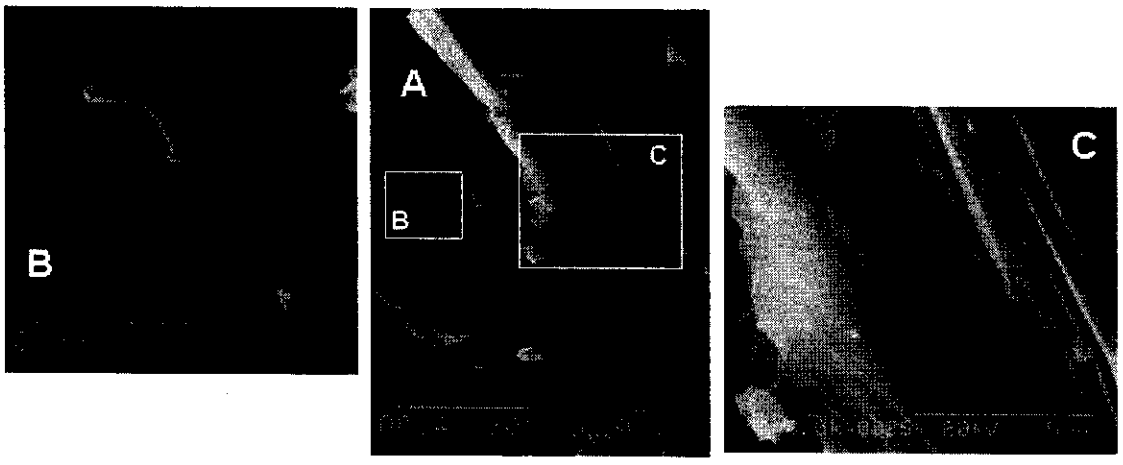

Fig. 10-6. Scanning electron micrographs of mineral grains and attached cells of *Halomonas* sp. incubated at a salinity of 20% NaCl. Cells immediately after binary division (B) and cells attached on cleavage surface of mineral multiplayer (C) are seen. Scale bars, 20 μm (A) and 5 μm (B and C).

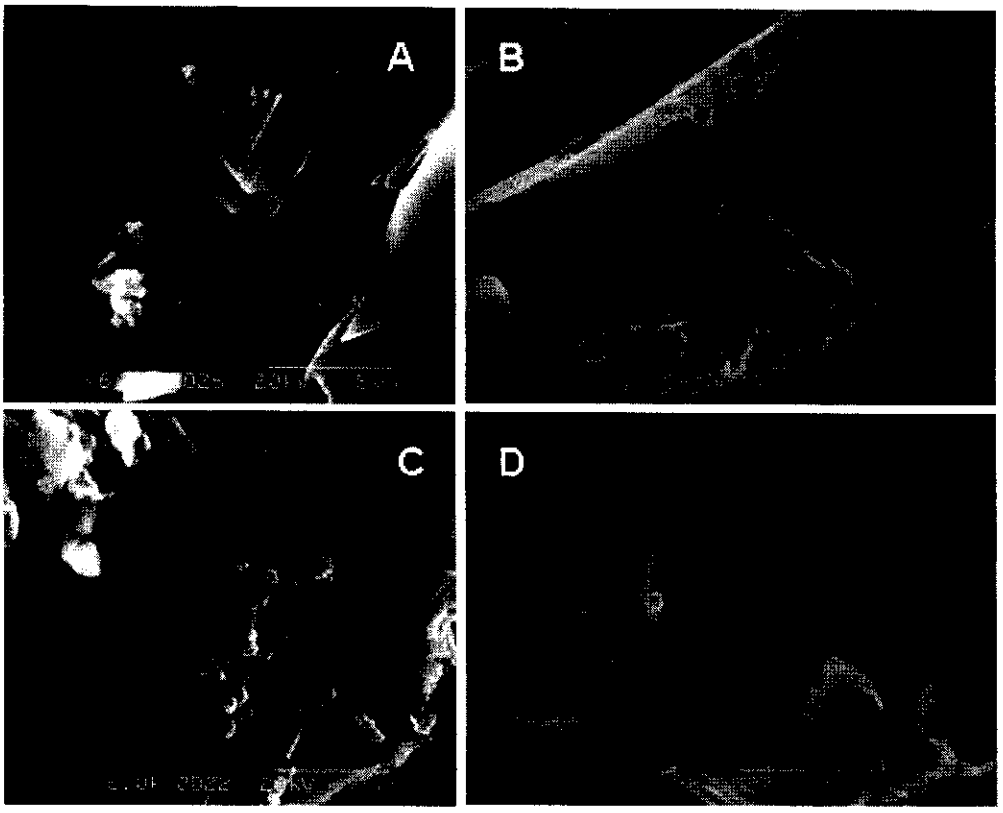

Fig. 10-7. Scanning electron micrographs of mineral grains and attached cells of *Halomonas* sp. incubated at a salinity of 20% NaCl. Microbial aggregate on cleaved grain surface may serve as the initiation core of biofilm formaation (A). Cells are loosely connected to develop biofilms (B and C). Cells also colonize and smooth the pits among grains. Scale bars, 10 μm (B) and 5 μm (A, C and D).

11. Conclusions

In this research, moisture migration and biofilm growth processes in fractured rock masses were investigated. We carried out quantitative, theoretical and experimental studies of wetting and drying of fracture-matrix systems. These include a consistent derivation of the non-linear diffusion equation for matrix flow coupled to an advection-dispersion equation for vapor transport in the fractures; measurement of hydraulic and dielectric properties of the rock sample, a matrix wetting experiment, single-fracture wetting and drying experiments; a fracture-network wetting experiment (biofilm here). For some cases, the Philip's equation was used for data analyses. Selected experiments were numerically simulated to validate the non-linear diffusion equation approach and to obtain insight for more detailed modeling in the future. Most of the experiments were based on the measurement of water content by a dielectric method.

(1) Material Properties

The rock material used for the laboratory experiments throughout this research is "Indiana limestone (Standard Buff Limestone)", whose effective porosity is n=13-17%. Using three cylindrical specimens (diameter=5cm, length=10cm), the mean saturated hydraulic conductivity measured by the transient pulse method is K_s = 1.5x10^{-6}cm/sec and K_s = 4.6x10^{-6}cm/sec when measured using the constant head method. The dielectric property of Indiana Limestone showed a monotonically-increasing relationship between the apparent dielectric constant of rock K_a and volumetric water content θ.

The hydraulic diffusivity and sorptivity were measured using a limestone block. The obtained hydraulic diffusivity $D(\theta)$ followed the exponential function ($D(\theta)$=0.0018exp(55θ)) except for the low water content region. For the low water content, the $D(\theta)$ function showed a significant contribution due to the water movement in vapor

phase, as has been observed for soils as well. The sorptivity measured using the integration method was S=0.0324 cm/min$^{1/2}$. From the slope of $I(t)$ - $t^{1/2}$ curve, S=0.0329 cm/min$^{1/2}$ was obtained, which agreed closely with the integration method.

The approaches used for making these measurements involved time-domain reflectometry (TDR). In the process of making these measurements, we used improved TDR probes, which are applicable to other rocks and in other contexts.

(2) Matrix Wetting Experiment

In the matrix wetting experiment, the wetting front was semi-circular and migrated in the radial direction. The water content measurements revealed that the water content distributions in the matrix were almost the same in the horizontal and vertical directions. These results qualitatively suggest that the effect of gravity is small and a large suction gradient dominates the flow behavior in a low permeability rock matrix. The neglect of gravity driven flow in the rock matrix seems to be appropriate for fractured rock masses, and makes the non-linear diffusion equation approach meaningful.

(3) Single-Fracture Experiments

The amount of water be absorbed by the matrix is independent of the amount of water flowing through the fracture, when the flow rate is sufficiently large (the "matrix-controlled" case). In such cases, the Philip's equation allows us to quantitatively relate the cumulative infiltration $I(t)$ to $t^{1/2}$ by a single parameter 'sorptivity'. This information is of great importance when predicting the travel time of solutes through unsaturated fractured rock masses. In the matrix, the wetting front migrated perpendicular to the fracture and indicated very little gravitational influence. For cases

where flow rate in fracture is less than the matrix imbibition rate, further investigation is necessary. Fracture-matrix interaction alters the hydraulic properties of a fractured rock mass until some time after the imbibition starts. In other words, the fracture-matrix system works as a damper such that a sharp excitation such as an episodic precipitation event results in very high absorption and low outflow. However, in variable aperture fractures, where gravity driven fingers within the fracture plane may be significant, the contact area across which matrix imbibition occurs may be smaller, and significant episodic moisture migration may be possible. This is a topic which merits further investigation.

Unlike in the wetting cycle, the cumulative evaporation did not perfectly follow the Philip's equation. This is because the width of the matrix blocks used in our experiment was not large enough, thus the effect of the boundary became important from the beginning, resulting in a uniform decrease in water content over the matrix width. In addition, the vapor density of the dry air in the fracture increases as it removes vapor from the matrix. This results in a decrease in evaporation rate along the fracture. The change in vapor density might also cause buoyant forces to be mobilized, because moist air has a lower bulk density than dry air. For a more detailed understanding of the drying behavior of fractured rock masses due to the flow of dry air through the fractures, some of these additional influences may need to be considered.

(4) Fracture-Network Experiment

In the fracture-network wetting experiment, the cumulative infiltration into the fracture network exhibited a piecewise linear variation with time$^{1/2}$, with different slopes (i.e. different effective sorptivities), during the time ranges $0<t<30$ hours and $30<t<132$hours. The break in slope is clearly associated with the activation of the second outlet, and is plausibly due to an increase in actual area across which absorption occurs.

This experiment confirms that flow pathways can change and discrete changes in behavior can occur in partially saturated fractured networks.

Roughly speaking, until the wetting fronts are at half way to the center of the tiles, Philip's equation allowed us to quantitatively relate the cumulative infiltration $I(t)$ to $t^{1/2}$ by a parameter 'sorptivity'. It can be concluded that the overall qualitative behavior of the network was similar to that of the single-fracture system at least until the wetting fronts are at the midpoint of the tiles. For future experiments, it is recommended that a surface sealing method be developed and the infiltration behavior after the wetting front passes the midpoint of the tiles be investigated.

(5) Numerical Simulations

In this research, only the first level of validation of the non-linear diffusion equation approach was conducted using 1-D and 2-D models. The simulation of the diffusivity measurement experiment agreed well with the measured data when proper material properties and boundary conditions were used. For the single-fracture wetting cycle, there was a little disagreement between the measured and computed water content values near the fracture at early times possibly due to insufficient number of probes. In case of the single-fracture drying cycle, the drying occurred in two-dimensions, although the measured data was based on the one-dimensional assumption. The desorptivity concept did not perfectly represent the evaporation rate. The material property is known to be hysteretic and the diffusivity function for the wetting cycle was used to simulate the drying phenomenon. These are the main reasons for why the numerical simulation did not predict the water content distribution in the block well. For the drying of the matrix due to air flow in the fracture, the above issues must be examined more carefully. There are some issues to be solved as mentioned above but the

non-linear diffusion equation is a potential method for predicting water migration in a single-fracture system.

The 2-D simulation of the water infiltration into a square tile, and thus into fractured rock masses, showed that the cumulative infiltration would follow the Philip's equation until the wetting front reaches half way to the center of the mean size of the matrix block. This is of great importance when predicting the infiltration behavior into fractured rock masses.

(6) Biofilm formation

Biofilm of a highly halophilic bacterium, *Halomonas* sp., was experimentally formed on simulated fracture surfaces using sandstone fragments. Biofilm formation was started by attachment of bacterial cells, followed by *in situ* proliferation to form microcolonies. The cells and colonies were loosely interconnected to form network-like structures on the grain surfaces, which would further develop to form film-like structures. Bacterial cell attachment and growth in the pits among grains were also observed.

During this study, extensive formation of the *Halomonas* biofilm was not observed, and thus the hydrophobicity of biofilm was not measurable by conventional methods such as contact-angle measurement. Therefore, further developments in biofilm formation by extensive survey of biofilm-forming bacteria and biofilm-forming conditions are needed.

REFERENCES

Anat, A., H. R. Duke, and A. T. Corey, Steady upward flow from water tables, *Colorado State Univ. Hydrol. Paper*, No.7, 1965.

Annan, A. P., Time-domain-reflectometry - Air-gap problem for parallel wire transmission lines, *Report of activities, part B*, Pap. 77-1B, pp. 59-62, Geol. Surv. Of Canada, Ottawa, 1977.

Bruce, R. R., and A. Klute, the measurement of soil moisture diffusivity, Soil Science Society Proceedings, 458-462, 1956.

Charbenuau, R. J., *Groundwater Hydraulics and Pollutant Transport*, Prentice Hall, pp. 593, 2000.

Commission on Geosciences, *Environment and Resources, Conceptual Models of Flow and Transport in the Fractured Vadose Zone*, National Academy Press, pp. 382, 2001.

Covey, W., Mathematical study of the first stage of drying of a moist soil, *Soil Soc. Sci. Am. Proc.*, 130-134, 1963.

Evans, D. D., and T. J. Nicholson, eds., Flow and transport through unsaturated fractured rock, *AGU Geophysical Monograph42*, pp. 186, 1987.

Faybishenko, B., P. A. Witherspoon, and S. M. Benson, Dynamics of fluids in fractured rock, *AGU Geophysical Monograph 122*, pp. 400, 2000.

Ferre, P. A., D. L. Rudolf, and R. G. Kachanoski, Spatial averaging of water content by time domain reflectometry: Implications for twin rod probes with and without dielectric coatings, *Water Resour. Res.*, 32, 271-279, 1996.

Fletcher, M., E. Murphy, Transport of microorganisms in the subsurface: the role of attachment and colonization of particle surfaces, In: Fredrickson, J. K. & M. Fletcher (eds.), "Subsurface Microbiology and Biogeochemistry", pp. 39-68, Wiley-Liss, Inc., New York, U.S.A., 2001.

Gardner, W. R., Some steady state solutions of the unsaturated moisture flow equation with application to evaporation from a water table, *Soil Sci.*, 85, 228-232, 1958.

Gardner, W. R., Solutions of the flow equation for the drying of soils and other porous media, *Soil Sci. Soc. Am. Proc.*, 23, 183-187, 1959.

Glass, R.J. and M. J. Nicholl, Physics of gravity driven fingering of immiscible fluids within porous media: An overview of current understanding and selected complicating factors, *Geoderma*, 70, 133-163, 1996.

Glass, R.J., and L. Yarrington, Simulation of gravity-driven fingering in porous media using a modified invasion percolation model, *Geoderma*, 70, 231-252, 1996.

Glass, R.J., M.J. Nicholl, and S.E. Pringle, Unsaturated flow through a fracture-matrix-network: A first experiment, In: "Bridging the gap between measurements and modeling", *IAHR conference proceedings*, Berkeley, California, March 22-25, 2002.

Hanks, R. J. , and S. A. Bowers, Influence of variations in the diffusivity – Water content relation on infiltration, *Soil Sci. Soc. Am. Proc.*, 263-275, 1963.

Hillel, D., Environmental Soil Physics, *Academic Press*, pp.771, 2000.

Hokett, S. L., J. B. Chapman, and C. E. Russell, Potential use of time domain reflectometry for measuring water content in rock, *J. Hydrol.*, 138, 89-96, 1992.

Jackson, R. D., Water vapor diffusion in relatively dry soil: I. Theoretical consideration and sorption experiments, *Soil Sci. Soc. Proceedings*, 172-176, 1964a.

Jackson, R. D., Water vapor diffusion in relatively dry soil: II. De sorption experiments, *Soil Sci. Soc. Proceedings*, 464-466, 1964b.

Jackson, R. D., Water vapor diffusion in relatively dry soil: III. Steady-state experiments, *Soil Sci. Soc. Proceedings*, 467-470, 1964c.

Knight, J. H., Sensitivity of time domain reflectometry measurement to lateral variations

in soil water content, *Water Resour. Res.*, 28, 2345-2352, 1992.

Knight, J. H., P. A. Ferre, D. L. Rudolph, R. G. Kachanoski, A numerical analysis of the effects of coatings and gaps upon relative dielectric permittivity measurement with time domain reflectometry, *Water Resour. Res.*, 33, 1455-1460, 1997.

Moore, R. E., Water conduction from shallow water tables, *Hilgardia*, 12, 383-426, 1939.

Lin, W. R., N. Hirahara, K. Nishida, M. Takahashi, T. Sakaki, effects of probe installation method, crack existence and high temperature on apparent dielectric constant determined by time domain reflectometry in rocks, *J. of Japanese Assoc. of Hydrological Sciences*, 29189-204, 1999.

Maheshwarla, S. V., R. Venkatasubramanian, and R. F. Bohem, Comparison of time domain reflectometry performance factors for several dielectric geometries: Theory and experiments, *Water Resour. Res.*, 31, 1927-1933, 1995.

Nitao, J. J., T. A. Buschbeck, Infiltration of a liquid front in an unsaturated fractured porous medium, *Water Resources Research*, 27, 2099-2112, 1991.

Philip, J. R., Theory of infiltration: 4. Sorptivity and algebraic infiltration equations, *Soil Sci.*, 84, 257-264, 1957.

Philip, J. R., Theory of infiltration, *Advances in Hydrogeoscience*, 5, 215-297, 1967.

Richards, L. A., Capillary conduction of liquids through porous medium, *Physics*, 1, 318-333,1931.

Rosenberg, M., R. J. Doyle, Microbial cell surface hydrophobicity history, measurement, and significance, In: Doyle, R. J. & M. Rosenberg (eds.), "Microbial Cell Surface Hydrophobicity", pp. 1-38, American Society for Microbiology, Washington, D.C., U.S.A., 1990.

Sakaki, T., K. Sugihara, T. Adachi, K. Nishida, W. R. Lin, Application of time domain reflectometry to determination of volumetric water content in rock, *Water Resources*

Research, 34, 10, 2623-2631, 1998a.

Sakaki, T, T. Kikuchi, T. Adachi, K. Nishida, and W. R. Lin, Comparison of accuracy and practicality of installation methods of time domain reflectometry probes for rock water content measurement, *Proceedings of the 42nd Japan Geotechnical Symposium*, 19-24, 1998b.

Sakaki, T., and H. Rajaram, Experimental investigation of gap and balun effects on water content measurement by two-wire TDR probes, 2002a. (*in preparation*)

Sakaki, T., and H. Rajaram, Hydraulic diffusivity of Indiana limestone measured by a new TDR probe, 2002b. (*in preparation*)

Shen, L. C., W. C. Savre, J. M. Price, and K. Athavere, Dielectric properties of reservoir rocks at ultra-high frequencies, *Geophysics*, 50, 692-704, 1985.

Tidwell, V. C., R. J. Glass, and W. Peplinski, Laboratory investigation of matrix imbibition from a flowing fracture, *Geophysical Research Letters*, 22., 1405-14-8, 1995.

von Hippel, A. (Ed.), *Dielectric Materials and Applications*, 438pp., Artec house, Norwood, Mass., 1995.

Weeks, E. P., Effect of topography on gas flow in unsaturated fractured rock : Conepts and observations, *Geophysical monograph 42*, 165-170, AGU, 1987.

Wharton, R. P., G. A. Hazen, R. N. Rau, and D. L. Best, Electromagnetic propagation logging: Advances in technique and interpretation, *The 55th Annual fall technical conference and exhibition, SPE 9267*,1-12, 1980.

Whisler, F. D., A. Klute, and D. B. Peters, Soil water diffusivity from horizontal infiltration, *Soil Sci. Soc. Am. Proc.*, 32, 6-11, 1968.

Zimmerman, R. W., G. S. Bodvarsson, and E. M. Kwiklis, Absorption of water into porous blocks of various shapes and sizes, *Water Resources Research*, 26, 2797-2806, 1990.